Branching Ratios and Spectral Functions of τ Decays: Final ALEPH Measurements and Physics Implications

The ALEPH Collaboration[1]

Abstract

The full LEP-1 data set collected with the ALEPH detector at the Z pole during 1991-1995 is analysed in order to measure the τ decay branching fractions. The analysis follows the global method used in the published study based on 1991-1993 data, but several improvements are introduced, especially concerning the treatment of photons and π^0's. Extensive systematic studies are performed, in order to match the large statistics of the data sample corresponding to over 300 000 measured and identified τ decays. Branching fractions are obtained for the two leptonic channels and eleven hadronic channels defined by their respective numbers of charged particles and π^0's. Using previously published ALEPH results on final states with charged and neutral kaons, corrections are applied to the hadronic channels to derive branching ratios for exclusive final states without kaons. Thus the analyses of the full LEP-1 ALEPH data are combined to yield a complete description of τ decays, encompassing 22 non-strange and 11 strange hadronic modes. Some physics implications of the results are given, in particular related to universality in the leptonic charged weak current, isospin invariance in a_1 decays, and the separation of vector and axial-vector components of the total hadronic rate. Finally, spectral functions are determined for the dominant hadronic modes and updates are given for several analyses. These include: tests of isospin invariance between the weak charged and electromagnetic hadronic currents, fits of the ρ resonance lineshape, and a QCD analysis of the nonstrange hadronic decays using spectral moments, yielding the value $\alpha_s(m_\tau^2) = 0.340 \pm 0.005_{\text{exp}} \pm 0.014_{\text{th}}$. The evolution to the Z mass scale yields $\alpha_s(M_Z^2) = 0.1209 \pm 0.0018$. This value agrees well with the direct determination from the Z width and provides the most accurate test to date of asymptotic freedom in the QCD gauge theory.

---

[1]See next pages for the list of authors.

The ALEPH Collaboration

S. Schael

Physikalisches Institut das RWTH-Aachen, D-52056 Aachen, Germany

R. Barate, R. Brunelière, I. De Bonis, D. Decamp, C. Goy, S. Jézéquel, J.-P. Lees, F. Martin, E. Merle, M.-N. Minard, B. Pietrzyk, B. Trocmé

Laboratoire de Physique des Particules (LAPP), IN^{2}P^3-CNRS, F-74019 Annecy-le-Vieux Cedex, France

S. Bravo, M.P. Casado, M. Chmeissani, J.M. Crespo, E. Fernandez, M. Fernandez-Bosman, Ll. Garrido,[15] M. Martinez, A. Pacheco, H. Ruiz

Institut de Fĺsica d'Altes Energies, Universitat Autònoma de Barcelona, E-08193 Bellaterra (Barcelona), Spain[7]

A. Colaleo, D. Creanza, N. De Filippis, M. de Palma, G. Iaselli, G. Maggi, M. Maggi, S. Nuzzo, A. Ranieri, G. Raso,[24] F. Ruggieri, G. Selvaggi, L. Silvestris, P. Tempesta, A. Tricomi,[3] G. Zito

Dipartimento di Fisica, INFN Sezione di Bari, I-70126 Bari, Italy

X. Huang, J. Lin, Q. Ouyang, T. Wang, Y. Xie, R. Xu, S. Xue, J. Zhang, L. Zhang, W. Zhao

Institute of High Energy Physics, Academia Sinica, Beijing, The People's Republic of China[8]

D. Abbaneo, T. Barklow,[26] O. Buchmüller,[26] M. Cattaneo, B. Clerbaux,[23] H. Drevermann, R.W. Forty, M. Frank, F. Gianotti, J.B. Hansen, J. Harvey, D.E. Hutchcroft,[30] P. Janot, B. Jost, M. Kado,[2] P. Mato, A. Moutoussi, F. Ranjard, L. Rolandi, D. Schlatter, F. Teubert, A. Valassi, I. Videau

European Laboratory for Particle Physics (CERN), CH-1211 Geneva 23, Switzerland

F. Badaud, S. Dessagne, A. Falvard,[20] D. Fayolle, P. Gay, J. Jousset, B. Michel, S. Monteil, D. Pallin, J.M. Pascolo, P. Perret

Laboratoire de Physique Corpusculaire, Université Blaise Pascal, IN^{2}P^3-CNRS, Clermont-Ferrand, F-63177 Aubière, France

J.D. Hansen, J.R. Hansen, P.H. Hansen, A.C. Kraan, B.S. Nilsson

Niels Bohr Institute, 2100 Copenhagen, DK-Denmark[9]

A. Kyriakis, C. Markou, E. Simopoulou, A. Vayaki, K. Zachariadou

Nuclear Research Center Demokritos (NRCD), GR-15310 Attiki, Greece

A. Blondel,[12] J.-C. Brient, F. Machefert, A. Rougé, H. Videau

Laoratoire Leprince-Ringuet, Ecole Polytechnique, IN^{2}P^3-CNRS, F-91128 Palaiseau Cedex, France

V. Ciulli, E. Focardi, G. Parrini

Dipartimento di Fisica, Università di Firenze, INFN Sezione di Firenze, I-50125 Firenze, Italy

A. Antonelli, M. Antonelli, G. Bencivenni, F. Bossi, G. Capon, F. Cerutti, V. Chiarella, P. Laurelli, G. Mannocchi,[5] G.P. Murtas, L. Passalacqua

Laboratori Nazionali dell'INFN (LNF-INFN), I-00044 Frascati, Italy

J. Kennedy, J.G. Lynch, P. Negus, V. O'Shea, A.S. Thompson

Department of Physics and Astronomy, University of Glasgow, Glasgow G12 8QQ,United Kingdom[10]

S. Wasserbaech

Utah Valley State College, Orem, UT 84058, U.S.A.

R. Cavanaugh,[4] S. Dhamotharan,[21] C. Geweniger, P. Hanke, V. Hepp, E.E. Kluge, A. Putzer, H. Stenzel,

K. Tittel, M. Wunsch[19]

Kirchhoff-Institut für Physik, Universität Heidelberg, D-69120 Heidelberg, Germany[16]

R. Beuselinck, W. Cameron, G. Davies, P.J. Dornan, M. Girone,[1] N. Marinelli, J. Nowell, S.A. Rutherford, J.K. Sedgbeer, J.C. Thompson,[14] R. White

Department of Physics, Imperial College, London SW7 2BZ, United Kingdom[10]

V.M. Ghete, P. Girtler, E. Kneringer, D. Kuhn, G. Rudolph

Institut für Experimentalphysik, Universität Innsbruck, A-6020 Innsbruck, Austria[18]

E. Bouhova-Thacker, C.K. Bowdery, D.P. Clarke, G. Ellis, A.J. Finch, F. Foster, G. Hughes, R.W.L. Jones, M.R. Pearson, N.A. Robertson, M. Smizanska

Department of Physics, University of Lancaster, Lancaster LA1 4YB, United Kingdom[10]

O. van der Aa, C. Delaere,[28] G.Leibenguth,[31] V. Lemaitre[29]
Institut de Physique Nucléaire, Département de Physique, Université Catholique de Louvain, 1348 Louvain-la-Neuve, Belgium

U. Blumenschein, F. Hölldorfer, K. Jakobs, F. Kayser, A.-S. Müller, B. Renk, H.-G. Sander, S. Schmeling, H. Wachsmuth, C. Zeitnitz, T. Ziegler

Institut für Physik, Universität Mainz, D-55099 Mainz, Germany[16]

A. Bonissent, P. Coyle, C. Curtil, A. Ealet, D. Fouchez, P. Payre, A. Tilquin
Centre de Physique des Particules de Marseille, Univ Méditerranée, IN^{2}P^3-CNRS, F-13288 Marseille, France

F. Ragusa
Dipartimento di Fisica, Università di Milano e INFN Sezione di Milano, I-20133 Milano, Italy.

A. David, H. Dietl,[32] G. Ganis,[27] K. Hüttmann, G. Lütjens, W. Männer[32], H.-G. Moser, R. Settles, M. Villegas, G. Wolf

Max-Planck-Institut für Physik, Werner-Heisenberg-Institut, D-80805 München, Germany[16]

J. Boucrot, O. Callot, M. Davier, L. Duflot, J.-F. Grivaz, Ph. Heusse, A. Höcker, A. Jacholkowska,[6] L. Serin, J.-J. Veillet, C. Z. Yuan, Z. Q. Zhang
Laboratoire de l'Accélérateur Linéaire, Université de Paris-Sud, IN^{2}P^3-CNRS, F-91898 Orsay Cedex, France

P. Azzurri, G. Bagliesi, T. Boccali, L. Foà, A. Giammanco, A. Giassi, F. Ligabue, A. Messineo, F. Palla, G. Sanguinetti, A. Sciabà, G. Sguazzoni, P. Spagnolo, R. Tenchini, A. Venturi, P.G. Verdini
Dipartimento di Fisica dell'Università, INFN Sezione di Pisa, e Scuola Normale Superiore, I-56010 Pisa, Italy

O. Awunor, G.A. Blair, G. Cowan, A. Garcia-Bellido, M.G. Green, T. Medcalf, A. Misiejuk, J.A. Strong, P. Teixeira-Dias
Department of Physics, Royal Holloway & Bedford New College, University of London, Egham, Surrey TW20 OEX, United Kingdom[10]

R.W. Clifft, T.R. Edgecock, P.R. Norton, I.R. Tomalin, J.J. Ward
Particle Physics Dept., Rutherford Appleton Laboratory, Chilton, Didcot, Oxon OX11 OQX, United Kingdom[10]

B. Bloch-Devaux, D. Boumediene, P. Colas, B. Fabbro, E. Lançon, M.-C. Lemaire, E. Locci, P. Perez, J. Rander, B. Tuchming, B. Vallage
CEA, DAPNIA/Service de Physique des Particules, CE-Saclay, F-91191 Gif-sur-Yvette Cedex, France[17]

A.M. Litke, G. Taylor

Institute for Particle Physics, University of California at Santa Cruz, Santa Cruz, CA 95064, USA[22]

C.N. Booth, S. Cartwright, F. Combley,[25] P.N. Hodgson, M. Lehto, L.F. Thompson

Department of Physics, University of Sheffield, Sheffield S3 7RH, United Kingdom[10]

A. Böhrer, S. Brandt, C. Grupen, J. Hess, A. Ngac, G. Prange

Fachbereich Physik, Universität Siegen, D-57068 Siegen, Germany[16]

C. Borean, G. Giannini

Dipartimento di Fisica, Università di Trieste e INFN Sezione di Trieste, I-34127 Trieste, Italy

H. He, J. Putz, J. Rothberg

Experimental Elementary Particle Physics, University of Washington, Seattle, WA 98195 U.S.A.

S.R. Armstrong, K. Berkelman, K. Cranmer, D.P.S. Ferguson, Y. Gao,[13] S. González, O.J. Hayes, H. Hu, S. Jin, J. Kile, P.A. McNamara III, J. Nielsen, Y.B. Pan, J.H. von Wimmersperg-Toeller, W. Wiedenmann, J. Wu, Sau Lan Wu, X. Wu, G. Zobernig

Department of Physics, University of Wisconsin, Madison, WI 53706, USA[11]

G. Dissertori

Institute for Particle Physics, ETH Hönggerberg, 8093 Zürich, Switzerland.

Contents

1 Introduction

Because of its relatively large mass and the simplicity of its decay mechanism, the τ lepton offers many interesting, and sometimes unique, possibilities for testing the Standard Model. These studies involve the leptonic and hadronic sectors and encompass a wide range of topics, from the measurement of the leptonic couplings in the weak charged current, providing precise universality tests, to a complete investigation of hadronic production from the QCD vacuum. In the latter case, the τ decay results have proven to be complementary to those from e^+e^- data, enabling detailed studies at the fundamental level to be performed, through the determination of the spectral functions which embody both the rich hadronic structure seen at low energy and the quark behaviour relevant in the higher energy regime. The spectral functions play an important role in the understanding of hadronic dynamics in the intermediate energy range and constitute the basic input for QCD studies and for evaluating contributions from hadronic vacuum polarization. The latter are needed for precision tests of the electroweak theory through the running of α to the M_Z scale and to compute the muon anomalous magnetic moment. The topics of interest include: testing the isospin invariance between the weak charged and electromagnetic hadronic currents; evaluation of chiral sum rules making use of the separate determination of vector and axial-vector components; and a global QCD analysis including perturbative and nonperturbative contributions, offering the possibility of a precise extraction of the strong coupling at a relatively low energy scale, thus providing a sensitive test of the running when compared to the value obtained at the M_Z scale.

A global analysis of the τ branching ratios was performed by the ALEPH Collaboration using the data recorded at LEP through the process $e^+e^- \to Z \to \tau^+\tau^-$ in 1990-1991 [1] and in 1991-1993 [2, 3]. Specific studies of final states including kaons were published using an early data set [4, 5], then with the full 1991-1995 statistics [6, 7, 8], and finally compiled [9]. Nonstrange spectral functions were determined earlier [10], then separately for the vector [11] and the axial-vector [12] components from the 1991-1994 data, leading to a precise determination of $\alpha_s(m_\tau^2)$ and showing that nonperturbative terms are small even at this relatively low scale. The strange spectral function was likewise extracted, from which it was possible to determine the strange quark mass [9]. Finally, a specific study of η and ω resonance production in τ decays was carried out [13].

In this report a complete and final analysis of τ decays is presented using the global method. All data recorded at LEP-I from 1991 to 1995 with the ALEPH detector are used, thus providing an update of the previous results which were based on partial data sets. The increase in statistics —the full sample corresponds to about 2.5 times the luminosity used in the last published global analysis [2, 3]— not only allows for a reduction of the dominant statistical errors but, more importantly, provides a way to better study possible systematic effects and to eventually correct for them. Several improvements of the method have been introduced in order to achieve a better control over the most relevant systematic uncertainties: simulation-independent measurement of the $\tau\tau$ selection efficiency; improved photon identification especially at low energy, where the separation between photons from τ decays and fake photons from fluctuations in hadronic or electromagnetic showers is delicate; a new method to correct the Monte

Carlo simulation for the rate of fake photons; and stricter criteria for channels with small branching fractions. For consistency and in order to maximally profit from the improved analysis all data sets recorded from 1991 to 1995 have been reprocessed with the latest version of the reconstruction and selection programs. The results presented in this report thus supersede those already published in Ref. [1, 2, 3]. In the same way the new determination of the nonstrange spectral functions replaces earlier results in Ref. [10, 11, 12]. Only the measurements on final states containing kaons, which were already based on the full statistics, remain unchanged [6, 7, 8, 9].

The new analysis has been carried out independently for the two data sets taken in 1991-1993 and 1994-1995, respectively. Each data set is associated to its own Monte Carlo sample describing the corresponding detector performance. This method was chosen as it provides an easy way to compare with the previous analysis of the 1991-1993 data sample and to check the consistency between the two sets of new results. The latter comparison is particularly meaningful as the systematic uncertainties are estimated from the agreement between data and Monte Carlo samples, once corrections are applied, and are thus mostly uncorrelated. The final results are obtained from the combination of both sets.

The paper is organized as follows. After a brief description of the ALEPH detector, and of the data and simulated samples in Section 2, the main analysis tools are presented in Sections 3 through 9: selection of $\tau\tau$ events and determination of non-τ backgrounds, charged particle identification, separation of genuine and fake photons, π^0 reconstruction, decay classification, channel-by-channel adjustment of the number of fake photons in the simulation, and branching ratio calculation. The determination of the different sources of systematic uncertainties is the subject of Section 10, while Section 11 provides some global checks on the results. Corrections are applied to raw results in order to obtain branching ratios for exclusive channels, as discussed in Section 12. The consistency between the results obtained from the two data sets is examined in Section 13 and the final combined results are given. Section 14 deals with a few physics topics directly related to the measurement of the branching ratios, such as universality in the leptonic charged weak current, the branching ratio into $\rho\nu_\tau$ in the context of vacuum polarization calculations, a_1 decay fractions into the two isospin-related modes 3π and $\pi 2\pi^0$, and separation of vector and axial-vector modes. The subject of Section 15 is the measurement of hadronic spectral functions, the vector part of which is compared to corresponding results from e^+e^- annihilation in Section 16, providing tests of the Conserved Vector Current (CVC) hypothesis. Finally, a QCD analysis of the vector and axial-vector spectral functions is performed in Sections 17 with a determination of the strong coupling at the τ mass scale, $\alpha_s(m_\tau^2)$ and of the small nonperturbative contributions.

2 The ALEPH detector and the data sample

A detailed description of the ALEPH detector and its performance can be found elsewhere [14, 15]. Only the features relevant to this analysis are briefly mentioned here.

Charged particles are measured by means of three detectors. The closest detector to the interaction point is a silicon vertex detector (VDET), which consists of two concentric

barrels of double-sided microstrip silicon detectors. An inner tracking chamber (ITC), with eight drift chamber layers, surrounds the vertex detector. The ITC is followed by a time projection chamber (TPC), a cylindrical three-dimensional imaging drift chamber, providing up to 21 space points for charged particles, and up to 338 measurements of the ionization loss, dE/dx. Combining the coordinate measurements of these detectors, a momentum resolution $\delta p_T/p_T^2 = 6 \cdot 10^{-4} \oplus 5 \cdot 10^{-3}/p_T$ (with p_T in GeV) is achieved in the presence of a 1.5 Tesla magnetic field.

The electromagnetic calorimeter (ECAL), located inside the coil, is constructed from 45 layers of lead interleaved with proportional wire chambers. The position and energy of electromagnetic showers are measured using cathode pads subtending a solid angle of $0.9° \times 0.9°$ and connected internally to form projective towers. Each tower is read out in three segments with a depth of 4, 9 and 9 radiation lengths, yielding an energy resolution $\delta E/E = 18\%/\sqrt{E} + 0.9\%$ (with E in GeV) for isolated photons and electrons. The inactive zones of this detector, referred to as cracks, represent 2 % in the barrel and 6 % in the endcap regions. The analysis of the hadronic τ decays presented in this paper benefits from the fine granularity and from the longitudinal segmentation of the calorimeter, which play a crucial role in the photon and π^0 reconstruction, and in the rejection of fake photons.

The hadron calorimeter (HCAL) is composed of the iron of the magnet return yoke interleaved with 23 layers of streamer tubes giving a digital hit pattern and has a projective tower cathode pad readout of hadronic energy with a resolution of about $85\%/\sqrt{E}$. Outside this calorimeter structure are located two additional double layers of streamer tubes, providing three-dimensional coordinates for particles passing through the HCAL.

The trigger efficiency for τ pair events is measured by comparing redundant and independent triggers involving the tracking detectors and the calorimeters. The measured trigger efficiency is better than 99.99% within the selection cuts.

Tau-pair events are simulated by means of a Monte Carlo program, KORALZ07, which includes initial state radiation computed up to order α^2 and exponentiated, and final state radiative corrections to order α [17]. The simulation of the subsequent τ decays also includes single photon radiation for the decays with up to three hadrons in the final state. Longitudinal spin correlations are taken into account [18] and the $\sin^2 \theta_W$ value is adjusted to be consistent with the determination from the measurement of τ polarization [16]. The GEANT-based simulation, with the detector acceptance and resolution effects, is used to initially evaluate the corresponding relative efficiencies and backgrounds. It also includes the tracking, the secondary interactions of hadrons, bremsstrahlung and conversions. Electromagnetic showers are generated in ECAL according to parameterizations obtained from test beam data [14]. For all these effects, detailed comparisons with relevant data distributions are performed and corrections to the MC-determined efficiencies are derived, as discussed below for each specific problem.

The data used in this analysis have been recorded at LEP-1 in 1991-1995. The numbers of detected τ decays are correspondingly 132 316 in 1991-1993 and 194 832 in 1994-1995, for a total of about $3.3 \cdot 10^5$. The ratios between Monte Carlo and data statistics are 7.3 and 9.7 for the 1991-1993 and 1994-1995 periods, respectively. Monte Carlo samples were

generated for each year of data taking in order to follow as closely as possible the status of the detector components. For convenience and easier reference to previously published results, the total data and Monte Carlo sets corresponding to the 1991-1993 and 1994-1995 periods are considered separately. Also, part of the data (approximately 11% of the τ sample) was taken off the Z peak in order to measure the lineshape. Corresponding Monte Carlo sets were generated to account for these conditions.

3   Selection of $\tau\tau$ events

3.1   The $\tau\tau$ event selector

The principal characteristics of $\tau\tau$ events in e^+e^- annihilation at the Z energy are low multiplicity, back-to-back topology and missing energy. Particles in each event are reconstructed with an energy flow algorithm [15] which calculates the visible energy, avoiding double-counting between the TPC and the calorimeter information. The reconstructed event is divided into two hemispheres by a plane perpendicular to the thrust axis. The jet in a given hemisphere is defined by summing the four-momenta of energy flow objects (charged and neutral). The energies in the two hemispheres including the energies of photons from final state radiation, E_1 and E_2, are useful variables for separating Bhabha, $\mu\mu$ and $\gamma\gamma$-induced events from the $\tau\tau$ sample, while relatively larger jet masses, wider opening angles, and higher multiplicities indicate $Z \to q\bar{q}$ events.

All these features are incorporated in a standard selector used extensively in ALEPH. While more detailed information can be found in earlier publications [2, 3, 19] the most important cuts are listed below:

1. The total charged multiplicity should be at least two and no more than eight.

2. Each hemisphere is required to have at least one charged track.

3. The scattering angle θ^* in the $\tau\tau$ rest frame, calculated using the measured polar angles θ_1 and θ_2 of the two jets through the relation $\cos\theta^* = \sin(\frac{\theta_1-\theta_2}{2})/\sin(\frac{\theta_1+\theta_2}{2})$, should satisfy $|\cos\theta^*| < 0.9$.

4. The acollinearity angle between the two jets should exceed $160°$.

5. The sum of the jet energies should be larger than $0.35 \times E_{beam}$ and the difference between the transverse momenta of the two jets should satisfy $|\Delta p_t| > 0.066 \times E_{beam}$.

6. At least one track should extrapolate to the interaction point within ± 1 cm transversally to and ± 5 cm along the beam axis.

7. A τ-like hemisphere is defined by its charged multiplicity equal to one and its invariant mass less than 0.8 GeV. For non τ-like hemispheres, the product of the number of energy flow objects in each hemisphere should be less than 40 and the sum of the maximal opening angle between any two tracks in each hemisphere less than 0.25 rad.

8. The ratio of the total energy to the beam energy should be smaller than 1.6, except for $\mu\mu$-like events (both leading tracks are muons, or one is a muon and the energy in the opposite hemisphere is greater than $0.9 \times E_{beam}$) where this cut is relaxed to 1.8. For Bhabha-like events (all the charged tracks are electrons), the cut is tightened to 1.4 if the tangent at the origin to the leading electron points to within ± 6 cm of an ECAL crack.

9. As an additional cut against the residual Bhabha background, the total energy measured independently in the wire planes of ECAL has to be less than $1.8 \times E_{beam}$.

10. Cuts using tight matching in space and momentum between the tracks in opposite hemispheres are used to reject cosmic rays [2].

In the previous analysis [2, 3] additional cuts had been introduced in order to further reduce the contamination from Bhabha and $e^+e^- \rightarrow \mu^+\mu^-$ processes. In the present work it was chosen to simplify the procedure in order to conveniently measure selection efficiencies on the data, at the expense of a slightly larger background contamination which is anyway also measured in the data sample as explained below.

3.2   Measurement of selection efficiencies

The "break-mix" method introduced for the determination of the $\tau\tau$ cross section [19] is used to measure the selection efficiency of the cuts listed above. A selection of $\tau\tau$ events is implemented using very tight cuts on only one hemisphere. Then the opposite hemisphere corresponds to an essentially unbiased τ decay, which is stored away. Pairs of selected hemispheres are combined to construct a $\tau\tau$ event sample built completely from data. This sample is used to measure the efficiency of the cuts based only on energy and/or topology.

The same procedure is applied to the Monte Carlo sample as well as to the data and the ratio of the corresponding efficiencies is taken as a correction to the pure Monte Carlo efficiency. In this way the small correlations between hemispheres which are neglected in the break-mix data sample are properly taken into account.

This method is used to determine the efficiencies of cuts 5 to 9 listed above for both MC and data for large branching ratio channels. Channels with small branching ratios are corrected using the same factor as for nearby topologies, with an error properly enlarged. Results are given in Section 10.2. The measured efficiencies are found to be very close to those obtained by the simulation, deviations being at most at the few per mille level. This situation stems from the facts that the τ decay dynamics is —apart from small branching ratio channels— very well known, the selection efficiencies are large and the simulation of the detector is adequate.

The overall selection efficiency of $\tau\tau$ events is 78.9%. This value increases to 91.7% when the $\tau\tau$ angular distribution is restricted to the detector polar acceptance (cut 3), giving a better indication for the efficiency of the cuts designed to exclude non-$\tau\tau$ backgrounds. In addition, when expressed relatively to each τ decay, the selection

9

efficiencies are only weakly dependent on the final state, with a maximum difference of 10% amongst the considered decay topologies.

3.3 Estimation of non-$\tau\tau$ backgrounds

A method —developed for the measurement of the τ polarization [16]— has been used to measure the contributions from the major non-τ backgrounds: Bhabhas, $\mu^+\mu^-$ pairs, and $\gamma^*\gamma^* \to e^+e^-, \mu^+\mu^-$, and hadrons events. The basic idea is to apply cuts to the selected $\tau\tau$ data in order to reduce as much as possible the $\tau\tau$ population while keeping a high efficiency for the background source under study. The procedure does not require an absolute normalization from the Monte Carlo simulation of these channels, only a qualitative description of the distribution of the discriminating variables. In the following, 'e' and 'μ' designate charged particles identified (see Section 4.2) as electrons and muons, respectively.

For Bhabha background, different event topologies are considered in turn, depending on whether one of the charged particle traverses an inactive area of the ECAL between detector modules. For $e-e$ and $e-crack$ topologies, either the acoplanarity angle is required to be larger than 179° or the acollinearity angle should be more than 175°, in which case the difference of transverse energies is required to be less than 3 GeV. The corresponding Bhabha efficiency (for the final sample) is 88% as determined from the simulation using the UNIBAB generator [20]. The angular distribution of the restricted sample is then fitted to $\tau\tau$ and Bhabha components (also including a small contribution from the other non-τ backgrounds) from the simulation. Therefore, the Bhabha Monte Carlo input is only used to determine the (large) selection efficiency and the $cos\ \theta^*$ shape inside the final sample, not relying on any determination of the absolute Monte Carlo normalization. The derived Bhabha contribution has a statistical uncertainty which is assigned as a systematic error. Several combinations of variables have been tried, showing a good stability of the result within its error. Figure 1 illustrates the determination for the $e-e$ topology in the 1994-1995 sample. For the more numerous $e-hadron$ sample, the same cuts are used, but they have to be supplemented by an additional requirement to suppress true hadrons as compared to electrons misidentified as hadrons. This is achieved by restricting opposite hadrons to have an electron identification probability larger than 0.01; most of the true hadrons are below this value.

A similar technique is used to estimate the μ-pair background. Figure 2 shows the corresponding plots for the $\mu-\mu$ topology, requiring an acoplanarity angle larger than 178°, for which 90% efficiency for $ee \to \mu\mu$ events in the final sample is achieved. Here, the fitted distribution is that of the calculated photon energy along the beam for a postulated $ee \to \mu\mu\gamma\gamma_{beam}$ kinematics to take the most general case compatible with the only information on the two muons. The $ee \to \mu\mu$ background signal is clearly seen for small energies.

The remaining background from $\gamma^*\gamma^* \to \mu\mu$ is easily found in the $\mu-\mu$ topology after requiring the acollinearity angle to be smaller than 170° leading to an efficiency of 57%. The distribution of the acoplanarity angle shows a distinct signal for the background, as seen in Fig. 3.
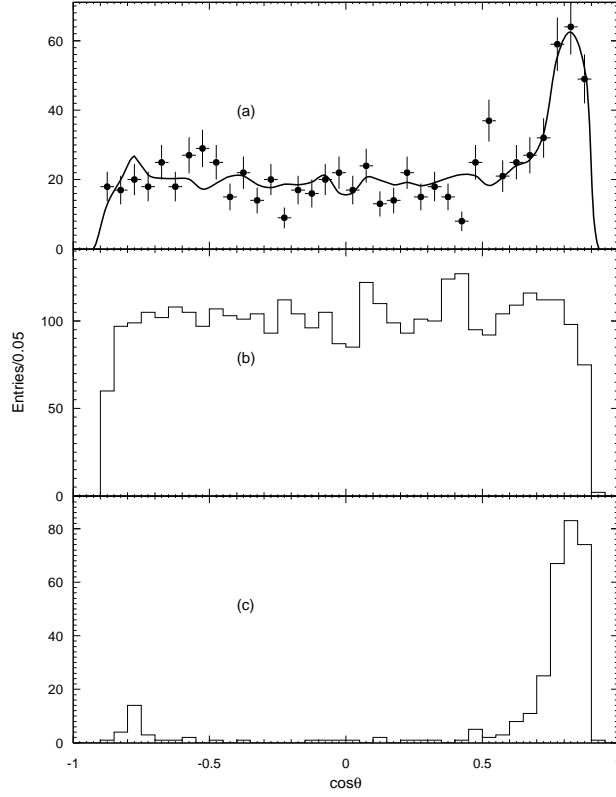
Figure 1: Determination of the remaining Bhabha contribution in the final *e-e* sample for 1994-1995 data: $\cos\theta^*$ distributions for (a) data, (b) $\tau\tau$ simulation, and (c) Bhabha simulation. The solid line represents a fit of the data with the relative normalization of the $\tau\tau$ and Bhabha contributions left free.

11
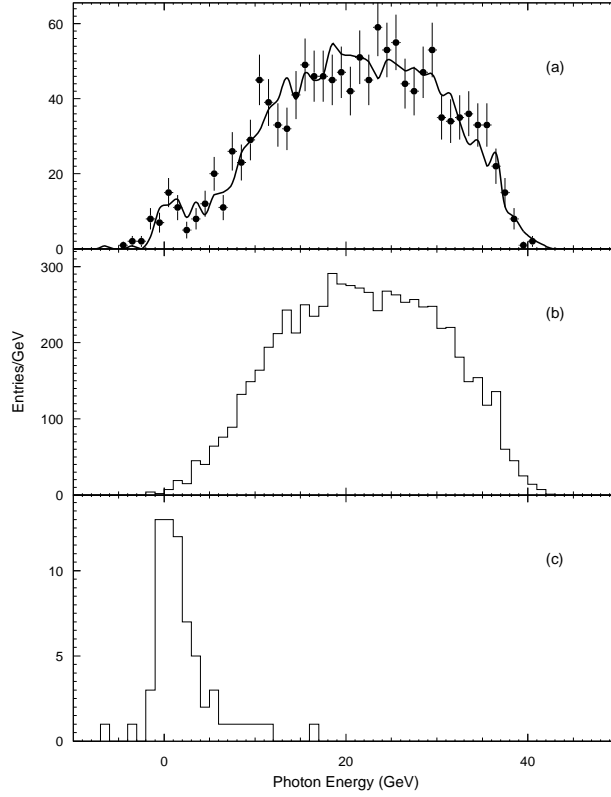
Figure 2: Determination of the remaining $e^+e^- \to \mu^+\mu^-$ contribution in the final μ-μ sample for 1994-1995 data using the kinematically calculated energy of a hypothetical photon emitted along one of the $e^\pm$ momenta: (a) data, (b) $\tau\tau$ simulation, and (c) $e^+e^- \to \mu^+\mu^-$ simulation. The solid line represents a fit of the data with the relative normalization of the $\tau\tau$ and μ-pair contributions left free.
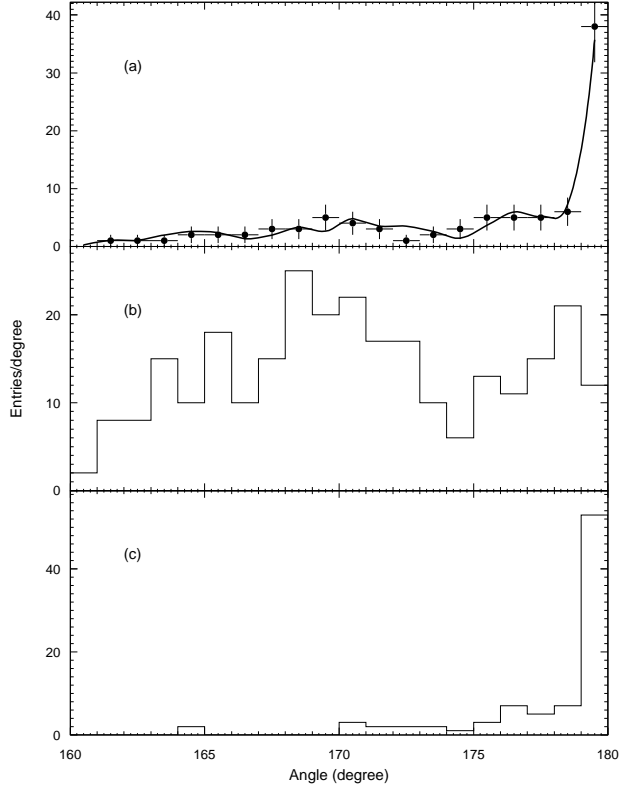
Figure 3: Determination of the remaining $\gamma^*\gamma^* \to \mu^+\mu^-$ contribution in the final μ-μ sample for 1994-1995 data: acoplanarity angle distributions for (a) data, (b) $\tau\tau$ simulation, and (c) $e^+e^- \to (e^+e^-)\mu^+\mu^-$ simulation. The solid line represents a fit of the data with the relative normalization of the $\tau\tau$ and $\gamma\gamma$-induced μ-pair contributions left free.

Table 1: Numbers of non-τ background events in observed classes as defined in Section 7.

class	1991-93	1994-95
e	598 ± 46	745 ± 58
μ	409 ± 45	380 ± 40
h	93 ± 11	100 ± 13
$h\pi^0$	141 ± 22	178 ± 26
$h2\pi^0$	44 ± 9	81 ± 16
$h3\pi^0$	26 ± 7	35 ± 9
$h4\pi^0$	12 ± 3	19 ± 5
$3h$	87 ± 20	129 ± 30
$3h\pi^0$	97 ± 23	165 ± 39
$3h2\pi^0$	27 ± 7	36 ± 10
$3h3\pi^0$	13 ± 4	25 ± 7
$5h$	3 ± 1	7 ± 2
$5h\pi^0$	16 ± 5	21 ± 6
Class 14	249 ± 38	303 ± 52
sum	1815 ± 86	2224 ± 107

The same procedure is applied for $\gamma^*\gamma^* \rightarrow ee$, but additional cuts (for example requiring the total event energy to be less than 35 GeV) must be applied to decrease the Bhabha contribution. Similar techniques are used to determine the contribution of $\gamma^*\gamma^* \rightarrow$ hadrons for low multiplicity events.

Cosmic ray background is determined to be negligible [2]. All other contributions are estimated with the proper Monte Carlo generators. This is the case for four-fermion processes and hadronic Z decays whose contribution is estimated from the Lund generator [21]. Tests were previously made to ascertain the reliability of the prediction for the rate of surviving low multiplicity events by comparing to data [3], resulting in a systematic uncertainty included in the analysis.

The non-τ backgrounds in each channel are listed in Table 1. The contaminations from the different sources are given in Table 2 and amount to a total fraction of $(1.23\pm0.04)\%$ in the full data sample.

4 Charged particle identification

4.1 Track definition

A *good* track is defined to have a momentum greater than or equal to 0.10 GeV (and not smaller than the momentum resolution), $|\cos(\theta)| \leq 0.95$, at least 4 hits in the TPC, and its minimum distance to the interaction point within 2 cm transversally and 10 cm along the beams. If a charged track is not a good one, has at least three hits in the TPC and

14

Table 2: Estimated contaminations from the different background processes.

process	contamination ($\times 10^{-3}$)
Bhabha	4.0
$ee \rightarrow \mu\mu$	1.0
two-γ^* processes	2.2
four-fermion	1.1
hadrons	3.9
cosmic rays	0.1
sum	12.3

the minimum distance to the interaction point is within 20 cm transversally to and 40 cm along the beams, then it is called a *bad* track.

In classifying τ decays, only good tracks are used, after removing those identified as electrons which are used to reconstruct converted photons; the electrons identified as bad tracks are also included in reconstruction of conversions.

4.2 The likelihood identification method

Charged particle identification plays a crucial role in the measurement of τ branching ratios. In this analysis, as in the previous ones, a likelihood method is used to incorporate the information from the relevant subdetectors. In this way, each charged particle is assigned a set of probabilities from which a particle type is chosen.

Eight discriminating variables are used in the identification procedure: dE/dx in the TPC, two estimators (transverse and longitudinal) of the shower profile in ECAL, the average shower width measured with the HCAL tubes in the fired planes, the number of fired planes among the last ten, the energy measured with HCAL pads, the number of hits in the muon chambers, in a road $\pm 4\sigma$-wide around the track extrapolation, where σ is the standard deviation expected from multiple scattering, and finally, the average distance (in units of the multiple-scattering standard deviation) of the hits from their expected position in the muon chambers.

Probability densities $f_i^j(x_i)$ of discriminating variable x_i are determined using the ALEPH simulation for each particle type j, where $j = e, \mu, h$ ($h = $ hadron). No attempt is made in this analysis to separate kaons from pions in the hadron sample since final states containing kaons have been previously studied [6, 7, 8]. Each charged particle is assigned to the type with the largest global estimator defined as

$$P^j = \frac{\prod_i f_i^j(x_i)}{\sum_j \prod_i f_i^j(x_i)} \ . \tag{1}$$

The performance of the particle identification has been studied in detail using control samples of Bhabha events, $\mu\mu$ pairs, $\gamma^*\gamma^*$-induced lepton pairs and hadrons from π^0-tagged τ decays over the full angular and momentum range.
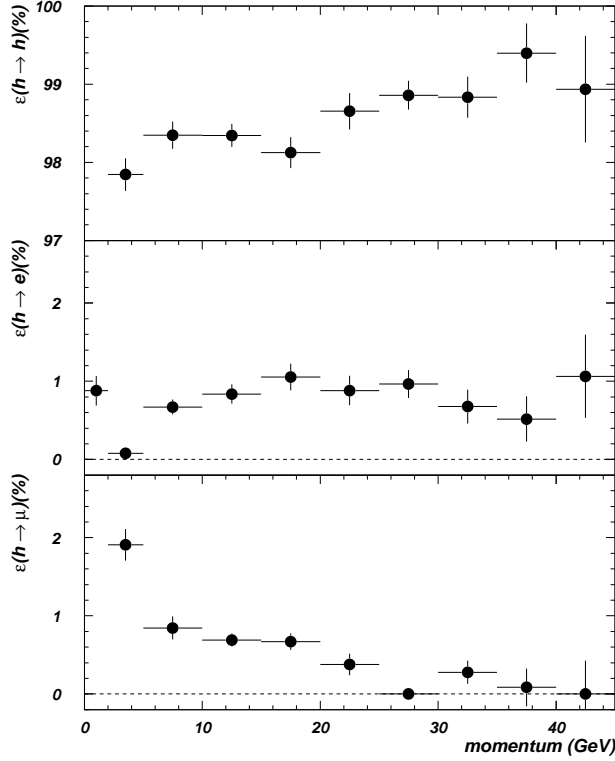
Figure 4: Hadron identification efficiency and misidentification probability obtained from the $\tau\tau$ simulation, corrected from data using the control samples, for the 1994-1995 data set.

The measurement of the particle identification efficiencies and the misidentification probabilities are described in details in Ref. [2]. Basically the efficiencies are obtained from the τ Monte Carlo in order to include the relevant detector description, but corrected as a function of momentum by the ratio of data over Monte Carlo efficiencies as measured with the control samples. This procedure takes care of the slightly different environment for a given particle between the various samples. Figures 4 and 5 show the data-corrected particle identification efficiencies and misidentification probabilities for e, μ and hadron tracks as a function of track momentum. Significant differences are observed between data and simulation, as in previous analyses, emphasizing the necessity of measuring directly these quantities on the data.

5 Photon identification

5.1 The problem of fake photons in ECAL

The high collimation of τ decays at LEP energies quite often makes photon reconstruction difficult, since these photons are close to one another or close to the showers generated by charged hadrons. Of particular relevance is the rejection of fake photons which may occur because of hadronic interactions, fluctuations of electromagnetic showers, or the
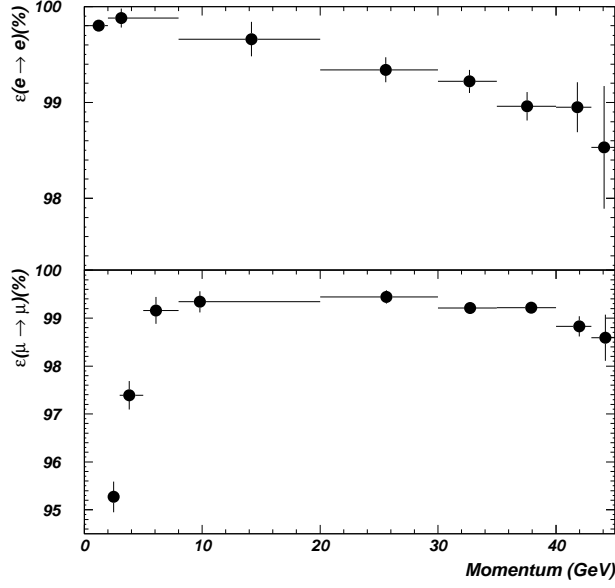
Figure 5: Lepton identification efficiencies obtained from the $\tau\tau$ simulation, corrected from data using the control samples, for the 1994-1995 data set.

overlapping of several showers. These problems reach a tolerable level thanks to the fine granularity of ECAL, in both transverse and longitudinal directions, but they nevertheless require the development of proper and reliable methods in order to correctly identify photon candidates.

A feeling of the fake photon problem can be obtained from Fig. 6 showing the comparison of simulated (at the generator level, after smearing for resolution effects) and observed photon energy spectra. A clear difference at low energy indicates a large contribution from fake photons. Since the fake photons have a complex origin and probably quite dependent of the details of the detector simulation, the procedure developed to separate them from the genuine primary photons from τ decays needs to be calibrated using the data.

5.2   Likelihood method for calorimeter photons

5.2.1   Photon reconstruction

The clustering algorithm for the photon reconstruction [15] starts with a search for local maxima among the towers in the three ECAL stacks. The segments of a projective tower which share a face in common with the local maximum are linked together into a cluster. At the end of the procedure, every segment of a tower is clustered with its neighbour of maximal energy. Then a cluster is accepted as a photon candidate if its energy exceeds 350 MeV and if its barycentre is at least 2 cm from the closest track extrapolation; this distance is slightly modified later after corrections for the finite size of the pads are applied.

The energy of the photon is calculated from the energy deposition in the four central towers only when the energy distribution is consistent with the expectation of a single

17
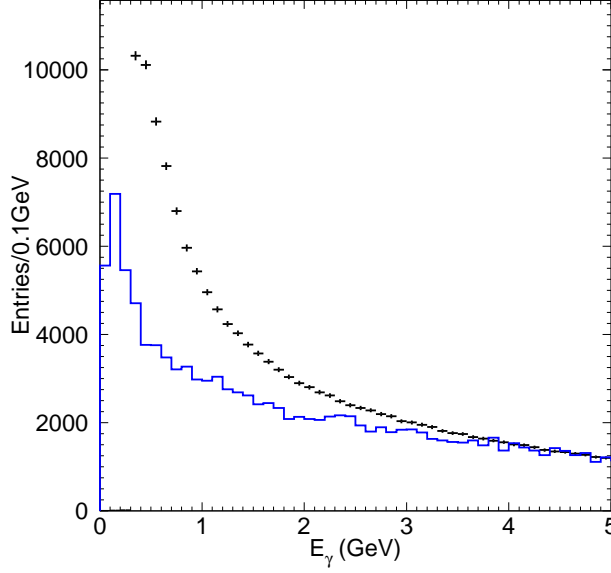
Figure 6: Energy spectra of reconstructed photons in simulated $\tau\tau$ events (points) and of primary produced photons by KORALZ07 after smearing for energy resolution (histogram). The fake photon contribution at lower energies is clearly indicated by normalizing to the number of photons with $E_\gamma > 5$ GeV). The distribution of primary photons is obtained from a statistically reduced sample.

photon, otherwise the sum of the tower energies is taken.

5.2.2 Method for photon identification

As presented above, the main problem is the separation between genuine photons from τ decays and the numerous fake photons generated either by the hadronic tracks interacting in ECAL, or by the fluctuation of the electromagnetic showers. The situation is worse for low energy photons which are however needed to retain a high π^0 reconstruction efficiency.

A likelihood method is used for discriminating between genuine and fake photons. For every cluster, a photon "probability" is defined

$$P_\gamma = \frac{P^{genuine}}{P^{genuine} + P^{fake}} \, , \tag{2}$$

where P^j is the estimator under the photon hypothesis of type j. By definition, genuine photons have a P_γ value near one while fake photons have P_γ near zero. Each estimator P_j is constructed according to

$$P^j = \prod_i \mathcal{P}_i^j(x_i) \tag{3}$$

where $\mathcal{P}_i^j$ is the probability density for the photon hypothesis of type j associated to the discriminating variable x_i.

18
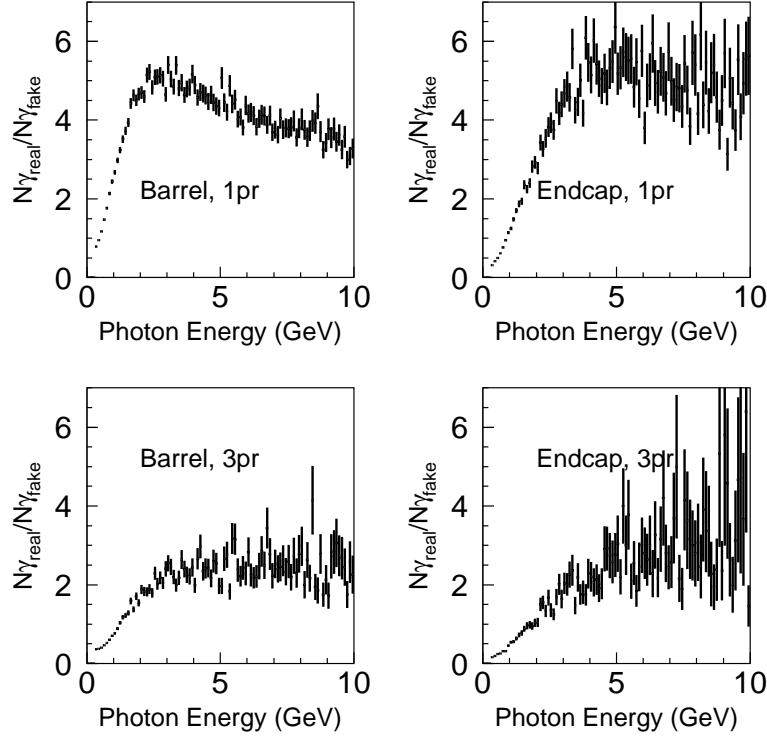
Figure 7: Genuine-to-fake photon ratio as a function of photon energy from simulation, for one- and three-prong τ decays, and in barrel and endcap parts of ECAL.

To take into account the ratio of fake to real photons which is strongly energy-dependent, another quantity is defined as

$$P'_\gamma = \frac{P^{genuine}}{P^{genuine} + P^{fake}/R_{gf}} \ ,$$ (4)

where R_{gf} is the ratio of the numbers of genuine and fake photons, which depends on the photon energy, the number of charged tracks and the number of photons in the hemisphere. This quantity is used in π^0 reconstruction in order to reduce the fraction of π^0 candidates where one of the photons is fake. Figure 7 shows the genuine-to-fake photon ratio as a function of energy as obtained from simulation.

Discriminating variables for each photon candidate used are the distance to the charged track (d_c), the distance to the nearest photon (d_γ), a parameter from the clustering process resulting from the comparison between the energies in the cluster and in the neighbouring cells(G), the fractions of energy deposition in ECAL stacks 1 (R_1), 2 (R_2) and 3 (R_3), and a parameter related to the transverse size of the energy distribution (T). The reference distributions for photons with energy between 1.0 and 1.5 GeV are shown in Fig. 8.

5.2.3 Improvements with respect to the previous analysis

Major improvements were introduced at this stage in the analysis compared to the previous one [3]:

19
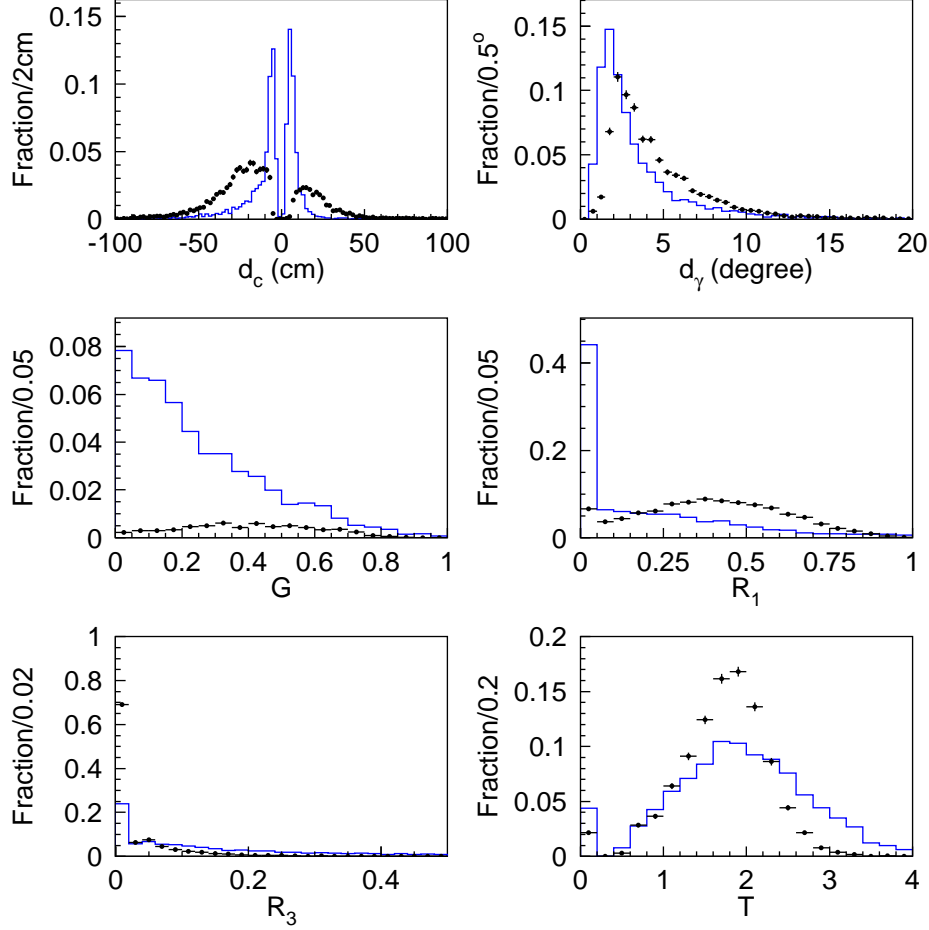
Figure 8: Reference distributions for fake photons (histogram) and genuine photons (points) with energy between 1.0 and 1.5 GeV. The underflows and overflows in each plot are also taken into account in the reference distributions.
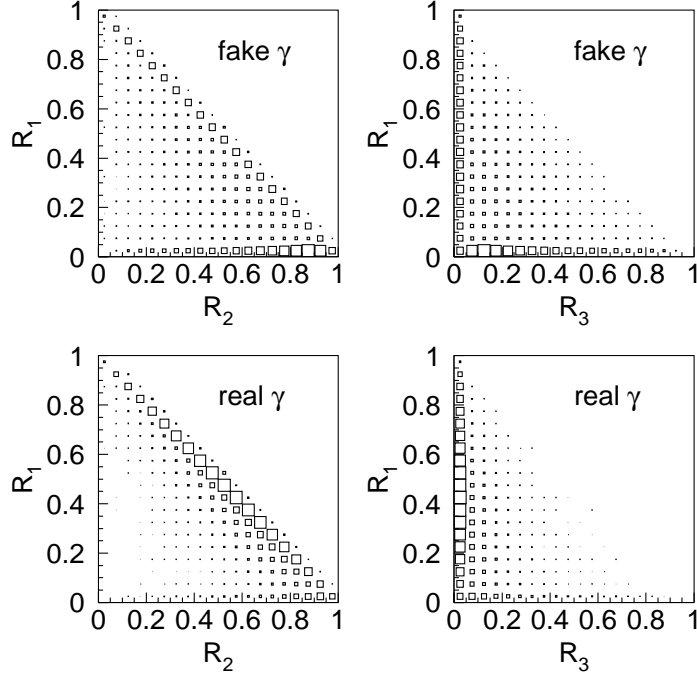
Figure 9: Correlations between R_1 and R_2, and between R_1 and R_3, for photons with energy below 3 GeV.

(1) R_3 is used instead of R_2. This change was made because of the large correlation between R_2 and R_1 for genuine photons, whereas the likelihood method ignores correlations between the discriminating variables. Also, R_3 contributes some additional discriminating power against fake photons (see Fig. 9). As a consequence, genuine and fake photons are better separated.

(2) Instead of using the same reference distributions for the whole energy range as before, energy-dependent reference distributions are now used to improve the discrimination between genuine and fake photons. This is made necessary because the reference distributions show pronounced energy dependence at energies below a few GeV's (see Fig. 10).

(3) Large differences are observed between the reference distributions of ECAL barrel and endcap photons (Figs. 11 and 12), so different sets of reference distributions are used for photons in different regions of the detector.

By comparing the distributions of photons at high energy, good agreement is observed between data and MC photons in d_c, d_γ, and G distributions, while for R_1, R_3 and T there are discrepancies (Fig. 13). The Monte-Carlo-determined reference distributions are then corrected using data. In order to do so, the R_1 and R_3 data distributions are obtained separately for real and fake photons by fitting the uncorrelated d_c distributions with fake and genuine photon d_c distributions from the simulation. For T, the value is shifted and smeared according to the difference between data and Monte Carlo.

21
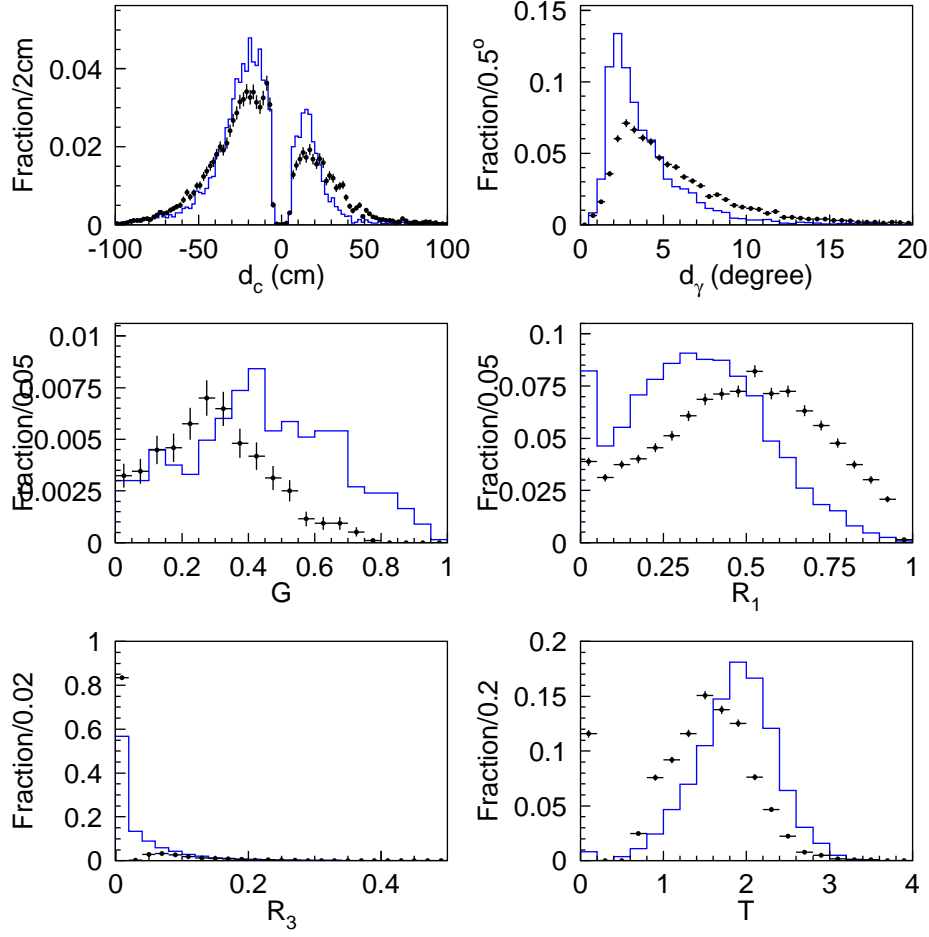
Figure 10: Comparison of the reference distributions for genuine photons in the 0.5-1.0 GeV (points) and 1.5-2.0 GeV (histogram) energy ranges.
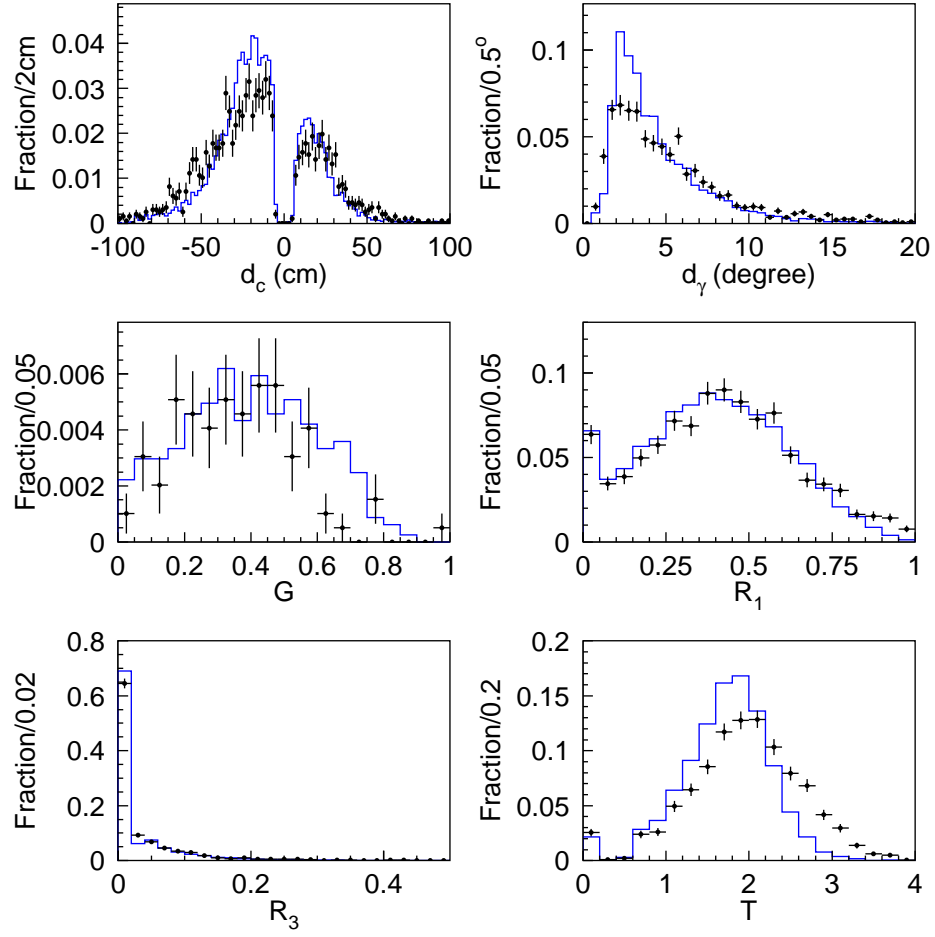
Figure 11: Comparison of the reference distributions in the barrel (histogram) and endcap (points) parts of ECAL for genuine photons between 1.0 and 1.5 GeV.
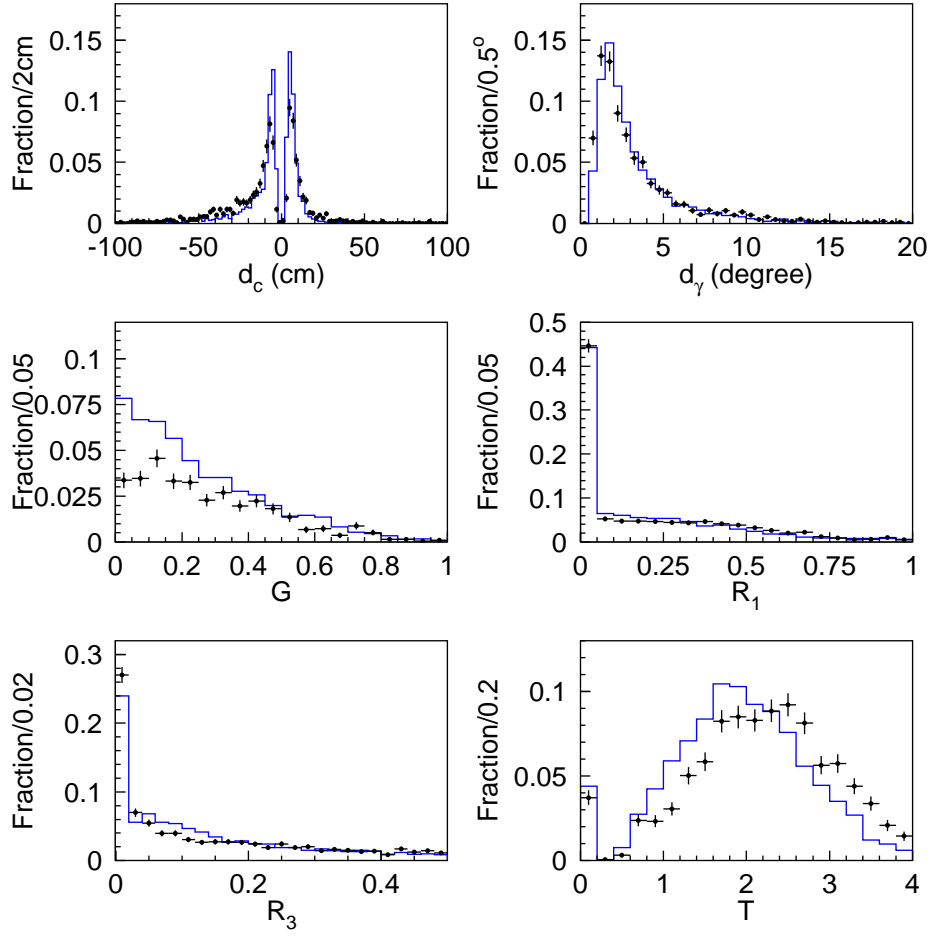
Figure 12: Comparison of the reference distributions in the barrel (histogram) and endcap (points) parts of ECAL for fake photons between 1.0 and 1.5 GeV.
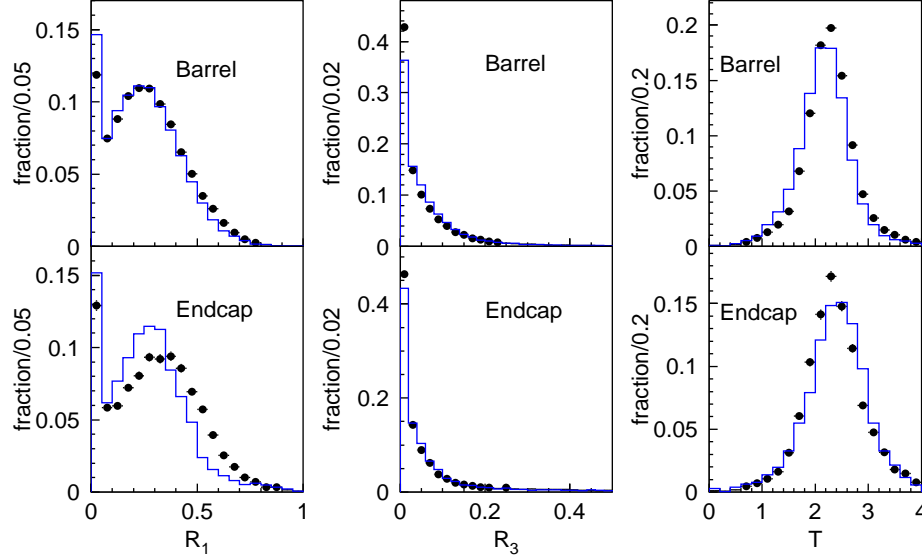
Figure 13: Comparison of R_1, R_3 and T distributions in data (points) and simulation (histogram) for photons with energy between 3.0 and 6.0 GeV, in ECAL barrel and endcap parts.

5.2.4 Total set of reference distributions

Fine granularity is introduced when needed in the reference distributions. Due to the observed strong energy dependence of some distributions, more energy bins are considered: for genuine photons 7 bins (0.3-0.5, 0.5-1.0, 1.0-1.5, 1.5-2.0, 2.0-2.5, 2.5-4.0, above 4 GeV) and for fake photons 4 bins (0.3-0.5, 0.5-1.0, 1.0-2.0, above 2 GeV). Different distributions are set up according to the number of charged tracks (1 and > 1) and of photon candidates (1, 2, 3, 4, > 4 for one prong and 1, 2, > 2 otherwise). Also the barrel and endcap regions of the calorimeter are separated so that the different amount of material in front and the different geometry is taken into account. Thus the photon identification procedure relies on the construction of 768 reference distributions for fake photons and 1344 for genuine photons.

Figure 14 shows the comparison of the photon identification probability (P_γ) before and after introducing energy-dependent reference distributions and the R_3 variable. A spectacular improvement is observed in genuine and fake photon discrimination: at low energy, a clear contribution of genuine photons can be seen, while at high energy, a small, but well identified, fake photon component shows up. Further checking, along the lines discussed below in Section 8, shows the validity of the latter signal on the simulated sample.

5.2.5 Photon energy calibration

Better photon energy calibration is achieved compared to the previous analysis. The procedure, aiming at a relative calibration between data and simulation, is implemented in several steps. First, a calibration is done using electrons from τ decays, treating the

25
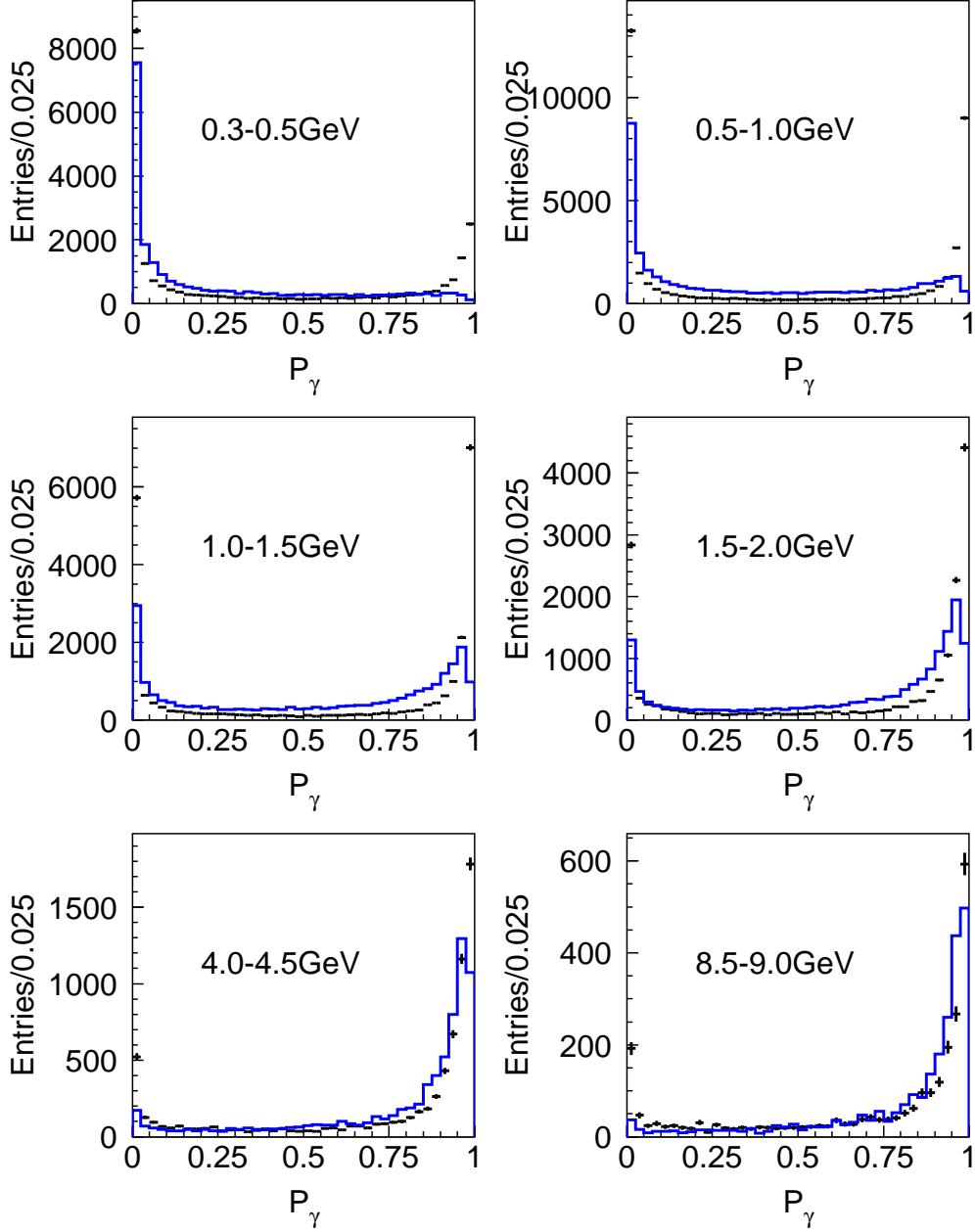
Figure 14: Comparison of the data probability distributions of a cluster to be identified as a genuine photon before (histogram) and after (error bars) introducing energy-dependent reference distributions and the R_3 variable.
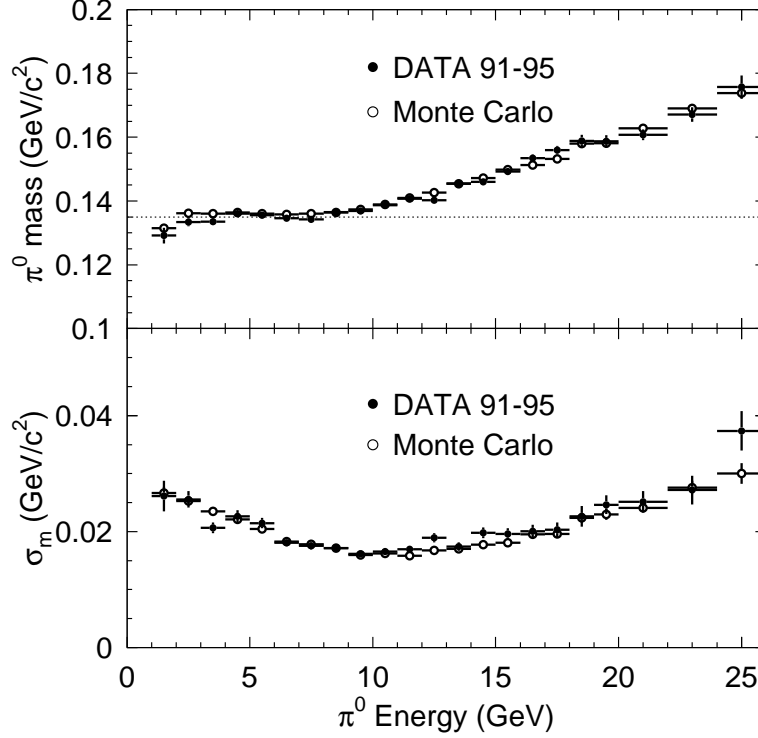
Figure 15: Reconstructed π^0 mass (upper plot) and resolution (lower plot) after photon energy and resolution calibration. Good agreement between data and simulation is observed.

ECAL information as for a neutral cluster. This method is reliable only above 2 GeV because the electron track curvature in the magnetic field causes the shower to be ill-pointing to the interaction region. The results are then extrapolated to lower energies. The bias introduced by the extrapolation is studied with the simulation comparing the true and the extrapolated energies, and the same correction is applied to data. Then the final calibration is achieved by comparing the reconstructed π^0 mass and resolution as a function of energy. The agreement between data and simulation is satisfactory, as seen in Fig. 15.

5.3   Converted photons

In order to identify photons which convert inside the tracking volume all oppositely charged track pairs of a given hemisphere identified as electrons are considered. These candidates are required to have an invariant mass smaller than 30 MeV and the minimal distance between the two helices in the transverse plane must be smaller than 0.5 cm. Finally, all remaining unpaired charged tracks identified as electrons are kept as single track photon conversions. These include Compton scatters or asymmetric conversions where the other track was either lost or poorly reconstructed.

The P_γ estimator is naturally set to unity for a converted photon. As the conversion rate in simulation is found to be lower than that of data by (7.6 ± 1.2) % in 1991-1993
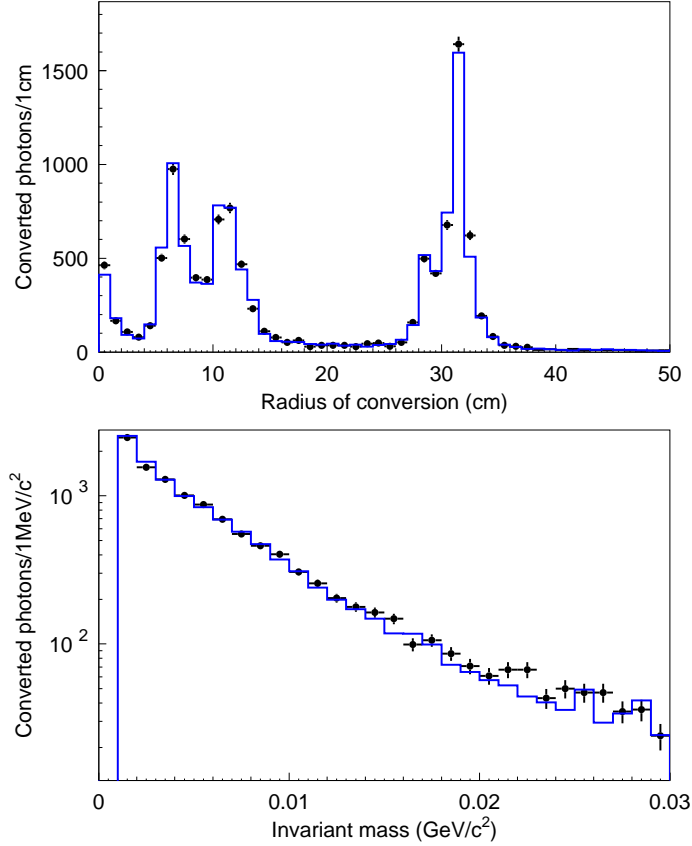
Figure 16: Comparison of the distributions of the conversion point radius and the two-track invariant mass for photon conversions in data (points) and simulation (histogram) for the 1994-1995 data sample. The distribution of material in the detector is well simulated except for a global lower rate in the simulation which is already corrected here.

and (9.3 ± 1.0) % in 1994-1995, some converted photons in data are turned randomly into calorimeter photons and assigned a P_γ value, generated according to the observed distribution for calorimeter photons at the same energy. Figure 16 shows the comparison of the radial conversion point and the invariant mass of two-track conversions between data and simulation. After correcting for the conversion rate, good agreement is observed.

6 π^0 reconstruction

6.1   Different π^0 types

The goal of the π^0 reconstruction procedure is to achieve a high efficiency while keeping the "fake" π^0's at a reasonably small level. Three different kinds of π^0's are thus reconstructed: resolved π^0 from two-photon pairing, unresolved π^0 from merged clusters, and residual π^0 from the remaining single photons after removing radiative, bremsstrahlung and fake photons.

6.2 Resolved π^0's

Since fake and genuine photons are better separated than previously published [3], a cut on P_γ before π^0 reconstruction is introduced to remove a large fraction of fake photons, while keeping the real photon efficiency high. The cut is energy-dependent, $\ln P_{\gamma cut} > 0.15 - 2.9 \times E_\gamma$, with an efficiency $> 90\%$ at $E_\gamma < 0.5$ GeV, and $\sim 100\%$ above 2 GeV.

A π^0 estimator D_{ij} is defined [3] to take into account the genuine and fake photon ratio at different energies:

$$D_{ij} = P'_{\gamma_i} \cdot P'_{\gamma_j} \cdot P_{\pi^0} \; , \tag{5}$$

where P_{π^0} is the χ^2 probability of a kinematic π^0-mass constrained fit of the two photons. It should be noted that P'_γ is used here instead of P_γ, as in the earlier analysis, in order to keep the same confidence for π^0's reconstructed from photons at different energies. Finally, π^0 candidates are retained if their D_{ij} value is larger than 1×10^{-4}.

In addition, a criterion must be established for choosing among all the accepted $i - j$ pairs in a multiphoton environment. Configurations with the maximum number of π^0's are retained and among those, the configuration which maximizes the product of all D_{ij}'s is kept.

In the old analysis [3], a significant difference in observed π^0 mass and resolution in data and simulation was observed. After the recalibration of the photon energy and resolution using the procedure described above, data and simulation agree reasonably well as shown in Fig. 15.

6.3 Unresolved π^0's

As the π^0 energy increases it becomes more difficult to resolve the two photons and the clustering algorithm may yield a single cluster. The two-dimensional energy distribution in the plane perpendicular to the shower direction is examined and energy-weighted moments are computed. Assuming only two photons are present, the second moment provides a measure of the $\gamma\gamma$ invariant mass [15].

Figure 17 shows this invariant mass distribution for data and simulation. Clusters with mass greater than 0.1 GeV are taken as unresolved π^0's. Some discrepancy is observed between data and Monte Carlo and in order to keep the same efficiency a slightly different value for the π^0 mass cut is applied in the simulation. It should be noted that this cut only affects the definition of unresolved and residual π^0's, and thus does not change in first order the π^0 multiplicity, hence the definition of the τ decay final state. Thus it has essentially no influence on the branching ratio analysis, since both unresolved and residual π^0s are used in the τ decay classification.

6.4 Residual π^0's

After the pairing and the cluster moment analysis, all the remaining photons inside a cone of $30°$ around the jet axis are considered. They come from different sources:
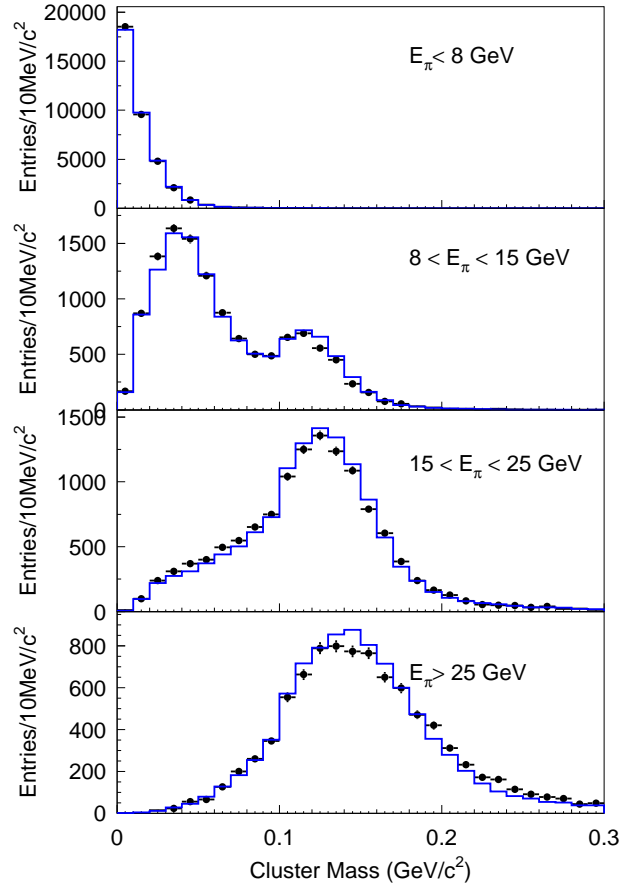
Figure 17: Comparison of the π^0 mass distributions of unresolved π^0's between data (points) and simulation (histogram) in different energy ranges.

- *bremsstrahlung*: bremsstrahlung photons radiated along the final charged particles in τ decay, including the contribution from the detector material for electrons,

- *radiative*: initial and final state radiation non-collinear to charged particles in the final state,

- *genuine* photons from π^0 decays where the partner photon is lost because of energy threshold, reconstruction inefficiency, cracks or overlap with another electromagnetic or hadronic shower,

- *genuine single* photons, mostly from $\omega \to \pi^0 \gamma$ and $\eta \to \gamma\gamma$, and

- *fake* photons.

With respect to the previous analysis, the cut on P_γ is tightened for residual π^0's since better discrimination between real and fake photons is now achieved. The cut used, $\ln P_{\gamma cut} > -0.23 - 0.40 \times E_\gamma$, has a rapidly increasing efficiency above 50% below 0.5 GeV and is about 90% at 3 GeV.

The radiative and bremsstrahlung photons are selected using the same method as described in the previous analysis [3]. Estimators P_{brem}, P_{rad} and $P_{\pi^0 \to \gamma}$ are calculated to select photons from bremsstrahlung, radiative processes and from π^0 decays, respectively. To compute these estimators, the angle between the photon and the most energetic charged track is used, in addition to the discriminating variables considered previously for the photon identification. Radiative and bremsstrahlung photons are not used in the τ decay classification discussed below.

The behaviour of these estimators was studied in Ref. [3]. The agreement between the number of bremsstrahlung photons in data and simulation is good, and affects mainly the electron τ decay channel where this contribution is important (however it does not affect the rate). Bremsstrahlung photons in hadronic channels (i.e. radiation along the final state charged pions) are at a much lower level and are difficult to pick up unambiguously in the data. The estimate of the effect of this contribution largely relies on the description of radiation at the generator level in the Monte Carlo [22]. This point is addressed in Section 10.11.

7 Decay classification

Each τ decay is classified topologically according to the number of charged hadrons, the charged particle identification and the number of π^0's reconstructed. While for one-prong and five-prong channels the exact multiplicity is required, the track number in three-prong channels is allowed to be 2, 3 or 4, in order to reduce systematic effects due to tracking and secondary interactions. Thus 13 classes are defined as given in Table 3. In this table, the right-most column shows how the different considered τ decays contribute to the reconstructed channels as defined. Throughout this paper only τ^- decays are cited and charge-conjugate modes are implied.

Table 3: Definition of the reconstructed τ decay classes. All τ decay modes implemented in the simulation are specified for each class. The notation τ stands for τ^- and the charge conjugate states are implied, while h stands for any charged hadron (π or K).

Class label	Reconstruction criteria	Generated τ decay
e	$1\ e$	$\tau \to e^- \overline{\nu}_e\, \nu_\tau$
μ	$1\ \mu$	$\tau \to \mu^- \overline{\nu}_\mu\, \nu_\tau$
h	$1\ h$	$\tau \to \pi^-\, \nu_\tau$ $\tau \to \pi^- K^0 \overline{K}^0\, \nu_\tau$ $\tau \to K^-\, \nu_\tau$ $\tau \to K^- K^0\, \nu_\tau$ $\tau \to K^{*-}\, \nu_\tau$
$h\,\pi^0$	$1\ h\ +\ \pi^0$	$\tau \to \rho^-\, \nu_\tau$ $\tau \to K^- \pi^0 K^0\, \nu_\tau$ $\tau \to \pi^- \pi^0 \overline{K}^0\, \nu_\tau$ $\tau \to K^{*-}\, \nu_\tau$
$h\,2\pi^0$	$1\ h\ +\ 2\pi^0$	$\tau \to a_1^-\, \nu_\tau$ $\tau \to \pi^- \omega\, \nu_\tau$ [2] $\tau \to K^{*-}\, \nu_\tau$ $\tau \to \pi^- K^0 \overline{K}^0\, \nu_\tau$ $\tau \to K^-\, 2\pi^0\, \nu_\tau$ $\tau \to K^- K^0\, \nu_\tau$
$h\,3\pi^0$	$1\ h\ +\ 3\pi^0$	$\tau \to \pi^- 3\pi^0\, \nu_\tau$ $\tau \to K^- \pi^0 K^0\, \nu_\tau$ $\tau \to \pi^- \pi^0 \overline{K}^0\, \nu_\tau$ $\tau \to \pi^- \pi^0 \eta\, \nu_\tau$ [3]
$h\,4\pi^0$	$1\ h\ +\ \geq 4\pi^0$	$\tau \to \pi^- 4\pi^0\, \nu_\tau$ $\tau \to \pi^- \pi^0 \eta\, \nu_\tau$ [4] $\tau \to \pi^- K^0 \overline{K}^0\, \nu_\tau$
$3h$	$2-4h$	$\tau \to a_1^-\, \nu_\tau$ $\tau \to K^- K^+ \pi^-\, \nu_\tau$ $\tau \to K^{*-}\, \nu_\tau$ $\tau \to \pi^- K^0 \overline{K}^0\, \nu_\tau$ $\tau \to K^- \pi^+ \pi^-\, \nu_\tau$ $\tau \to K^- K^0\, \nu_\tau$
$3h\,\pi^0$	$2-4h + \pi^0$	$\tau \to 2\pi^- \pi^+ \pi^0\, \nu_\tau$ [5] $\tau \to K^- \pi^0 K^0\, \nu_\tau$ $\tau \to \pi^- \pi^0 \overline{K}^0\, \nu_\tau$
$3h\,2\pi^0$	$3h + 2\pi^0$	$\tau \to 2\pi^- \pi^+ 2\pi^0\, \nu_\tau$ [6] $\tau \to \pi^- \pi^0 \eta\, \nu_\tau$ [7] $\tau \to \pi^- K^0 \overline{K}^0\, \nu_\tau$
$3h\,3\pi^0$	$3h + \geq 3\pi^0$	$\tau \to 2\pi^- \pi^+ 3\pi^0\, \nu_\tau$
$5h$	$5h$	$\tau \to 3\pi^- 2\pi^+\, \nu_\tau$ $\tau \to \pi^- K^0 \overline{K}^0\, \nu_\tau$
$5h\,\pi^0$	$5h + \pi^0$	$\tau \to 3\pi^- 2\pi^+ \pi^0\, \nu_\tau$

[2] With $\omega \to \pi^0 \gamma$

[3] With $\eta \to \gamma\gamma$

[4] With $\eta \to 3\pi^0$

[5] This channel includes $\tau \to \pi\omega\, \nu_\tau$ with $\omega \to \pi^- \pi^+ \pi^0$

[6] This channel includes $\tau \to \pi\pi^0 \omega\, \nu_\tau$ with $\omega \to \pi^- \pi^+ \pi^0$

[7] With $\eta \to \pi^- \pi^+ \gamma$

The definition of the leptonic channels requires an identified electron or muon with any number of photons. Some cuts on the total final state invariant mass are introduced to reduce feedthrough from hadronic modes [2]. Also some decays with at least two good electron tracks are now included, when one or more of such tracks are classified as converted photons.

In the previous analysis [3], the $3h2\pi^0$, $3h3\pi^0$ and $h4\pi^0$ channels (where h stands for any charged hadron: π or K) suffered from large backgrounds and consequently had a low signal-to-noise ratio. Most of these backgrounds are due to secondary interactions of the hadronic track with material in the inner detector part. In order to improve the definition of these channels the following steps are taken: (1) require the exact charged multiplicity $n_{ch} = 3$ (instead of 2, 3, or 4) for $3h2\pi^0$ and $3h3\pi^0$, (2) demand a maximum impact parameter of charged tracks less than 0.2 cm (instead of 2 cm) for $3h3\pi^0$, and (3) require the number of resolved π^0s in $3h3\pi^0$ to be 3 or 2, and 4 or 3 in $h4\pi^0$. With these tightened cuts the signal-to-noise ratio improves significantly with a small loss of efficiency.

It should be emphasized that all hemispheres from the selected $\tau\tau$ event sample are classified, except for single tracks going into an ECAL crack (but for identified muons) or with a momentum less than 2 GeV (except for identified electrons and hemispheres with at least one reconstructed π^0). These latter decays, in addition to the rejected ones in the $3h2\pi^0$ or $3h3\pi^0$ channels are put in a special class, labelled 14, which then collects all the non-selected hemispheres. By definition, the sample in class-14 does not correspond to one physical τ decay mode. In fact, it follows from the simulation that this class comprises about 21% electron, 27% muon, 41% 1-prong hadronic and 11% 3-prong τ decays. However, consideration of class-14 events can test if the rejected fraction is correctly understood, as discussed later.

The numbers of τ's classified in each of the considered decay channels are listed in Table 4.

The KORALZ07 generator [17] in the Monte Carlo simulation incorporates all the decay modes considered in Table 3. Since the $h4\pi^0$ decay channel is not included in the standard Monte Carlo, a separate generation was done where one of the produced τ is made to decay into that mode using a phase space model for the hadronic final state, while the other τ is treated with the standard decay library. The complete behaviour between the generated decays and their reconstructed counterparts using the decay classification is embodied in the efficiency matrix. This matrix ε_{ji} gives the probability of a τ decay generated in class j to be reconstructed in class i. Obtained initially using the simulated samples, it is corrected for effects where data and simulation can possibly differ, such as particle identification, as discussed previously, and photon identification as affected by the presence of fake photons. The latter correction is presented next, before exhibiting the final corrected matrix.

Table 4: Number of reconstructed events in 1991-1993 and 1994-1995 data sets in the different considered topologies.

Reconstr. class	n_i^{obs} (91-93)	n_i^{obs} (94-95)
e	22405	33100
μ	22235	32145
h	15126	22429
$h\pi^0$	32282	49008
$h2\pi^0$	12907	18317
$h3\pi^0$	2681	3411
$h4\pi^0$	458	499
$3h$	11610	17315
$3h\pi^0$	6467	9734
$3h2\pi^0$	1091	1460
$3h3\pi^0$	124	150
$5h$	60	105
$5h\pi^0$	36	59
Class 14	4834	7100
sum	132316	194832

8 Adjusting the number of fake photons in the simulation

The number of fake photons in the simulation does not agree well with the rate in data. Such a discrepancy is seen in the comparison between the photon energy distributions in data and simulation given in Fig. 18: at low energy there is clear indication that the rate of simulated fake photons is insufficient. This effect will affect the classification of the reconstructed final states in the Monte Carlo and bias the efficiency matrix constructed from this sample. A procedure must be developed to correct for this effect.

8.1 The method

Taking explicitly into account the number k of fake photons in a τ decay, the efficiency matrix can be rewritten as

$$\varepsilon_{ji} = \sum_k \varepsilon_{jik} \cdot \omega_{jk} \tag{6}$$

where ε_{jik} is the efficiency for a produced event in class j with k fake photons to be reconstructed in class i. It can be calculated from the simulation directly, given the number of fake photon in each event. Above ω_{jk} is the fraction of produced class j events with k fake photons. The insufficient fake photons in simulation is due to the fact that ω_{jk}^{MC} is different from ω_{jk}^{data}.
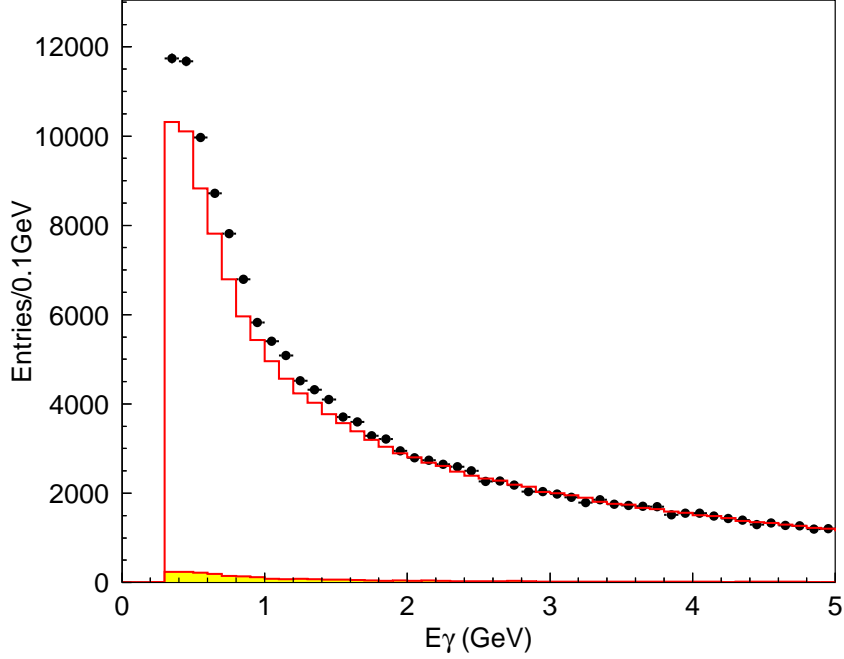
Figure 18: Energy spectra of observed photons in data (error bars) and Monte Carlo (histogram) samples. When normalized above 5 GeV photon energy the two distributions show a clear discrepancy in the low energy region. The shaded histogram shows the contribution from non-τ backgrounds.

Assuming each fake photon is produced randomly, one can get the fake photon multiplicity in Monte Carlo by in principle randomly removing a fraction of f fake photons in real data sample, *i.e.*

$$\omega^{MC} = A\omega^{data} \tag{7}$$

where $\omega^{data} = (\omega_0, \omega_1, \omega_2, \ldots, \omega_n)_{data}$ and $\omega^{MC} = (\omega_0, \omega_1, \omega_2, \ldots, \omega_n)_{MC}$ are the fake photon multiplicity distributions in data and simulation respectively. The matrix A is given by

$$A_{kl} = C_l^{l-k} f^{l-k} (1-f)^k \tag{8}$$

if $k \leq l$, otherwise it is 0. Here k, l run from 0 up to the maximum number of fake photons. The above equation holds for all the produced classes, with one parameter f_j for each class.

The number of fake photons in data can be expressed as

$$N_i^{f,data} = \sum_j N_j^{produced,data} \sum_k \varepsilon_{jik} \cdot k \cdot \sum_l (A_j^{-1})_{kl} \cdot \omega_{jl}^{MC} \tag{9}$$

i is the index for reconstructed class. In this set of equations, the numbers $N_i^{f,data}$ are obtained from photon probability fits in the reconstructed data samples, $N_j^{produced,data}$ from the produced $\tau\tau$ number and the measured branching ratios (implying an iterative procedure which in fact converges extremely fast), ε_{jik} from the simulation with a proper procedure to determine k (called matching in the following), ω_{jl}^{MC} from the simulation

35

and matching, while $(A_j^{-1})_{kl}$ depends on the f_j unknowns to be determined by solving the equations.

Thus to measure the f_j factors, the number of fake photons in each simulated event and the number of fake photons in each reconstructed class in data must be determined.

8.2 Counting fake photons in simulation: the photon matching procedure

To count the number of fake photons in each simulated event, the philosophy is to remove all the clusters reconstructed in ECAL associated with produced photons at the generator level. The remaining clusters are then declared to be fake photons.

To match a produced photon to an ECAL cluster, the cluster with minimum χ^2 is selected, with

$$\chi^2 = \left(\frac{\delta\theta}{\sigma_\theta}\right)^2 + \left(\frac{\delta\phi}{\sigma_\phi}\right)^2 + \left(\frac{\delta E}{\sigma_E}\right)^2 \tag{10}$$

where the quantities with δ correspond to differences between reconstructed and generated levels, while the σ denote the corresponding expected resolutions. A matching flag M is assigned to each cluster according to the χ^2 value. The photon sample with $M = 1$ corresponds to small χ^2 and should be almost exclusively composed of genuine photons, with a small feedthrough from fake photons. The sample with intermediate χ^2 is still dominated by genuine photons with a larger fake photon content. At the end of the loop over the produced (genuine) photons the unmatched clusters are given a flag $M = -1$, corresponding to an almost pure sample of fake photons with a small amount of genuine photons.

Many effects affect the matching procedure, leading to an incorrect estimate of the number of fake photons in the event: energy threshold, ECAL non-sensitive regions (cracks, acceptance), merging with other neutral clusters, merging with charged tracks, accidental matching. These effects have been studied very carefully and χ^2 cuts are chosen so that the real photon contamination in the fake photon sample is the same as the fake photon contamination in the real photon sample. In this way the number of fake photons is given by the number of $M = -1$ photons, facilitating considerably further treatment of the fake photon contribution.

8.3 Fits to data

Using as reference the P_γ distributions for $M = -1$ and $M \neq -1$ of a reconstructed class in the simulation, the P_γ distribution of all photons in a class i of data is fitted with these two components, and then corrected by the fraction of contaminated parts in the two distributions. Figure 19 shows a typical fit in this procedure. The fitted fake photon numbers in each observed class after correction are listed in Table 5, with the error from the fit and the correction.
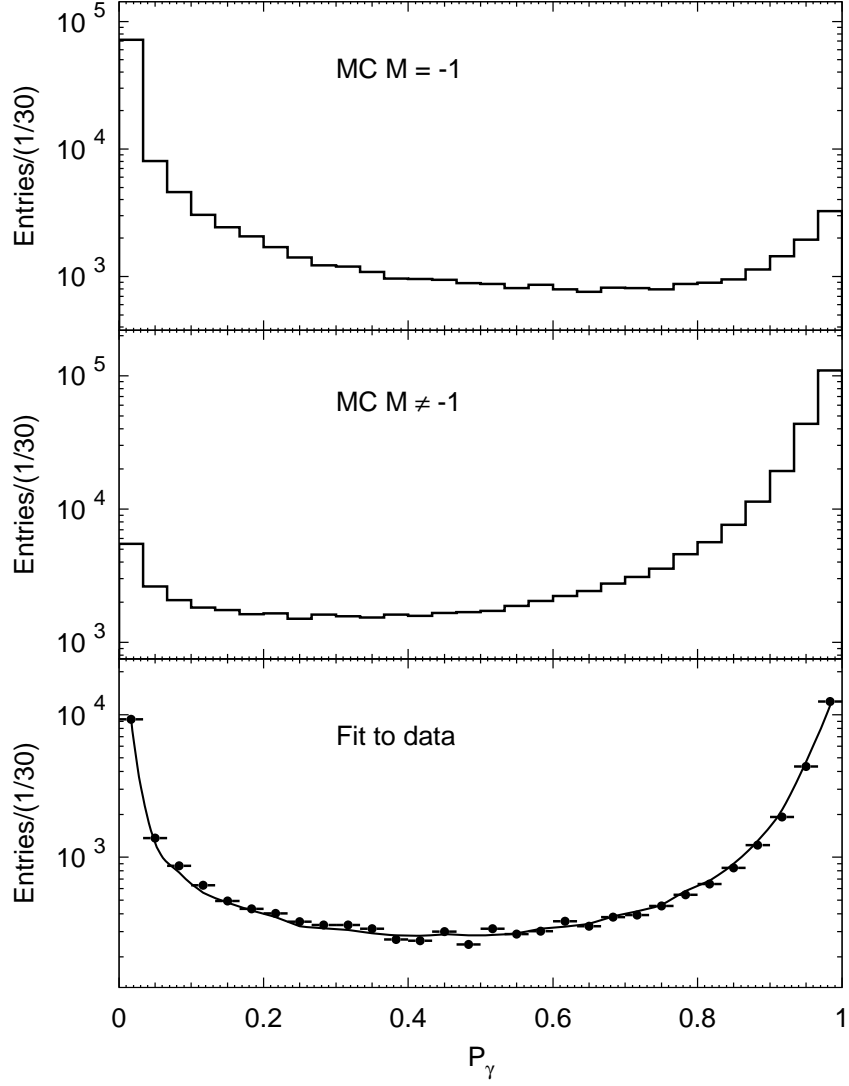
Figure 19: Fit to the photon probability distribution in observed $h\pi^0$ events for the 1994-1995 data set. From top to bottom, are the probability distributions of fake and real photon samples in the simulation from the matching procedure, and the fit to the data distribution using the two Monte Carlo components.

Table 5: Number of fake photons in 1991-93 and 1994-1995 data sets.

Reconstr. class	91-93	94-95
e	2448 ± 75	3552 ± 110
μ	183 ± 24	170 ± 26
h	3718 ± 58	5766 ± 98
$h\pi^0$	9708 ± 196	14844 ± 350
$h2\pi^0$	5941 ± 172	8837 ± 237
$h3\pi^0$	2311 ± 83	3085 ± 90
$h4\pi^0$	574 ± 35	677 ± 35
$3h$	5769 ± 88	8639 ± 162
$3h\pi^0$	4130 ± 98	6444 ± 112
$3h2\pi^0$	1129 ± 48	1432 ± 52
$3h3\pi^0$	183 ± 18	225 ± 24
$5h$	45 ± 6	73 ± 13
$5h\pi^0$	30 ± 6	52 ± 8
Class 14	1369 ± 43	2014 ± 62

8.4   An independent check

The total excess of fake photons in data with respect to Monte Carlo from the fits to the P_γ distributions in each observed class can be checked comparing the photon energy spectra of data and Monte Carlo, after normalization to the number of τ events and correcting the simulation for measured branching ratios. The latter method is justified by the fact that fake photons show up as an excess at energies typically less than 1-2 GeV. The former estimate yields 7279 ± 334 and 11419 ± 511 for 1991-1993 and 1994-1995 data samples respectively summing up all channels, while the latter yields 7007 ± 307 and 10820 ± 376 for the two data sets. The differences

$$\Delta_{91-93} = 272 \pm 454 \tag{11}$$
$$\Delta_{94-95} = 599 \pm 634 \tag{12}$$

indicate that the number of fake photons estimated from the fit procedure is reliable.

8.5   Solving for the fake photon correction factors

In order to reduce the number of parameters to be determined, it is assumed that the correction factors of some channels with small branching ratios are the same as those of the nearby channels with comparable multiplicity. Also the μ channel is not considered since it is hardly influenced by fake photons and the feedthrough to other channels is very small. Therefore the correction factors are only fitted for e, h, $h\pi^0$, $h2\pi^0$, $3h$ and $3h\pi^0$ channels. The results are given in Table 6. They are consistent for the two data/Monte Carlo sets. The resulting $\chi^2/$ degrees of freedom (DF) is 12.4/5 and 15.2/5 for 1991-1993

Table 6: Fake photon correction factors for 1991-1993 and 1994-1995 data sets.

produced class	91-93 (%)	94-95 (%)
e	41.0 ± 1.9	36.1 ± 2.2
h	8.3 ± 2.2	12.1 ± 2.3
$h\pi^0$	21.7 ± 2.2	20.5 ± 2.6
$h2\pi^0$	13.0 ± 2.7	18.7 ± 2.0
$3h$	12.9 ± 1.6	14.0 ± 1.9
$3h\pi^0$	25.1 ± 2.5	27.4 ± 1.6

and 1994-1995 data respectively. The final error on the fitted correction factors has been properly enlarged to take into account these somewhat large values.

8.6   Comparison to the previously used method

In the published analysis using 1991-1993 data [3] a much less sophisticated approach was taken. The deficit of fake photons in the simulation was determined in a global way to be $(16 \pm 8)\%$, common to all channels. Since it would have been delicate to generate extra fake photons, the procedure chosen was to actually do the opposite, $i.e.$ randomly kill identified (in the sense of the matching procedure discussed above) fake photons in the simulation, determine the new efficiency matrix and use the deviations to correct in the opposite direction.

The current way of dealing with the fake photon problem is both more precise and more reliable. The fact that different channels are treated separately provides a handle on the different origins of the fake photons, since, for example, fake photons in the h class only originate from hadronic interactions, whereas they come from both hadronic interactions and photon shower fluctuations in the $h\pi^0$ class. Also the previous procedure was dependent on the quality of the photon matching in simulation and the killing of fake photons entailed the possibility to mistakenly removing some genuine photons as well.

9   Determination of the branching ratios

The branching ratios are determined using

$$n_i^{obs} - n_i^{bkg} \;=\; \sum_j \varepsilon_{ji} N_j^{prod} \tag{13}$$

$$B_j \;=\; \frac{N_j^{prod}}{\sum_j N_j^{prod}} \tag{14}$$

where n_i^{obs} is the number of observed τ candidates in reconstructed class i, n_i^{bkg} the non-τ background in reconstructed class i, ε_{ji} the efficiency of a produced class j event

Table 7: Efficiency matrix for 1994-95 data (in %). Generated classes are given in the first row, and reconstructed classes in the first column. All the corrections are applied except that for nuclear interactions and hadron misidentification in multiprong channels. The last row gives the selection efficiency for each produced class.

	e	μ	h	$h\pi^0$	$h2\pi^0$	$h3\pi^0$	$h4\pi^0$	$3h$	$3h\pi^0$	$3h2\pi^0$	$3h3\pi^0$	$5h$	$5h\pi^0$
e	73.26	0.01	0.41	0.45	0.34	0.25	0.74	0.02	0.02	0.05	0.00	0.00	0.00
μ	0.01	74.49	0.63	0.22	0.07	0.21	0.33	0.01	0.01	0.00	0.00	0.00	0.00
h	0.25	0.75	65.03	3.56	0.34	0.06	0.00	1.44	0.10	0.08	0.00	0.80	0.00
$h\pi^0$	1.02	0.26	4.70	68.19	11.31	2.15	0.49	0.48	1.28	0.62	0.05	0.24	0.00
$h2\pi^0$	0.12	0.01	0.33	5.67	57.68	23.13	7.57	0.08	0.39	1.48	0.24	0.04	0.00
$h3\pi^0$	0.01	0.00	0.07	0.41	6.92	43.06	38.15	0.01	0.10	0.37	0.71	0.04	0.00
$h4\pi^0$	0.00	0.00	0.02	0.05	0.67	6.25	25.26	0.00	0.02	0.11	0.19	0.00	0.00
$3h$	0.01	0.02	0.25	0.07	0.03	0.00	0.00	67.98	6.77	0.80	0.03	22.11	2.52
$3h\pi^0$	0.01	0.01	0.22	0.56	0.27	0.06	0.06	7.29	58.90	16.53	4.46	7.07	16.04
$3h2\pi^0$	0.00	0.00	0.04	0.06	0.10	0.08	0.02	0.41	6.02	40.42	25.02	0.28	0.65
$3h3\pi^0$	0.00	0.00	0.00	0.00	0.00	0.01	0.05	0.02	0.41	6.19	28.98	0.00	0.00
$5h$	0.00	0.00	0.00	0.00	0.00	0.00	0.00	0.01	0.01	0.00	0.00	38.70	4.58
$5h\pi^0$	0.00	0.00	0.00	0.00	0.00	0.00	0.00	0.01	0.02	0.03	0.08	2.99	38.72
Class 14	3.27	4.17	6.38	0.73	1.08	1.71	1.75	0.80	3.66	9.96	13.87	5.03	9.75
sum	77.06	79.72	78.08	79.97	78.81	76.97	74.42	78.56	77.71	76.64	73.64	77.30	72.26

reconstructed as class i, and N_j^{prod} the produced events number of class j. The class numbers i, j run from 1 to 14, the last one corresponding to the rejected τ candidates.

The efficiency matrix ε_{ji} is determined from the Monte Carlo, but corrected using data for many effects such as particle identification efficiency, $\tau\tau$ selection efficiency and fake photon simulation. It is given in Table 7 where the last line shows that the selection efficiency remains constant within $\pm$ 5% for all 13 considered topologies.

It should be noted that the efficiency matrix ε_{ji} is independent of the τ branching ratios used in the simulation, except for the subclasses contributing to each defined class as shown in Table 3. The effect depends however on small branching ratios for final states including kaons and the procedure used for this correction relies on the ALEPH measured values [9].

The analysis assumes a standard τ decay description. One could imagine unknown decay modes not included in the simulation, but since large detection efficiencies are achieved in the $\tau\tau$ selection which is therefore robust, so that these decays would be difficult to pass unnoticed. An independent measurement of the branching ratio for undetected decay modes, using a direct search with a one-sided τ tag, was done in ALEPH [23], limiting this branching ratio to less than 0.11% at 95% CL. This result justifies the assumption that the sum of the branching ratios for visible τ decays is equal to unity.

The equations are conveniently solved by a minimization technique and all corrections not yet included in the efficiency matrix are applied. These small final corrections are discussed in the following section on systematic studies. The branching ratios are obtained and listed in Table 8. The results on the class-14 "branching ratio" are discussed in Section 13.1.

Table 8: Branching ratios (%) from 1991-1993 and 1994-1995 data sets; the first error is statistical and the second is systematic.

Topology	91-93	94-95
e	$17.859 \pm 0.112 \pm 0.058$	$17.799 \pm 0.093 \pm 0.045$
μ	$17.356 \pm 0.107 \pm 0.055$	$17.273 \pm 0.087 \pm 0.039$
h	$12.238 \pm 0.105 \pm 0.104$	$12.058 \pm 0.088 \pm 0.083$
$h\pi^0$	$26.132 \pm 0.150 \pm 0.104$	$26.325 \pm 0.123 \pm 0.090$
$h2\pi^0$	$9.680 \pm 0.139 \pm 0.124$	$9.663 \pm 0.107 \pm 0.105$
$h3\pi^0$	$1.128 \pm 0.110 \pm 0.086$	$1.229 \pm 0.089 \pm 0.068$
$h4\pi^0$	$0.227 \pm 0.056 \pm 0.047$	$0.163 \pm 0.050 \pm 0.040$
$3h$	$9.931 \pm 0.097 \pm 0.072$	$9.769 \pm 0.080 \pm 0.059$
$3h\pi^0$	$4.777 \pm 0.093 \pm 0.074$	$4.965 \pm 0.077 \pm 0.066$
$3h2\pi^0$	$0.517 \pm 0.063 \pm 0.050$	$0.551 \pm 0.050 \pm 0.038$
$3h3\pi^0$	$0.016 \pm 0.029 \pm 0.020$	$-0.021 \pm 0.023 \pm 0.019$
$5h$	$0.098 \pm 0.014 \pm 0.006$	$0.098 \pm 0.011 \pm 0.004$
$5h\pi^0$	$0.022 \pm 0.010 \pm 0.009$	$0.028 \pm 0.008 \pm 0.007$
Class 14	$0.017 \pm 0.043 \pm 0.042$	$0.099 \pm 0.035 \pm 0.037$

10 Determination of systematic uncertainties

10.1 Methodology

Wherever possible the efficiencies relevant to the analysis have been determined using ALEPH data, either directly on the $\tau\tau$ sample itself or on specifically selected control samples, as for example in the case of particle identification. The resulting efficiencies are thus measured with known statistical errors.

In some cases the procedure is less straightforward and involves a model for the systematic effect to be evaluated. An important example is given by the systematics in the simulation of fake photons in ECAL. In such cases the evaluation of the systematic error not only takes into account the statistical aspect, but also some estimate of the systematics involved in the assumed model. The latter is obtained from studies where the relevant parameters are varied in a range consistent with the comparison between data and Monte Carlo distributions.

Quite often a specific cut on a given variable can be directly studied. The comparison between the corresponding distributions, respectively in data and Monte Carlo, provides an estimate of a possible discrepancy whose effect would be to change the assumed efficiency of the cut. If a significant deviation is observed, a correction is applied to the simulation to obtain the nominal branching ratio results, while the error on the deviation provides the input to the evaluation of the systematic uncertainty. The analysis is therefore repeated with a full re-classification of all the measured τ decay candidates, changing the incriminated cut by one standard deviation. Since the new samples slightly

Table 9: Selection efficiencies (%) for $\tau\tau$ events, corresponding to cuts 5-9 described in Section 3.1 , measured by the break-mix method for the 1994-1995 data.

class	data (BM)	Monte Carlo (BM)	R=data/MC
e	95.70 ± 0.10	95.54 ± 0.07	1.0017 ± 0.0012
μ	96.10 ± 0.10	96.20 ± 0.06	0.9990 ± 0.0012
h	96.03 ± 0.10	95.95 ± 0.07	1.0009 ± 0.0013
$h\pi^0$	97.07 ± 0.10	97.26 ± 0.04	0.9980 ± 0.0011
$h2\pi^0$	95.36 ± 0.16	95.68 ± 0.10	0.9967 ± 0.0020
$3h$	94.77 ± 0.18	95.10 ± 0.10	0.9965 ± 0.0022
$3h\pi^0$	92.53 ± 0.22	92.93 ± 0.19	0.9957 ± 0.0031

differ from the nominal ones because of feedthrough between the different channels, the modified results are affected both by the systematic change in the variable value and the statistical fluctuation from the event sample which is uncommon to both samples. In this case the final systematic uncertainty is obtained by adding linearly the modulus of the systematic deviation observed and the statistical error from the monitored independent sample. This procedure is followed in a systematic way for the studies listed below and its description will of course not be repeated each time.

Finally, the systematic deviations for each study are obtained with their sign in each measured decay channel, thus providing the full information on the correlations between the results and allowing the corresponding covariance matrix to be constructed.

10.2   Selection of $\tau\tau$ events

Selection efficiencies of all the dominant channels have been determined from data using the break-mix method as discussed in Section 3.2. The efficiencies are very similar for the different data sets. They are listed in Table 9 for the 1994-1995 sample.

The obtained values are then allowed to float around the nominal values with their corresponding errors, and 1000 toy experiments are generated to estimate the effect on the branching ratios. The errors are listed in Table 11 in the column 'sel'.

10.3   Non-τ background

Most non-τ background contributions in each τ decay channel have been measured directly in data following the procedure described in Section 3.3. The contamination from hadronic Z decays has been determined by Monte Carlo simulation. In that case the relative error of non-τ background is taken as 30%. Toy experiments are used where new values for the non-τ background are generated according to Gaussian distributions with the measured error. Branching ratios are reevaluated in each case and the resulting standard deviations are quoted as errors. They are given in Table 11 in the column 'bkg'.

10.4   Particle identification

The same technique is used to estimate the systematic error on particle identification and misidentification efficiencies which are obtained from measurements on control samples (see Section 4.2) with their own statistical and systematic uncertainties. The errors on the branching ratios are listed in Table 11 in the column 'pid'.

10.5   Photon detection efficiency

Photon detection efficiency at low energy and high energy are studied by different means.

10.5.1   Photon efficiency at low energy

The number of real photons in the data sample is obtained from the fit of the P_γ distribution in each energy bin with the distributions of genuine and fake photons from Monte Carlo sample. The energy spectra of genuine photons for both data and Monte Carlo samples are then compared in order to obtain the relative photon efficiency between data and Monte Carlo (Fig. 20). Some discrepancy is observed at low energy, indicating that the efficiency in the data sample is different from the simulation. It should be emphasized that this effect originates almost exclusively from the detector simulation which was improved for the 1994-1995 sample. It is taken into account in the analysis by randomly killing Monte Carlo photons in the corresponding energy bins. The error on the efficiency is propagated to the final branching ratios and are given in Table 10 in the column 'eff'.

One could question whether the above effect is indeed related to the simulation of photon efficiency or rather induced by different physics in data and in simulation. The fact that the first explanation is the correct one is made clear by the following observations: (1) the discrepancy occurs only near photon-detection threshold with a characteristic shape, (2) the branching ratio values are adjusted in the Monte Carlo to match those measured in data, (3) the effect is observed in all photonic classes, and (4) the effect is quantitatively different in the barrel and endcap parts of ECAL.

The efficiency is measured for 1991-1993 and 1994-1995 samples separately, and the values are found to be different for 1-prong and 3-prong τ decays, which is reasonable considering the different environment of hadronic interactions in ECAL. The efficiencies in the ECAL barrel and endcaps are also measured separately, because the photon performance is quite different in the endcaps due to more material present in front of the calorimeter.

10.5.2   Photon efficiency at high energy

A loss of high energy photons occurs because of the merging of their showers into nearby charged track clusters. Photon reconstruction requires a cut on d_c at 2 cm in order to separate the photon candidate from the charged track cluster. The corresponding loss
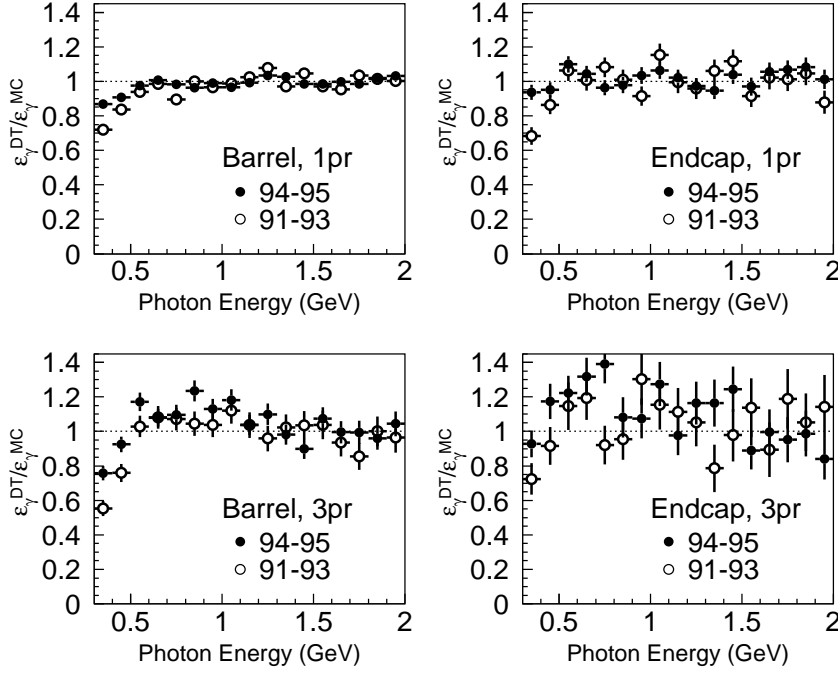
Figure 20: Relative photon efficiency in data and Monte Carlo for 1991-1993 (open circles) and 1994-1995 (black dots) data sets. The plots are separated for the barrel and endcap sections of the calorimeter, and for one- and three-prong τ decays.

Table 10: Systematic error for photon and π^0 reconstruction in 1994-1995 data sample. All numbers are absolute branching ratios in %. The labels are defined as follows: photon efficiency at low energy (eff), photon efficiency at high energy (dgt), converted photons (cnv), photon identification efficiency (prb), photon energy calibration (cal), fake photon correction (fak), π^0 reconstruction efficiency (dij), bremsstrahlung and radiative photons (bms). The total π^0 systematic uncertainty is given in the rightmost column.

Topology	eff	dgt	cnv	prb	cal	fak	dij	bms	total π^0
e	0.006	0.002	0.005	0.000	0.004	0.003	0.005	0.003	0.011
μ	0.002	0.001	0.001	0.000	0.002	0.000	0.001	0.002	0.004
h	0.022	0.029	0.006	0.056	0.009	0.011	0.002	0.019	0.071
$h\pi^0$	0.015	0.011	0.009	0.024	0.011	0.048	0.006	0.023	0.063
$h2\pi^0$	0.033	0.013	0.013	0.041	0.018	0.048	0.025	0.038	0.089
$h3\pi^0$	0.012	0.019	0.010	0.035	0.014	0.008	0.030	0.013	0.056
$h4\pi^0$	0.017	0.012	0.005	0.012	0.006	0.010	0.007	0.007	0.029
$3h$	0.028	0.012	0.007	0.029	0.010	0.012	0.005	0.011	0.046
$3h\pi^0$	0.004	0.003	0.010	0.014	0.006	0.020	0.010	0.017	0.033
$3h2\pi^0$	0.016	0.010	0.008	0.012	0.006	0.008	0.003	0.007	0.027
$3h3\pi^0$	0.002	0.004	0.003	0.004	0.003	0.002	0.005	0.004	0.010
$5h$	0.001	0.001	0.000	0.001	0.000	0.000	0.000	0.001	0.002
$5h\pi^0$	0.001	0.000	0.001	0.001	0.001	0.000	0.001	0.001	0.002
Class 14	0.008	0.004	0.004	0.002	0.003	0.002	0.004	0.006	0.013
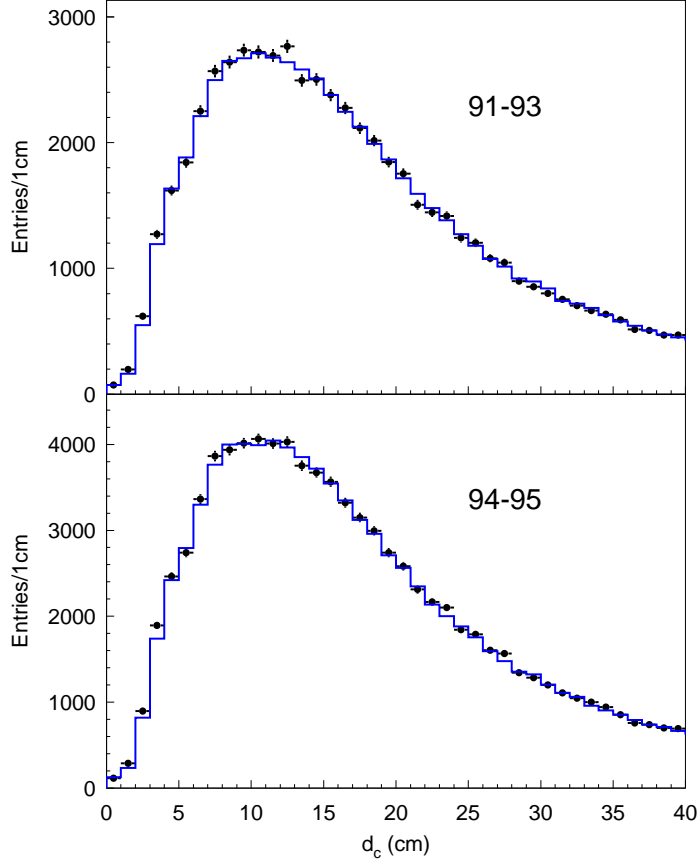
Figure 21: Comparison of d_c distributions for high energy photons ($E_\gamma > 3\ GeV$) in data (points) and in Monte Carlo (histogram) for 1991-1993 and 1994-1995 data sets. The distributions are normalized to each other for $d_c > 8$ cm.

of efficiency depends on the simulation of hadronic interactions in ECAL, which can be checked against data by comparing the actual d_c distributions. Figure 21 shows the comparison for photons with energy greater than 3 GeV. After normalization to $d_c \geq 8$ cm, the fraction of photons below 8 cm is $(0.30 \pm 0.15)\%$ more in data for 1991-1993 and is $(0.37 \pm 0.13)\%$ more in data for 1994-1995.

The observed difference is applied in the analysis and varying it by one standard deviation provides an estimate of the systematic error induced by the d_c cut. The errors are listed in Table 10 in the column 'dgt'.

10.6 Converted photons

The rate of reconstructed converted photons depends on the conversion probability and the misidentification of hadronic tracks in a multihadron environment. The misidentification of protons originating from nuclear interactions should also be considered in this context since their energy loss by ionization can be close to that expected for electrons in the low momentum range.

45
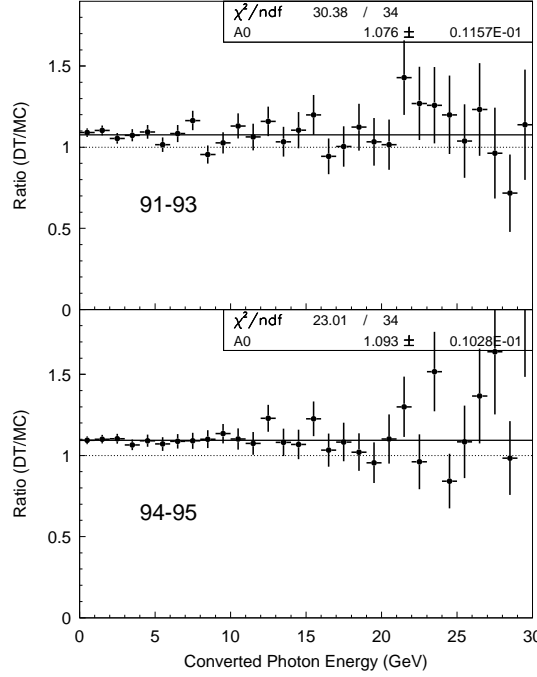
Figure 22: Ratio of converted photon energy spectra in data and Monte Carlo.

Figure 22 shows the ratio of converted photon spectra in data and Monte Carlo, indicating an inadequate simulation of the rate of converted photons. Since in the analysis converted photons are given an identification probability of 1, the net effect is an efficiency increase for photons in data. To correct for this, some converted photons in the data sample are randomly declared to be calorimeter photons according to the observed excess and given an identification probability value according to the corresponding ECAL photon distribution. Their fate in the analysis thus follows that of the ordinary calorimetric photons which can be removed when probability cuts are applied.

The error on the conversion rate ratio is propagated to branching fractions through a full reanalysis. The corresponding systematic errors are listed in Table 10 in the column 'cnv'.

The misidentification of hadrons to electrons in a multihadron environment is measured by comparing events reconstructed as $3h\pi^0$ with two tracks identified as hadrons and one reconstructed converted photon: this sample is dominated by produced $3h$ events with one hadronic track misidentified as electron. Comparing the event numbers in data and Monte Carlo after normalization to the total τ event number, the rate of hadron misidentification is found to be $(0.06 \pm 0.03)\%$ lower in simulation for the 1994-1995 data sample, corresponding to an absolute change in the $3h$ fraction of $(+0.010 \pm 0.005)\%$. A bigger difference is observed in the 1991-1993 data sample where the misidentification probability is found to be $(0.25 \pm 0.04)\%$ lower in the Monte Carlo. This problem only affects feedthrough between nearby 3-prong channels, the largest correction being to the $3h$ channel, $(+0.034 \pm 0.007)\%$, while the effect on $3h\pi^0$ and $3h2\pi^0$ modes is $(-0.019\pm0.004)\%$ and $(-0.015\pm0.003)\%$, respectively. The found difference is illustrated in Fig. 23 where a comparison of the data and Monte Carlo distributions of the momenta
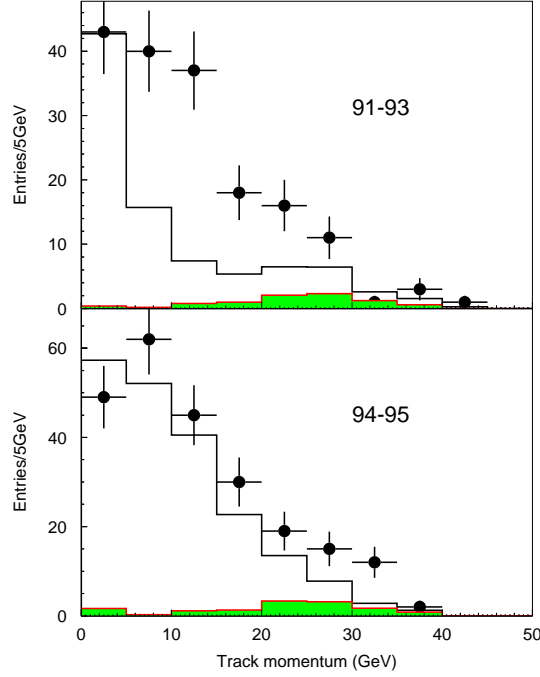
Figure 23: Comparison of hadron misidentification in multihadronic final states (see text for details). Data are given by points and Monte Carlo by histogram, while the shaded histogram shows the contribution from non-τ background. A clear improvement is observed in the 1994-1995 simulation.

of the converted photons is shown. The error of this correction is included under 'cnv' in Table 10.

Proton tracks are observed when hadrons interact with the material of the inner detectors. Since at low energy, only dE/dx information is used for particle identification, protons can be misidentified as electrons for momenta between 0.9 and 1.1 GeV, as seen in Fig. 24. By selecting tracks with large dE/dx at even lower momenta so that protons dominate the sample, the proton rates can be compared in data and in simulation directly. Good agreement is observed and the systematic error on τ branching ratios from proton tracks in the photon conversions is negligible.

10.7   Photon identification efficiency

Since the reference distributions for photon identification are not exactly the same for data and Monte Carlo (even after corrections), the same probability cut will have different efficiencies for the two cases. Figure 25 shows the comparison of P_γ distributions between data and simulation for residual photons in the 0.3-3.0 GeV range: good agreement is observed overall, however some small shape differences can be seen. A comparison of the same distributions is performed for photons in small energy slices, after correcting the branching ratios in the Monte Carlo and for the non-τ background. The numbers of photons surviving the cut are compared, and the efficiency is found to be a little larger in the simulation. This effect is then corrected in the analysis by using a slightly tighter cut
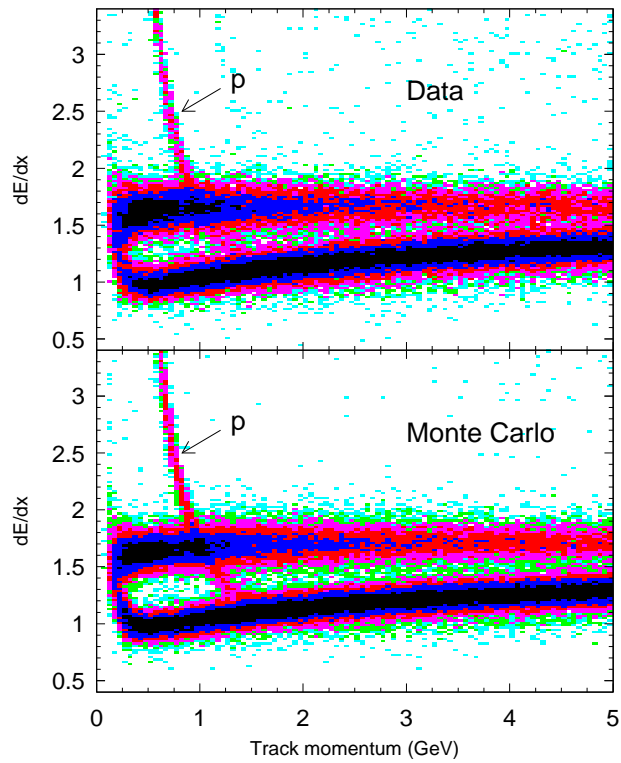
Figure 24: Measured dE/dx as a function of momentum for all (good and bad) tracks in the selected τ sample: the proton band from nuclear interactions is clearly observed, and predicted by the simulation.
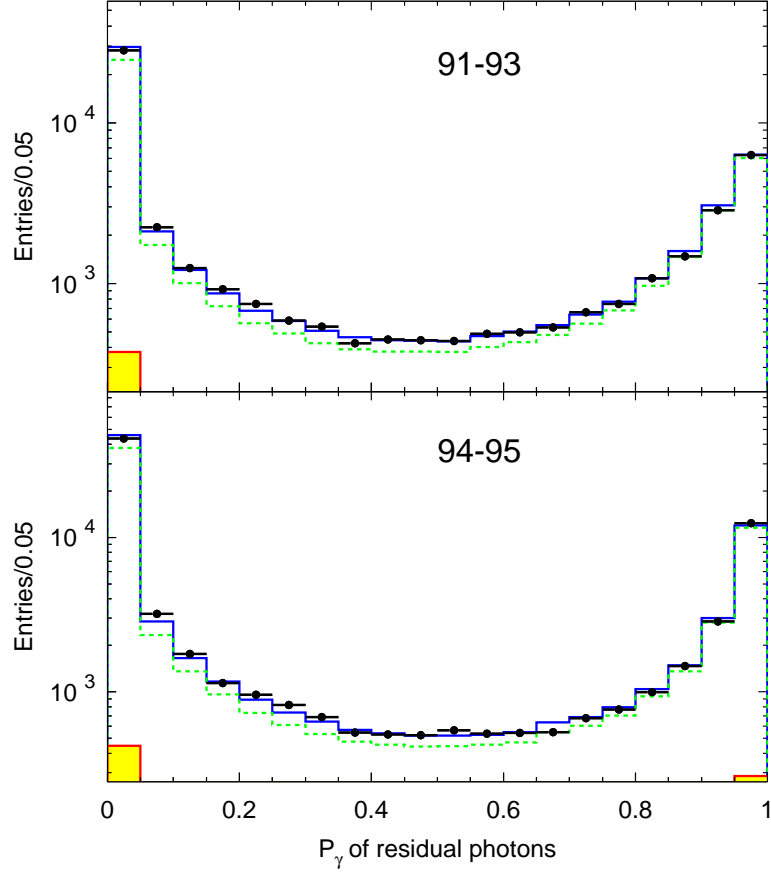
Figure 25: Comparison of photon identification probability distributions in data (points) and Monte Carlo (solid histogram, after fake photon correction) for residual photons in the 0.3-3.0 GeV energy range. The dashed histogram shows the simulated distribution before fake photon correction, and the shaded histogram indicates the contribution of non-τ background.

for the simulation, corresponding to the observed difference in the numbers of accepted photons. The systematic errors on branching ratios appear in Table 10 in the column 'prb'.

10.8 Photon energy calibration

The photon energy scale relative to the simulation is calibrated using high energy electrons from τ decays as discussed in Section 5.2.5. The parameterization of the E/p ratio is extrapolated to low energy for both data and Monte Carlo. The error on the calibration factors is propagated to branching ratios and are listed in Table 10('cal').

49

10.9   Fake photon correction

The error on the fake photon correction comes from the uncertainty in measuring the total number of fake photons in each observed class for data, and in determining the fake photon multiplicity in each generated Monte Carlo event, using the matching procedure described in Section 8.2. The latter has a negligible effect on branching ratios since the dependence of the efficiency matrix on the fake photon multiplicity is weak. The fake photon numbers are determined from fits to the P_γ distributions, and the errors are obtained in the global fit of the fake photon correction factors. These errors are then propagated to branching ratios. To reduce the total number of parameters the correction factors on low branching ratio channels are assumed to be equal to those of the nearby high branching ratio channels, thus somewhat increasing the χ^2 of the fits. The fitted errors are then enlarged by the $\sqrt{\chi^2/DF}$ values in each channel. The errors are reported in Table 10 in the column 'fak'.

10.10 π^0 reconstruction efficiency

To estimate the uncertainty on the reconstruction of the resolved π^0's, a comparison of the D_{ij} (Section 6) distributions is shown in Fig. 26 after branching ratio, fake photon, and non-τ background corrections are applied in the simulation. Good agreement is observed. The agreement on the reconstruction efficiencies of resolved π^0's in data and Monte Carlo is tested with a precision of 0.17% and 0.14% for the 1991-1993 and 1994-1995 samples respectively. They can be reproduced by changing the value of the D_{ij} cut by 0.14×10^{-4} and 0.12×10^{-4} for 1991-1993 and 1994-1995 respectively, the nominal cut being set at 1×10^{-4}. The effect of changing the cut by this amount in the simulation was taken as the systematic error, listed in Table 10 in the column 'dij'.

10.11   Simulation of bremsstrahlung and radiative photons

Figure 27 shows the comparison of the energy spectra of selected radiative and bremsstrahlung photons in data and simulation after normalization to the total number of τ events. Reasonable agreement is found except for the radiative photon spectrum in the 1991-1993 sample, where more photons are found in the simulation. A comparison of 1991-1993 and 1994-1995 simulated samples clearly shows that too many radiative photons were produced in 1991-1993 at the generator level (Fig. 28). To correct for this, photons matched as radiative in the 1991-1993 Monte Carlo sample are deleted randomly according to the 1994-1995 distribution, which agrees with data. The angle between the radiative photon and the jet axis is also taken into account in this procedure.

The statistical error in the measurement of the numbers of radiative and bremsstrahlung photons is propagated to the τ branching ratios and listed in Table 10 in the column 'bms'.

It turns out that most of the bremsstrahlung photons originate from radiation in the detector material by electrons in the decay $\tau^- \rightarrow \nu_\tau e^- \overline{\nu}_e$. The comparison in Fig. 27
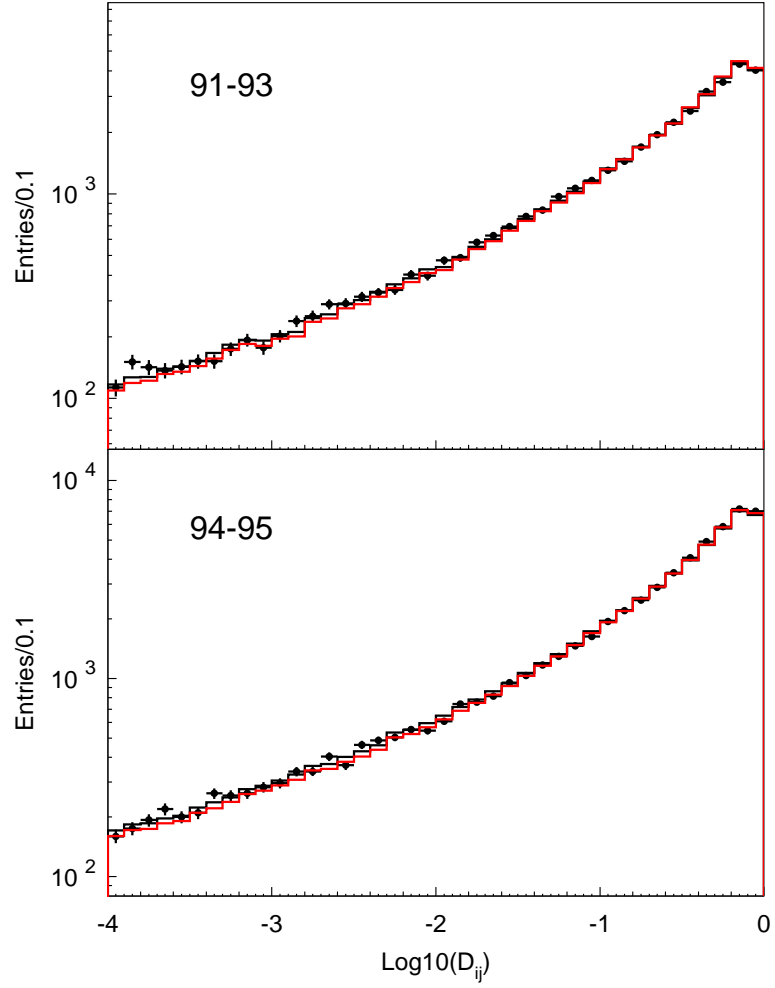
Figure 26: Comparison of D_{ij} distributions in data (points) and simulation (dark histogram) for 1991-1993 and 1994-1995 data sets. The light histograms show the distribution before fake photon correction.
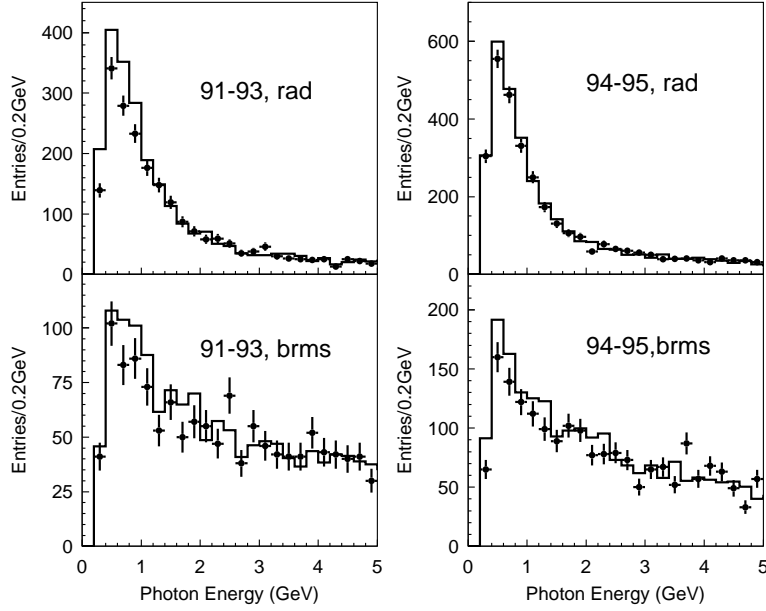
Figure 27: Comparison of measured energy spectra of bremsstrahlung and radiative photons in data (points) and Monte Carlo (histogram) for 1991-1993 and 1994-1995 data sets.
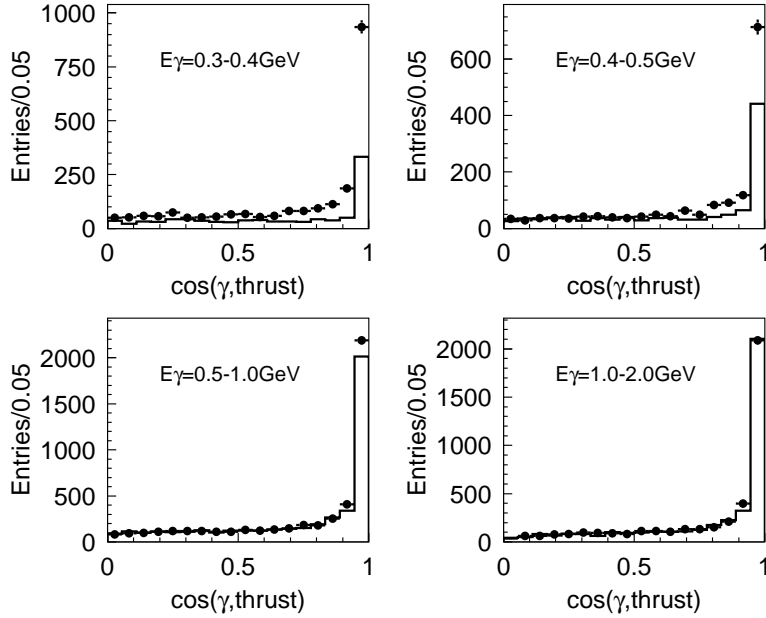
Figure 28: Comparison of the angle between produced radiative photons and jet axis in 1991-1993 (points) and 1994-1995 (histogram) simulated samples for different energy slices.

shows that the description of radiation is adequate in the simulation. However, any difference at this level would only affect the electron momentum spectrum, but not the decay classification.

The situation is more delicate for radiative photons in hadronic decay channels. From simulation, it is found that only 23% of these photons are recognized as such, while the purity in the identified radiative photon sample is about 55% (others photons are either fake or originating from π^0 decays). These values are weakly dependent on the decay channel. Since the simulation is relied upon for the unobserved radiative photons, it is important to validate the radiation procedure in the simulation.

In KORALZ07 [17] a model for radiation based on PHOTOS [22] is implemented: charged particles independently emit photons according to a bremsstrahlung probability. A test of this model can be performed in the $\pi\pi^0$ channel where a complete calculation of radiative corrections exists [24]. If a photon is radiated by either the ρ or the charged π, then the final state can be identified as $\pi\pi^0$ if the radiative photon is classified as a bremsstrahlung or radiative photon, or undetected. Otherwise such a decay would be (wrongly) classified in the $\pi 2\pi^0$ class and the corresponding bias should be corrected for through the simulation. It is thus important to verify the radiation model against the full calculation. A good agreement is found for the radiative rate for photon energies E_γ^* above 12 MeV in the τ centre-of-mass frame, comparable to the detection threshold of 350 MeV in the e^+e^- frame: the simulation using PHOTOS yields a radiative branching ratio of $(2.91 \pm 0.04) \times 10^{-3}$ to be compared to a value of 2.9×10^{-3} from the exact calculation. In both cases, the radiative yield includes photons emitted by the τ lepton and by the charged ρ and π in the decay. The simplified bremsstrahlung probability is however no longer adequate for hard radiation: the corresponding values for $E_\gamma^* > 300$ MeV are $(0.90 \pm 0.09) \times 10^{-4}$ for the simulation and 1.8×10^{-4} for the calculation. Although significant, such a difference has no practical influence in this analysis, since it only affects a negligible part of the radiative photon spectrum. The comparison of the total radiative yield above detection threshold leads to an absolute systematic error of 0.005% on the branching ratio in the $\pi\pi^0$ channel, a factor of 3 to 4 smaller than the estimated uncertainties quoted in Table 10 from the direct data/simulation comparison of the radiative photon spectra. The latter values are therefore retained as final uncertainties for this source.

10.12   Simulation of π^0 Dalitz decays

The simulation of the π^0 Dalitz decays is checked at the generator level. Good agreement is found with the world average branching ratio. The quality of the simulation of π^0 Dalitz decays can also be checked in the distribution of the reconstructed photon conversion point near interaction point which agree well with data (Fig. 16). The possible systematic effect in the simulation of π^0 Dalitz decays on the τ branching ratios is found to be negligible.

Table 11: Total systematic errors for branching ratios measured from the 1994-1995 data sample. All numbers are absolute in per cent. The labels are defined as follows: photon and π^0 reconstruction (π^0), event selection efficiency (sel), non-τ background (bkg), charged particle identification (pid), secondary interactions (int), tracking (trk), Monte Carlo dynamics (dyn), Monte Carlo statistics (mcs), total systematic uncertainty (total).

Topology	π^0	sel	bkg	pid	int	trk	dyn	mcs	total
e	0.011	0.021	0.029	0.019	0.009	0.000	0.000	0.015	0.045
μ	0.004	0.020	0.020	0.021	0.008	0.000	0.000	0.015	0.039
h	0.071	0.016	0.010	0.022	0.022	0.014	0.000	0.019	0.083
$h\pi^0$	0.063	0.027	0.019	0.011	0.045	0.009	0.000	0.027	0.090
$h2\pi^0$	0.089	0.021	0.014	0.004	0.007	0.003	0.040	0.028	0.105
$h3\pi^0$	0.056	0.012	0.015	0.000	0.008	0.001	0.008	0.030	0.068
$h4\pi^0$	0.029	0.005	0.011	0.000	0.015	0.000	0.000	0.019	0.040
$3h$	0.047	0.021	0.018	0.004	0.012	0.014	0.006	0.015	0.059
$3h\pi^0$	0.033	0.017	0.029	0.002	0.041	0.009	0.007	0.018	0.066
$3h2\pi^0$	0.027	0.008	0.015	0.000	0.009	0.003	0.012	0.014	0.038
$3h3\pi^0$	0.010	0.012	0.002	0.000	0.002	0.001	0.010	0.006	0.019
$5h$	0.002	0.000	0.002	0.000	0.000	0.001	0.000	0.003	0.004
$5h\pi^0$	0.002	0.000	0.006	0.000	0.000	0.000	0.000	0.002	0.007
Class 14	0.013	0.003	0.022	0.002	0.024	0.000	0.000	0.011	0.037

10.13 Nuclear interactions

Secondary interactions of charged hadrons produced from τ decays with material in the inner part of the detector are studied with the help of an enriched sample. Interaction events are characterized by the presence of many bad tracks and proton tracks. By requiring more than three bad tracks in the hemisphere or at least one proton track identified with energy loss information, interaction events are selected with an efficiency of about 50% and a purity of 70%, as estimated from the simulation.

Figure 29 shows the comparison of data to Monte Carlo of the observed τ decays in each reconstructed class for this interaction-rich sample, after normalizing to the total number of τ events. Globally it is found that the MC overestimates the rate for secondary interactions by about 10%, with some channel-to-channel variation.

By comparing the total number of interaction events in data and simulation, the difference of interaction rates is measured and corrected, modifying the efficiency matrix slightly. The branching ratios are then reevaluated with this new efficiency matrix. The differences between the new branching ratios and those without correction are taken as the conservative estimate of the systematic error from the simulation of nuclear interactions. This procedure is justified by the fact that, although the rate differences can be well measured, it does not ensure that the interaction dynamics is properly simulated. As shown in Fig. 29, even after the applied global rate correction the agreement between data and Monte Carlo, although much improved, remains not very satisfactory.

Another approach to study the influence of secondary interactions relies on the
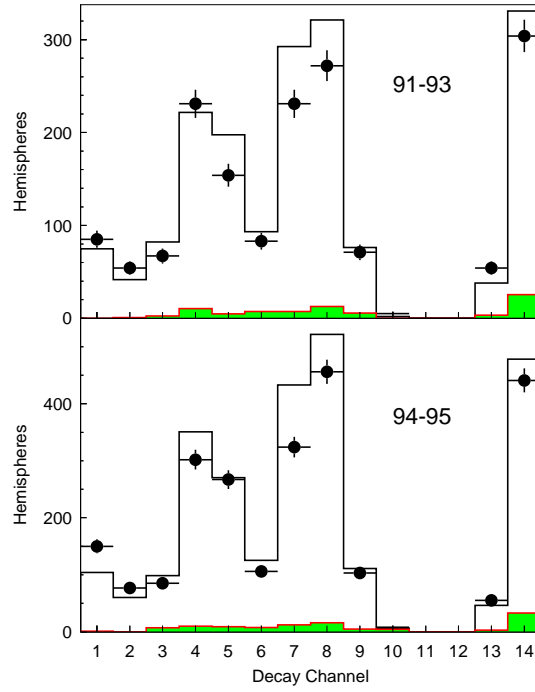
Figure 29: Comparison of the numbers of selected τ decays with secondary interactions for each channel (see Table 3 in data (points) and Monte Carlo (histogram)). The shaded part gives the contribution from non-τ background, mainly from $Z \rightarrow q\bar{q}$ events. The secondary tracks found in leptonic channels (classes 1 and 2) originate from the opposite (hadronic) decay.
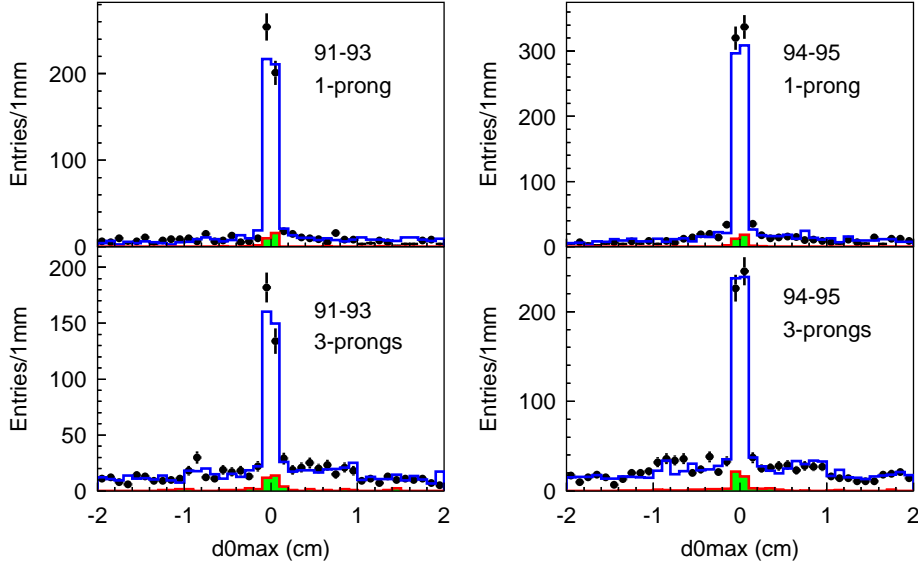
Figure 30: Comparison of the distributions of the maximum d_0 value for selected τ decays with secondary interactions in data (points) and Monte Carlo (histogram), the shaded part shows the contribution from non-τ background, mainly from $Z \rightarrow q\bar{q}$ events. The global interaction rate difference has been corrected for.

distribution of the distance in the transverse plane between the extrapolated track and the interaction point. Figure 30 shows the corresponding comparison of data to simulation (in three-prong channels, the largest of the three distances is plotted). After the global interaction rate correction, good agreement is observed for both one-prong and three-prong channels for 1991-1993 and 1994-1995 data sets, thus corroborating the findings of the other study.

The errors are listed in Table 11 in the column 'int'.

10.14   Tracking

The only situation where tracking efficiency is relevant occurs in a three-prong decay when two of the tracks are lost. This effect can be studied by looking at events with same sign hemispheres. In order to reduce the effect of secondary interactions and asymmetric photon conversions, the requirements of no proton track in both hemispheres, less than four bad tracks and no track classified as converted photon, are made. In this way 121 ± 9 events are obtained in the Monte Carlo sample after normalizing to the total τ events in the 1994-1995 data sample. The efficiency of measuring same sign events resulting from tracking is found to be 55% in simulation with a purity of 60%, the remainder being dominated by one-prong τ decays with nuclear interactions. The corresponding number from the data sample is 180 ± 13, significantly larger than the rate seen in the simulation. Taking into account the corrected simulation rate of nuclear interactions as determined in the preceding section, the data sample produces an estimated excess of $(81 \pm 24)\%$ same sign hemispheres compared to the simulation. This value corresponds to a tracking

efficiency difference of $(0.3 \pm 0.1)\%$ between data and simulation. This correction is applied to the efficiency matrix element corresponding to produced three-prong τ decays reconstructed as 1-prong, which increases by about 40%, only about half of the three-prong τ decays reconstructed as one-prong are due to tracking efficiency, the another half originating from $K_s^0 \rightarrow \pi^+\pi^-$ decays with their secondary vertex far from the interaction point. The efficiency of three-prong to three-prong decays is decreased accordingly. The error on the tracking efficiency is propagated to the τ branching ratio measurement. The largest correction in the branching ratios due to tracking is in the h channel, which decreases by $(0.047 \pm 0.014)\%$ absolutely, while the $3h$ channel correspondingly increases by the same amount.

The same analysis gives (104 ± 7) same sign hemisphere events in 1991-1993 Monte Carlo sample, while (109 ± 10) events are observed in data, thus these are in good agreement. Following the same procedure, the excess of misreconstructed events in the data sample is $(9\pm21)\%$. No correction is taken into account this time and the systematic uncertainty is evaluated in the same way as for 1994-1995 sample.

The errors are shown in Table 11 in the column 'trk'.

10.15   Dynamics

Uncertainties in the dynamics of the hadronic τ decays can lead to systematic biases when computing the efficiency matrix from the simulation. The fact that selection efficiencies are large and weakly dependent on the hadronic invariant mass is an important factor limiting those biases. Nevertheless systematic checks have been performed, comparing the measured mass distributions in all reconstructed channels to their simulated counterparts.

Some small differences are observed in the $3h$ and $h2\pi^0$ channels. However no new evaluation of this systematic uncertainty was done for this analysis as it is not dominant. The result is taken from the published paper on 1991-1993 data [3] which was based on detailed tests of several models describing the a_1 resonance. Similarly, systematic uncertainties were derived for the higher multiplicity modes by comparing decay models with different resonance contributions in the final states. Finally the effect of τ polarization on the efficiency matrix is estimated to be negligible.

The corresponding errors are listed in Table 11 in the column 'dyn'.

10.16   Monte Carlo statistics

Multinomial fluctuations for each generated class in the Monte Carlo sample using the measured fractions of events in each reconstructed class are included in the efficiency matrix uncertainties. Generating 1000 sets of efficiency matrices, the RMS of the branching ratio values are obtained and taken as the uncertainty from the finite Monte Carlo statistics. It is shown in Table 11 in the column 'mcs'.

10.17 Total systematic errors

Assuming that all the above systematics from specific sources are uncorrelated, the total systematic error is computed for each channel. The final values are listed in the last columns of Table 11. Correlations exist between different channels for a given source of systematics: the correlation matrix for the total systematic uncertainties is given in Section 13.3.

11 Global systematic checks

After taking into account all the corrections to the simulation (measured τ branching ratio values, fake photon simulation, ...) and including non-τ backgrounds, some distributions are compared in data and Monte Carlo in order to provide global checks of the consistency between data and simulation. Of course such tests cannot be taken literally as they could reveal some difference in the τ decay dynamics in some channel, however such effects are expected to be small as most τ decay channels are well understood from the basic principles of the Standard Model. This comparison is done for the distributions of charged particle momenta, of photon and π^0 energies and of the hadronic invariant mass spectra for each τ decay mode.

11.1 Charged particle momentum distributions

The only accessible observable in the leptonic channels is the lepton momentum. Figures 31 and 32 show the respective track momentum distributions for electrons and muons. They are in good agreement with the simulation including backgrounds and the Standard Model spectrum.

The charged hadron momentum distribution is shown in Fig. 33. Good agreement is observed between data and the simulation.

11.2 Photon energy distribution

The comparison of photon energy spectra in data and Monte Carlo is shown in Figs. 34 and 35 for 1991-1993 and 1994-1995 data sets respectively. Good agreement is observed except for the largest energies. This effect is understood as coming from the correction of saturation and leakage which is applied to single clusters in data, while no such correction is done in the simulation. This procedure is incorrect for unresolved π^0's not recognized as such, since the correction is applied to the resulting shower rather than to the two merged individual photonic showers, leading to an overestimate of the π^0 energy. This shortcoming has no effect on the branching ratio measurement. The agreement between data and Monte Carlo at low energy after fake photon correction shows that the procedure is reliable, since no energy information was used in the fake photon correction procedure.
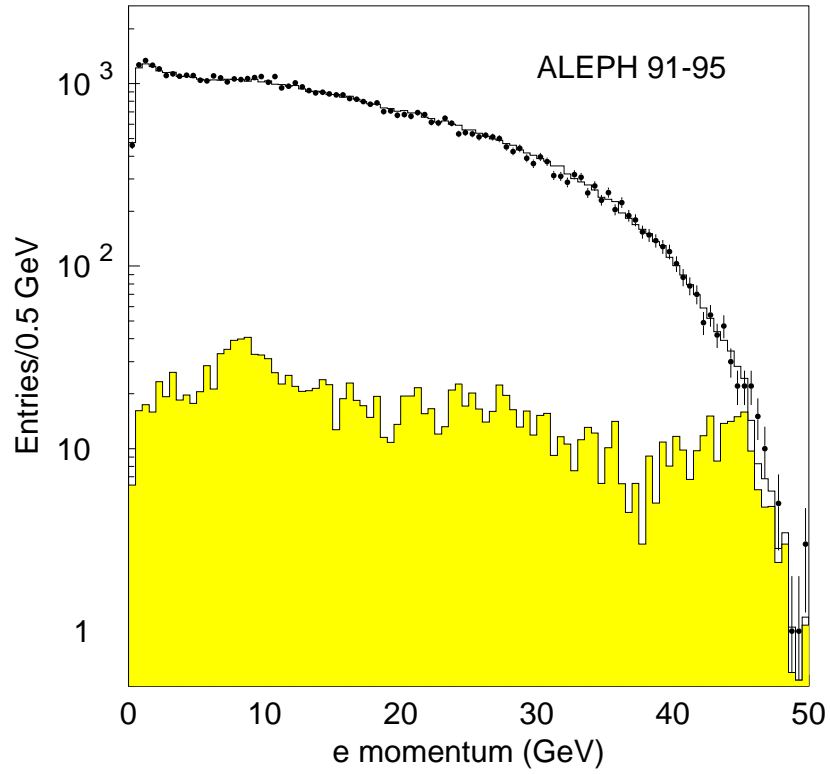
Figure 31: Comparison of electron momentum spectra in data (points) and simulation (histogram) for the full 1991-1995 data sample. The shaded histogram is the contribution of non-τ background.
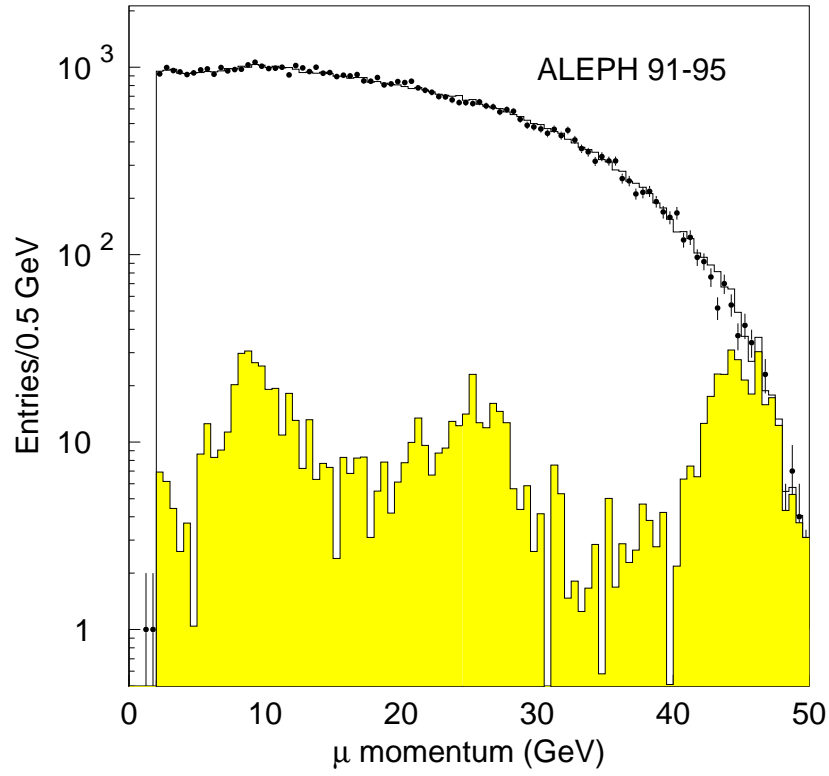
Figure 32: Comparison of muon momentum spectra in data (points) and simulation (histogram) for the full 1991-1995 data sample. The shaded histogram is the contribution of non-τ background.
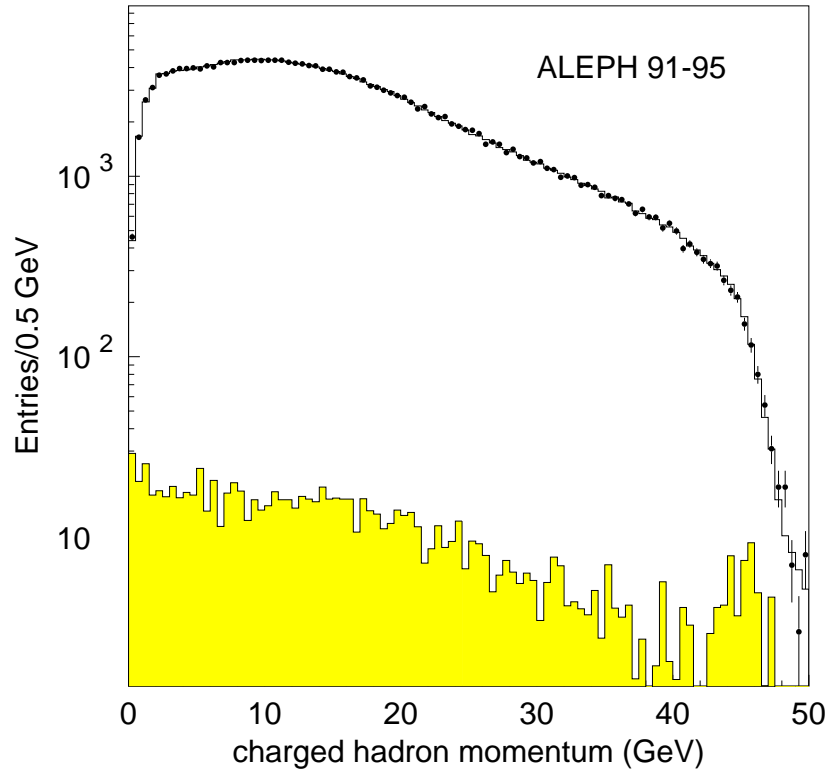
Figure 33: Comparison of charged hadron momentum spectra in data (points) and simulation (histogram) for the full 1991-1995 data sample. The shaded histogram is the contribution of non-τ background.

Figure 34: Comparison of photon energy spectra for all τ events in data (points) and simulation (histogram) after all the corrections for 1991-1993 data set. The dotted line shows the simulated distribution before correction and the shaded histogram is the contribution of non-τ background.
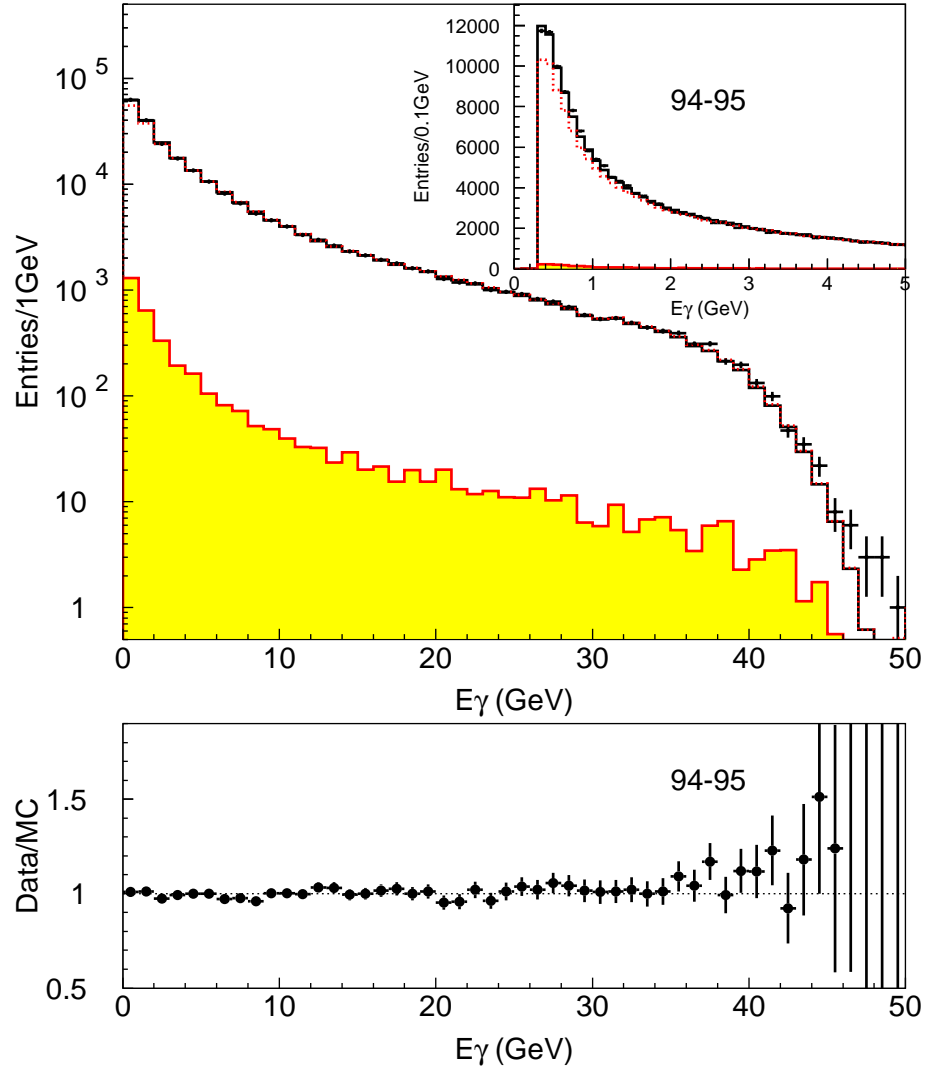
Figure 35: Comparison of photon energy spectra for all τ events in data (points) and simulation (histogram) after all the corrections for 1994-1995 data set. The dotted line shows the simulated distribution before correction and the shaded histogram is the contribution of non-τ background.

11.3 π^0 energy distribution

The comparison of π^0 energy spectra in data and Monte Carlo is shown in Figs. 36 and 37 for 1991-1993 and 1994-1995 data sets respectively. Good agreement is observed except at energies below 1 GeV for the 1994-1995 data and for the highest energies. The former discrepancy is within the quoted systematic uncertainty for $\gamma - \pi^0$ reconstruction. As for high energy, the explanation is the same as for single photons since, at high energy, unresolved π^0's dominate the sample.

11.4 Invariant mass spectra in multihadron channels

The comparison of mass spectra for all τ decays in data and Monte Carlo is shown in Fig. 38 for the full 1991-1995 data set. As noticed earlier perfect agreement cannot be expected since the Monte Carlo simulation of the dynamics in some decay modes may not be accurate. Even in prominent channels like $\pi\pi^0$, 3π and $\pi 2\pi^0$, the precise shape of the mass distribution is not predicted by theory and the phenomenology of the corresponding spectral functions does, on the contrary, rely on precise measurements (see Section 15 on the measurement of spectral functions from this analysis). The long tail above the τ mass in the distribution is dominated by secondary interaction of hadronic tracks with inner detector material. Globally, the agreement is reasonable and confirms that the simulation of secondary interactions in the detector is adequate.

The comparison of mass spectra for reconstructed $h\pi^0$ events in data and Monte Carlo is shown in Fig. 39 for the full 1991-1995 data set, with the Monte Carlo predicted feedthrough from other channels and non-τ backgrounds.

12 From reconstructed classes to exclusive modes

So far branching fractions have been determined in 13 classes corresponding to major τ decay modes. However, as shown in Table 3, these classes still contain the contributions from final states involving kaons. The latter are coming from Cabibbo-suppressed τ decays or modes with a $K\overline{K}$ pair, both characterized by small branching ratios compared to the nonstrange modes without kaons.

Complete analyses of τ decays involving neutral or charged kaons have been performed by ALEPH on the full LEP 1 data [6, 7, 8]. They are summarized in Ref. [9] where measurements with K_S^0 or K_L^0 are combined. The ALEPH analyses have provided measurements of branching ratios of modes with kaons containing up to 4 hadrons in the final states. Thus they are fully adequate to cover the needs of the present analysis of the nonstrange modes.

The τ decays involving η or ω mesons also require special attention in this analysis because of their electromagnetic decay modes. Indeed the final state classification relies in part on the π^0 multiplicity, thereby assuming that all photons —except those specifically identified as bremsstrahlung or radiative— originate from π^0 decays. Therefore the non-π^0 photons from η and ω decays are treated as π^0 candidates in the analysis and the
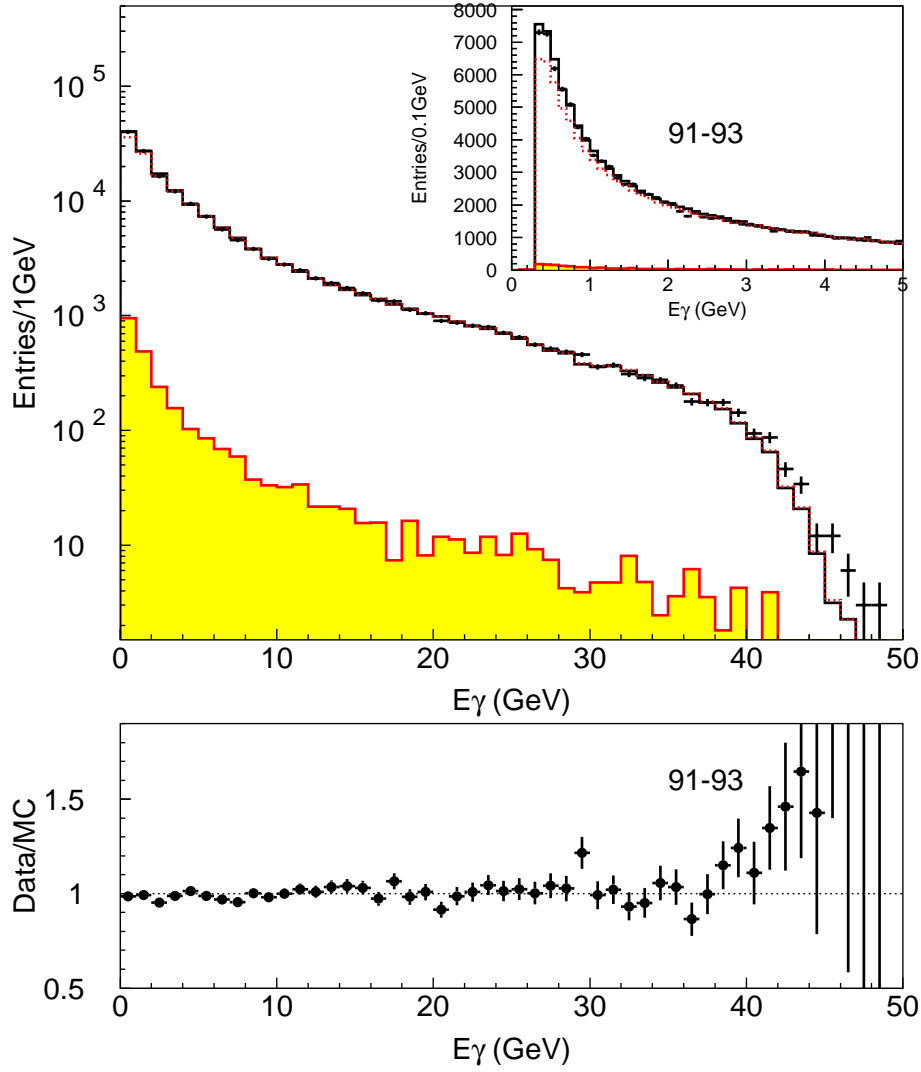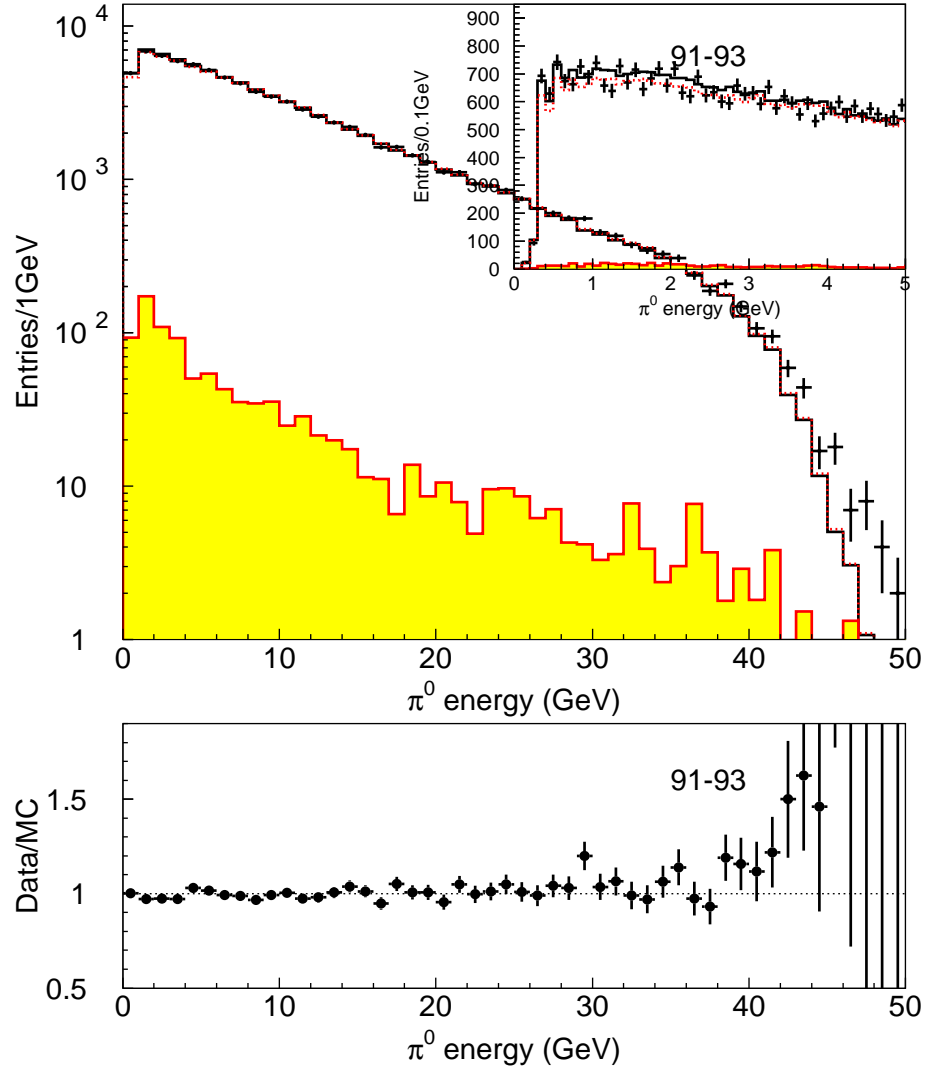
Figure 36: Comparison of π^0 energy spectra for all τ events in data (points) and simulation (histogram) after all the corrections for 1991-1993 data set. The dotted line shows the simulated distribution before correction and the shaded histogram is the contribution of non-τ background.
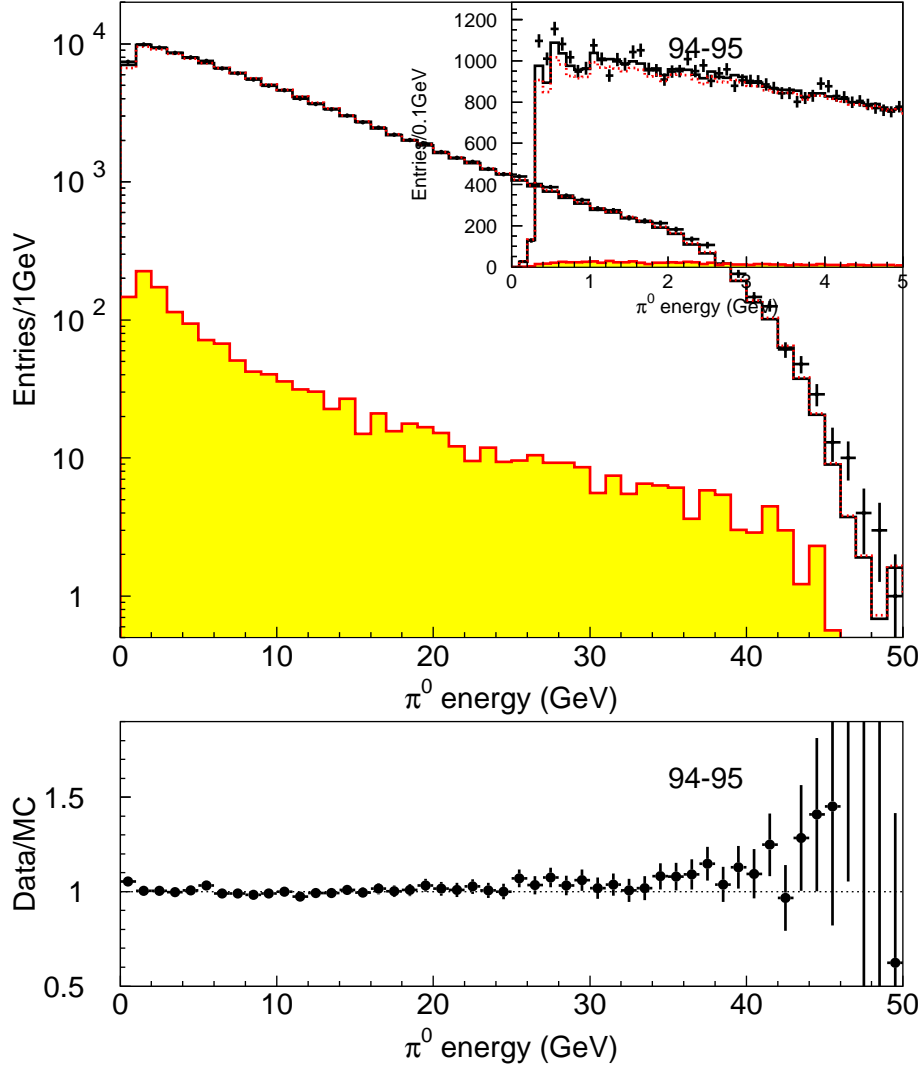
Figure 37: Comparison of π^0 energy spectra for all τ events in data (points) and simulation (histogram) after all the corrections for 1994-1995 data set. The dotted line shows the simulated distribution before correction and the shaded histogram is the contribution of non-τ background.
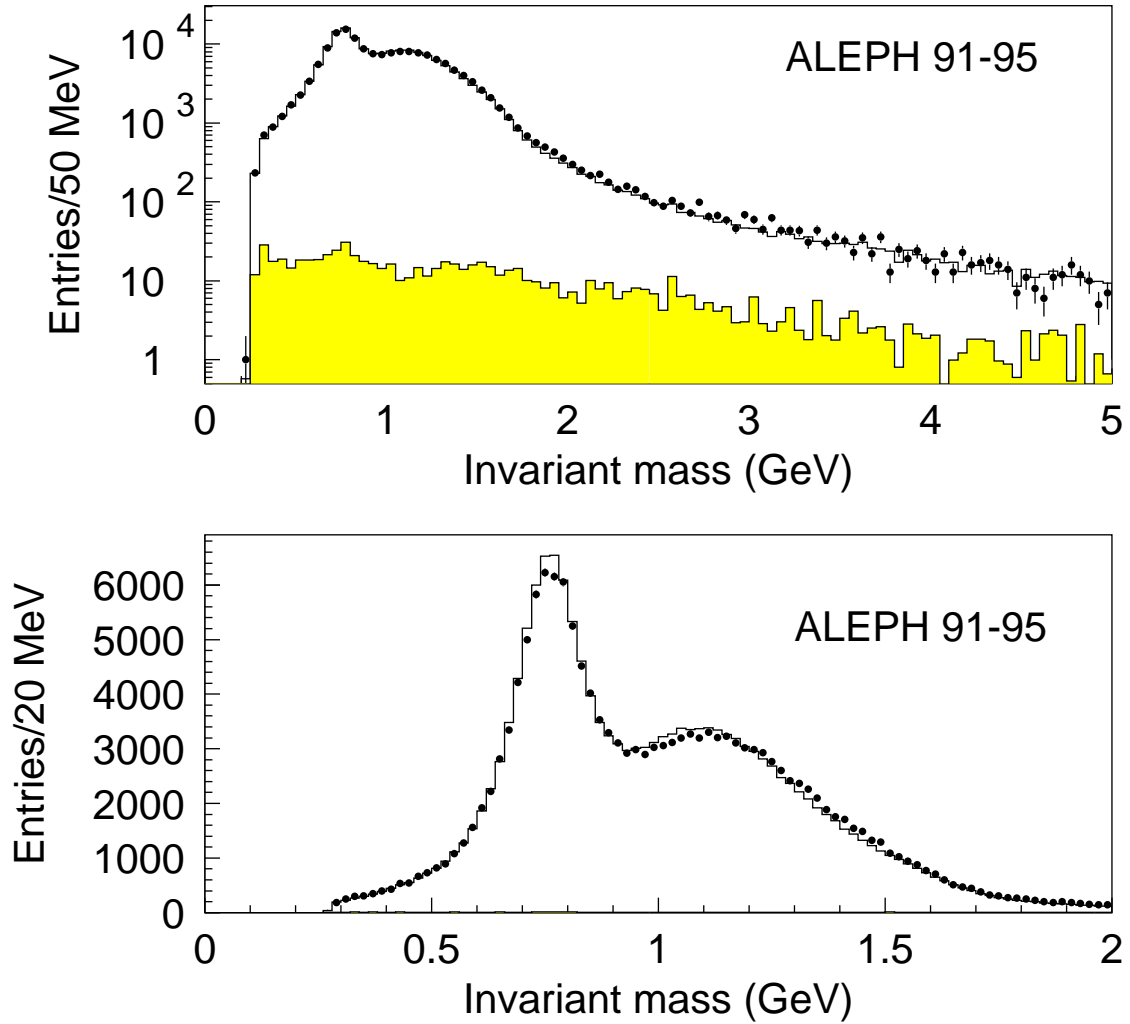
Figure 38: Comparison of mass spectra (assuming all charged particles are pions) in data (points) and simulation (histogram) after fake photon correction for all the hadronic τ decays (except single hadron) in 1991-1995 data sample. The shaded histogram is the contribution of non-τ background. The same plots are displayed in logarithmic (top) and linear (bottom) vertical scales.
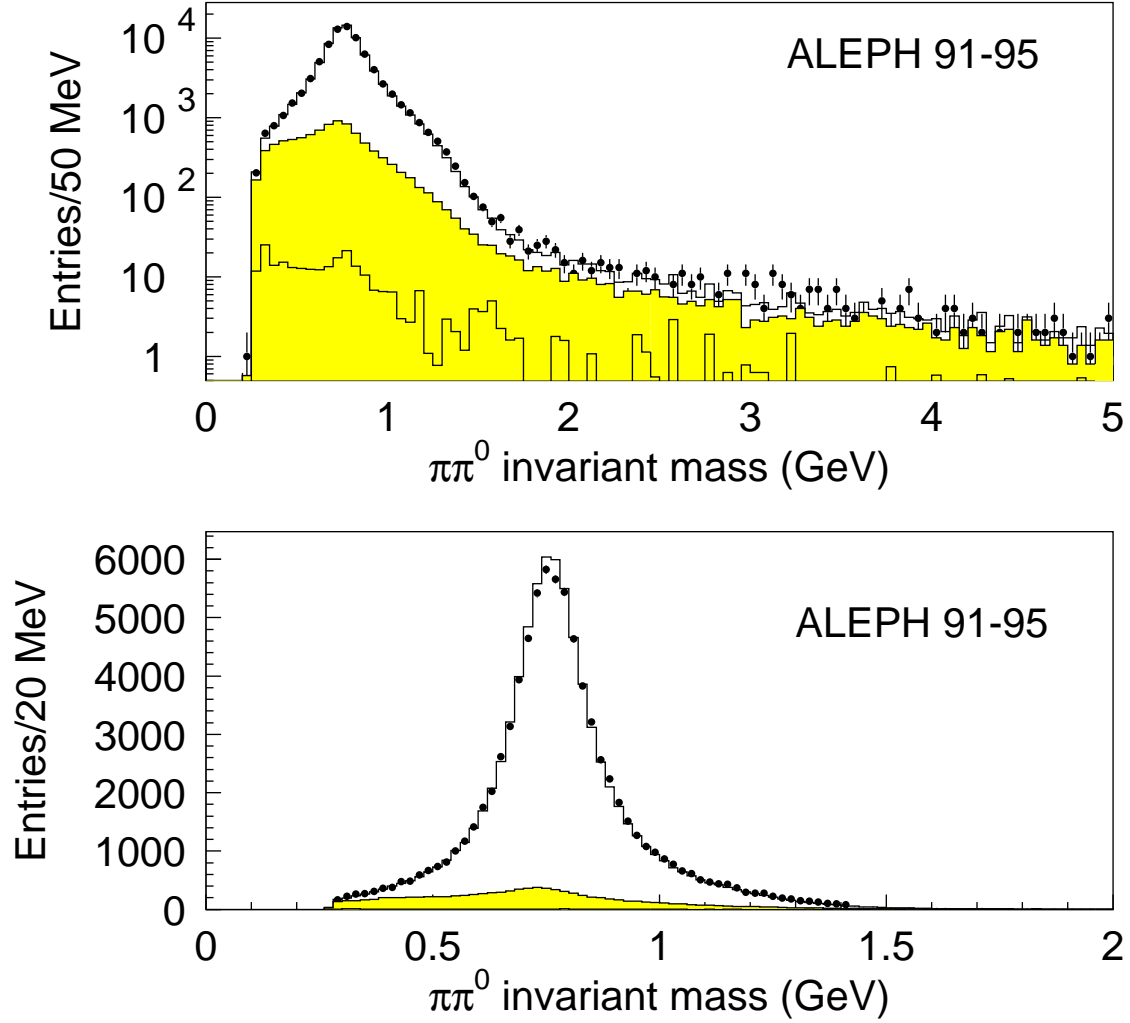
Figure 39: Comparison of hadronic mass spectra in data (points) and simulation (histogram) after fake photon correction for the $h\pi^0$ sample in 1991-1995 data. The lower shaded histogram is the contribution of non-τ background and the upper shaded is from τ feedthrough. The plots are displayed in logarithmic (top) and linear (bottom) vertical scales.

Table 12: Corrections for the exclusive nonstrange branching ratios. 'QE' and 'E' denote the quasi-exclusive (with kaons, ω and η included) and exclusive modes, respectively. Treating the ω and η contributions separately is made necessary because of their large radiative (*i.e.* with photons not originating from π^0's) modes.

QE class	E class	correction to BR (%)
e	e	-0.000 $\pm$ 0.000
μ	μ	-0.000 $\pm$ 0.000
h	π^-	-1.341 $\pm$ 0.040
$h\pi^0$	$\pi^-\pi^0$	-0.756 $\pm$ 0.038
$h2\pi^0$	$\pi^-2\pi^0$	-0.408 $\pm$ 0.030
$h3\pi^0$	$\pi^-3\pi^0$	-0.236 $\pm$ 0.032
$h4\pi^0$	$\pi^-4\pi^0$	-0.085 $\pm$ 0.016
$3h$	$\pi^-\pi^-\pi^+$	-0.770 $\pm$ 0.057
$3h\pi^0$	$\pi^-\pi^-\pi^+\pi^0$	-1.994 $\pm$ 0.100
$3h2\pi^0$	$\pi^-\pi^-\pi^+2\pi^0$	-0.480 $\pm$ 0.071
$3h3\pi^0$	$\pi^-\pi^-\pi^+3\pi^0$	-0.032 $\pm$ 0.006
$5h$	$3\pi^-2\pi^+$	-0.026 $\pm$ 0.004
$5h\pi^0$	$3\pi^-2\pi^+\pi^0$	-0.012 $\pm$ 0.002

systematic bias introduced by this effect must be evaluated. The corrections are based on specific measurements by ALEPH of τ decay modes containing those mesons [13]. Thus the final results correspond to exclusive branching ratios obtained from the values measured in the topological classification, corrected by the removed contributions from K, η and ω modes measured separately, taking into account through the Monte Carlo their specific selection and reconstruction efficiencies to enter the classification. This delicate bookkeeping takes into account all the major decay modes of the considered mesons [25], including the isospin-violating $\omega \to \pi^+\pi^-$ decay mode. The main decay modes considered are $\pi\omega$, $\pi\pi^0\omega$ and $\pi\pi^0\eta$ with branching fractions of $(2.26\pm0.18)\times10^{-2}$, $(4.3\pm0.5)\times10^{-3}$, and $(1.80\pm0.45)\times10^{-3}$ [13], respectively. The first two values are derived from the branching ratios for the $3\pi\pi^0$ and $3\pi2\pi^0$ modes obtained in this analysis and the measured ω fractions of 0.431 ± 0.033 from ALEPH [13] and the average value, 0.78 ± 0.06, from ALEPH [13] and CLEO [26], respectively.

Some much smaller contributions with η and ω have been identified and measured by CLEO [27] with the decay modes $\tau \to \nu_\tau\eta\pi^-\pi^+\pi^-$ $((2.4\pm0.5)\times10^{-4})$, $\tau \to \nu_\tau\eta\pi^-2\pi^0$ $((1.5\pm0.5)\times10^{-4})$, $\tau \to \nu_\tau\omega\pi^-\pi^+\pi^-$ $((1.2\pm0.2)\times10^{-4})$, and $\tau \to \nu_\tau\omega\pi^-2\pi^0$ $((1.5\pm0.5)\times10^{-4})$. Even though the corrections from these channels are very small they have been included for the sake of completeness. Finally, another very small correction has been applied to take into account the a_1 radiative decay into $\pi\gamma$ with a branching fraction of $(2.1\pm0.8)\times10^{-3}$ obtained from Ref. [28].

The corrections used to obtain exclusive branching ratios for the listed nonstrange modes are given in Table 12.

13 Results

13.1 Overall consistency test

Rejected τ hemispheres because of charged particle identification cuts are placed in class 14; these cuts include the 2 GeV minimum momentum and the ECAL-crack veto for some one-prong modes, and the strict definition of higher multiplicity channels. As already emphasized, this sample does not correspond to a nominal τ decay mode and should be explained by all other measured fractions in the other classes and the efficiency matrix. Thus the determination of a hypothetical signal in this class is a measure of the level of consistency achieved in the analysis.

For this determination the efficiency of the possible signal in class 14 is taken to be 100%. The results, already shown in Table 8 separately for the 1991-1993 and 1994-1995 data sets, are consistent and are combined to give $B_{14} = (0.066 \pm (0.027)_{stat} \pm (0.021)_{syst,c} \pm (0.025)_{syst,unc})\%$, where the last two errors refer to the common and uncommon uncertainties from the two data sets. With a combined error of 0.042% this value is consistent with zero and provides a nontrivial check of the overall procedure at the 0.1% level for branching ratios. It is interesting to note that this value coincides, approximately and accidentally, with the limit achieved of 0.11% at 95% CL in a direct search for "invisible" decays not selected in the 13-channel classification.

In the following it is assumed that all τ decay modes have been properly considered at the 0.1% precision level and no physics contribution beyond standard τ decays is further allowed. Thus the quantity B_{14} is now constrained to be zero.

It can be further noticed that this analysis provides a branching ratio in the $3\pi 3\pi^0$ class which is consistent with zero for both 1991-1993 and 1994-1995 data sets (see Table 8). The result is therefore given as an upper limit at 95% CL

$$B_{3\pi 3\pi^0} < 4.9 \times 10^{-4} \tag{15}$$

consistent with the measurement made by CLEO [29] yielding $B_{3\pi 3\pi^0} = (2.2 \pm 0.5) \times 10^{-4}$. The final state is dominated by η and ω resonances [29] and using other channels allows a lower limit to be obtained for this branching ratio, $(2.6 \pm 0.4) \times 10^{-4}$. In the following a value of $(3 \pm 1) \times 10^{-4}$ is used as input for this channel and the global analysis is performed in terms of the remaining 12 defined channels which are refitted. As for other channels proper subtractions are made for the contributions of modes with η which are listed separately.

13.2 Comparison of 1991-1993 and 1994-1995 results

Since the same procedure is applied for the analyses of 1991-1993 and 1994-1995 data the results must be consistent within the statistical errors of data and Monte Carlo. Table 13 shows the list of the differences of branching ratios with their expected fluctuations. Good agreement is observed with a χ^2 of 8.6 for 11 DF.

Table 13: Differences of branching ratios between 1991-1993 and 1994-1995 data samples; only the statistical errors in data and Monte Carlo are considered.

class	Δ BR (%)
e	0.040 ± 0.148
μ	0.061 ± 0.140
h	0.145 ± 0.139
$h\pi^0$	-0.186 ± 0.197
$h2\pi^0$	0.018 ± 0.178
$h3\pi^0$	-0.105 ± 0.143
$h4\pi^0$	0.065 ± 0.076
$3h$	0.163 ± 0.128
$3h\pi^0$	-0.201 ± 0.120
$3h2\pi^0$	0.046 ± 0.078
$5h$	0.006 ± 0.018
$5h\pi^0$	-0.006 ± 0.014

In conclusion the two independent data and Monte Carlo samples give consistent results. The 1994-1995 results confirm the trend of larger $h\pi^0$ and $3h\pi^0$, and smaller h and $3h$ branching ratios compared to the previous analyses, as observed in 1991-1993 data sample.

13.3   Final combined results

Finally the two sets of results are combined. Using only statistical or total weights —in the latter taking into account correlated errors from dynamics and secondary interactions— gives almost identical results. The final results obtained with the total weights are shown in Table 14.

The branching ratios obtained for the different channels are correlated with each other. On one hand the statistical fluctuations in the data and the Monte Carlo sample are driven by the multinomial distribution of the corresponding events, producing well-understood correlations. On the other hand the systematic effects also induce significant correlations between the different channels. All the systematic studies were done keeping track of the correlated variations in the final branching ratio results, thus allowing a proper propagation of errors. The full covariance matrices from statistical (from data) and systematic origins are given in Tables 15 and 16.

13.4   An independent analysis of the leptonic branching ratios

A dedicated analysis of the leptonic branching ratios has been performed as a by-product of one of the two methods used by ALEPH to measure the τ polarization and polarization

Table 14: Combined results for the exclusive branching ratios (B) for modes without kaons. The contributions from channels with η and ω are given separately, the latter only for the electromagnetic ω decays. All results are from this analysis, unless explicitly stated. The "estimates" are discussed in the text.

mode	B $\pm\sigma_{\text{stat}} \pm \sigma_{\text{syst}}$ [%]	
e	$17.837 \pm 0.072 \pm 0.036$	
μ	$17.319 \pm 0.070 \pm 0.032$	
π^-	$10.828 \pm 0.070 \pm 0.078$	
$\pi^-\pi^0$	$25.471 \pm 0.097 \pm 0.085$	
$\pi^-2\pi^0$	$9.239 \pm 0.086 \pm 0.090$	
$\pi^-3\pi^0$	$0.977 \pm 0.069 \pm 0.058$	
$\pi^-4\pi^0$	$0.112 \pm 0.037 \pm 0.035$	
$\pi^-\pi^-\pi^+$	$9.041 \pm 0.060 \pm 0.076$	
$\pi^-\pi^-\pi^+\pi^0$	$4.590 \pm 0.057 \pm 0.064$	
$\pi^-\pi^-\pi^+2\pi^0$	$0.392 \pm 0.030 \pm 0.035$	
$\pi^-\pi^-\pi^+3\pi^0$	$0.013 \pm 0.000 \pm 0.010$	estimate
$3\pi^-2\pi^+$	$0.072 \pm 0.009 \pm 0.012$	
$3\pi^-2\pi^+\pi^0$	$0.014 \pm 0.007 \pm 0.006$	
$\pi^-\pi^0\eta$	$0.180 \pm 0.040 \pm 0.020$	ALEPH [13]
$\pi^-2\pi^0\eta$	$0.015 \pm 0.004 \pm 0.003$	CLEO [27]
$\pi^-\pi^-\pi^+\eta$	$0.024 \pm 0.003 \pm 0.004$	CLEO [27]
$a_1^-(\to \pi^-\gamma)$	$0.040 \pm 0.000 \pm 0.020$	estimate
$\pi^-\omega(\to \pi^0\gamma, \pi^+\pi^-)$	$0.253 \pm 0.005 \pm 0.017$	ALEPH [13]
$\pi^-\pi^0\omega(\to \pi^0\gamma, \pi^+\pi^-)$	$0.048 \pm 0.006 \pm 0.007$	ALEPH [13] + CLEO [26]
$\pi^-2\pi^0\omega(\to \pi^0\gamma, \pi^+\pi^-)$	$0.002 \pm 0.001 \pm 0.001$	CLEO [27]
$\pi^-\pi^-\pi^+\omega(\to \pi^0\gamma, \pi^+\pi^-)$	$0.001 \pm 0.001 \pm 0.001$	CLEO [27]

Table 15: Correlation matrix of the statistical errors on the branching fractions.

	μ	h	$h\pi^0$	$h2\pi^0$	$h3\pi^0$	$h4\pi^0$	$3h$	$3h\pi^0$	$3h2\pi^0$	$3h3\pi^0$	$5h$	$5h\pi^0$
e	-0.21	-0.15	-0.25	-0.09	-0.01	0.00	-0.15	-0.10	0.03	-0.06	0.00	0.01
μ	1.00	-0.13	-0.21	-0.07	-0.06	0.00	-0.09	-0.07	0.00	-0.02	0.00	-0.04
h		1.00	-0.31	-0.02	0.01	-0.06	-0.12	-0.06	-0.02	0.01	-0.01	0.02
$h\pi^0$			1.00	-0.40	0.05	0.00	-0.11	-0.06	-0.02	0.00	-0.04	-0.04
$h2\pi^0$				1.00	-0.51	0.26	-0.09	0.01	-0.07	0.06	-0.01	0.03
$h3\pi^0$					1.00	-0.75	0.01	-0.03	0.05	-0.02	-0.01	0.01
$h4\pi^0$						1.00	-0.02	-0.02	-0.03	0.01	0.02	-0.03
$3h$							1.00	-0.33	0.08	-0.05	-0.04	0.00
$3h\pi^0$								1.00	-0.45	0.19	-0.02	-0.02
$3h2\pi^0$									1.00	-0.65	0.03	0.02
$3h3\pi^0$										1.00	-0.01	-0.04
$5h$											1.00	-0.24
$5h\pi^0$												1.00

Table 16: Correlation matrix of the systematic errors on the branching fractions.

	μ	h	$h\pi^0$	$h2\pi^0$	$h3\pi^0$	$h4\pi^0$	$3h$	$3h\pi^0$	$3h2\pi^0$	$3h3\pi^0$	$5h$	$5h\pi^0$
e	-0.17	-0.01	0.02	0.01	0.03	-0.08	-0.17	-0.22	-0.05	0.02	0.00	0.00
μ	1.00	0.05	0.09	-0.03	0.02	-0.13	-0.11	-0.24	-0.06	0.01	0.03	-0.04
h		1.00	0.36	-0.29	-0.32	-0.42	0.34	-0.40	-0.40	-0.07	0.16	-0.09
$h\pi^0$			1.00	-0.35	-0.02	-0.33	0.01	-0.54	-0.26	0.02	0.11	-0.06
$h2\pi^0$				1.00	-0.01	0.13	-0.24	0.07	0.13	0.06	-0.13	0.03
$h3\pi^0$					1.00	-0.13	-0.29	-0.02	0.15	0.09	-0.06	0.04
$h4\pi^0$						1.00	-0.14	0.34	0.27	0.00	-0.12	-0.05
$3h$							1.00	-0.03	-0.16	-0.11	0.17	-0.06
$3h\pi^0$								1.00	0.04	-0.03	-0.07	-0.01
$3h2\pi^0$									1.00	-0.14	-0.09	0.07
$3h3\pi^0$										1.00	-0.02	0.02
$5h$											1.00	-0.26
$5h\pi^0$												1.00

asymmetry [16]. It identifies and selects directly single τ hemispheres with leptons without a full selection of other *tau* decay modes. In order to normalize the selected samples, the number of produced τ pairs is derived using the $e^+e^- \rightarrow \tau^+\tau^-$ cross section measured by ALEPH [19] and the precise determination of luminosity using small-angle Bhabha scattering.

Particle identification is performed using a method quite similar to the one used in the global analysis and described in Section 4.2 but using a totally independent code. The performances of the two procedures are very close. Similarly, the treatment of photons and the separation between genuine and fake photons follows similar philosophies, but it is implemented separately.

Hemispheres with τ decay leptonic candidates are selected in two steps. In the preselection step, events with acollinear "jets" ($\cos\theta_{\mathrm{acol}} < -0.9$) are retained with a loose lepton identification at least on one side. Then, strict cuts are applied to select electron and muon hemispheres, by rejecting hadronic τ decays (electron or muon identification, veto if a π^0 is reconstructed in the same hemisphere) and non-τ background (using methods similar to those described in Section 3.3). The selection efficiencies are about 69% and 75% for electronic and muonic decays, respectively. The corresponding values for the τ decay feedthrough contaminations are 1.0% and 0.8%, and 1.5% and 0.4% for the non-τ background, respectively. The muon identification in this method allows the detection of lower muon momenta down to 1.3 GeV, compared to 2 GeV in the global method. A total of 48882 electron and 50782 muon hemispheres are thus selected. In this method the largest systematic uncertainty originates from the τ-pair normalization and is completely correlated for the electron and muon channels. The results of this specific analysis are:

$$
\begin{aligned}
B(\tau \rightarrow \nu_\tau e \overline{\nu}_e) &= (17.778 \pm 0.080 \pm 0.049)\% , & (16) \\
B(\tau \rightarrow \nu_\tau \mu \overline{\nu}_\mu) &= (17.299 \pm 0.077 \pm 0.045)\% , & (17)
\end{aligned}
$$

where the first errors are statistical and the second systematic.

Although both analyses share the same data and have both large selection efficiencies they have been carried out in a completely different and independent way, from the selection of candidates to the identification method of the final state. The comparison thus provides a valuable check.

The samples of events have been compared and the correlations found to be 0.861 for electrons and 0.896 for muons. Part of the Monte Carlo statistics is also non common. An important effect could come from the normalization of the independent method using the luminosity-derived number of produced $\tau\tau$ events, which is common to both electron and muon analyses.

The results of the independent analysis are consistent with the present values of the leptonic branching ratios. The differences found, $\Delta B_e = (0.059 \pm 0.051 \pm 0.029))\%$ and $\Delta B_\mu = (0.020 \pm 0.042 \pm 0.028)\%$, are well within the expectation of the respective noncommon errors. The second quoted errors are from the normalization of $\tau\tau$ events and are completely correlated.

Since the results are in agreement they could be combined. However, the resulting improvement is not visible for the statistical error and small for the (non-dominant) systematic uncertainty. Furthermore, it is very cumbersome to average the leptonic branching fractions alone in the framework of the global analysis where all branching ratios are derived in a consistent way. For these reasons the final results are taken from the global analysis, while the independent analysis provides a meaningful check for the leptonic channels.

14 Discussion of the results

14.1 Comparison with other experiments

As the results from other experiments are most often given without $K - \pi$ separation for charged hadrons, comparison is made summing branching ratios with charged kaons and pions. Also contributions from modes with η are included in the relevant hadronic final states. Figures 40, 41, 42, 43, 44, 45, 46, 47, 48, 49 and 50 show that the results of this analysis are in good agreement with those from other experiments. In all these cases, ALEPH achieves the best precision, except for branching ratios under 0.1%, such as $\tau \to 5h\nu$ and $\tau \to 5h\pi^0\nu$, where CLEO results are more precise because of their higher statistics.

A meaningful comparison can be performed between the exclusive fractions and the topological branching ratios B_i, where i refers to the charged particle multiplicity in the decay. Even though the latter have essentially no physics interest, their determination can constitute a valuable cross check as they depend only on selection efficiency, tracking, handling of secondary interactions and electron identification for photon conversions, and not on photon identification. The results from this analysis can be compared in this way with a dedicated analysis recently performed by DELPHI [48]. Summing up appropriately (both analyses assume a negligible contribution from hadronic multiplicities larger than five, in agreement with the 90% CL limit by CLEO [49], $B_7 < 2.4 \times 10^{-6}$), one gets

$$B_3 = (14.652 \pm 0.067 \pm 0.086)\% , \qquad (18)$$
$$B_5 = (0.093 \pm 0.009 \pm 0.012)\% , \qquad (19)$$

in good agreement with the DELPHI values, $B_3 = (14.569 \pm 0.093 \pm 0.048)\%$ and $B_5 = (0.115 \pm 0.013 \pm 0.006)\%$. The rather small systematic uncertainty in the DELPHI results reflects the fact that a sharper study of hadronic interactions can be performed when only charged particles are considered in the analysis. In addition the modes with $K_s^0 \to \pi^+\pi^-$ decays are subtracted statistically here, rather than trying to identify them on an event-by-event basis.

Figure 40: Comparison of ALEPH measurement with published precise results from other experiments for $\tau \to e\nu\bar{\nu}$. References for other experiments are ARGUS [30], CLEO [31], DELPHI [32], OPAL [33], L3 [34].

Figure 41: Comparison of ALEPH measurement with published precise results from other experiments for $\tau \to \mu\nu\bar{\nu}$. References for other experiments are ARGUS [30], CLEO [31], DELPHI [32], OPAL [35], L3 [34].

Figure 42: Comparison of ALEPH measurement with published precise results from other experiments for $\tau \rightarrow h\nu$ (sum of $\pi\nu$ and $K\nu$). References for other experiments are CLEO [31], OPAL [36].

CLEO 94
25.87±0.12±0.42

OPAL 91-95
25.89±0.17±0.29

ALEPH 91-95
25.924±0.097±0.085

average
25.916±0.116

$B(h\pi^o\nu)$ (%)

Figure 43: Comparison of ALEPH measurement with published precise results from other experiments for $\tau \to h\pi^0\nu$ (sum of $\pi\pi^0\nu$ and $K\pi^0\nu$). References for other experiments are CLEO [37], OPAL [36].

Figure 44: Comparison of ALEPH measurement with published precise results from other experiments for $\tau \to h2\pi^0\nu$ (sum of $\pi2\pi^0\nu$ and $K2\pi^0\nu$). References for other experiments are CLEO [38].

Figure 45: Comparison of ALEPH measurement with published precise results from other experiments for $\tau \to h(3,4)\pi^0\nu$ (sum of $\pi(3,4)\pi^0\nu$ and $K(3,4)\pi^0\nu$). References for other experiments are CLEO [38].

Figure 46: Comparison of ALEPH measurement with published precise results from other experiments for $\tau \rightarrow 3h\nu$ (sum of $3\pi\nu$, $K2\pi\nu$ and $2K\pi\nu$). References for other experiments are CLEO [39], OPAL [40].

Figure 47: Comparison of ALEPH measurement with published precise results from other experiments for $\tau \rightarrow 3h\pi^0\nu$ (sum of $3\pi\pi^0\nu$, $K2\pi\nu$ and $2K\pi\nu$). References for other experiments are CLEO [39].
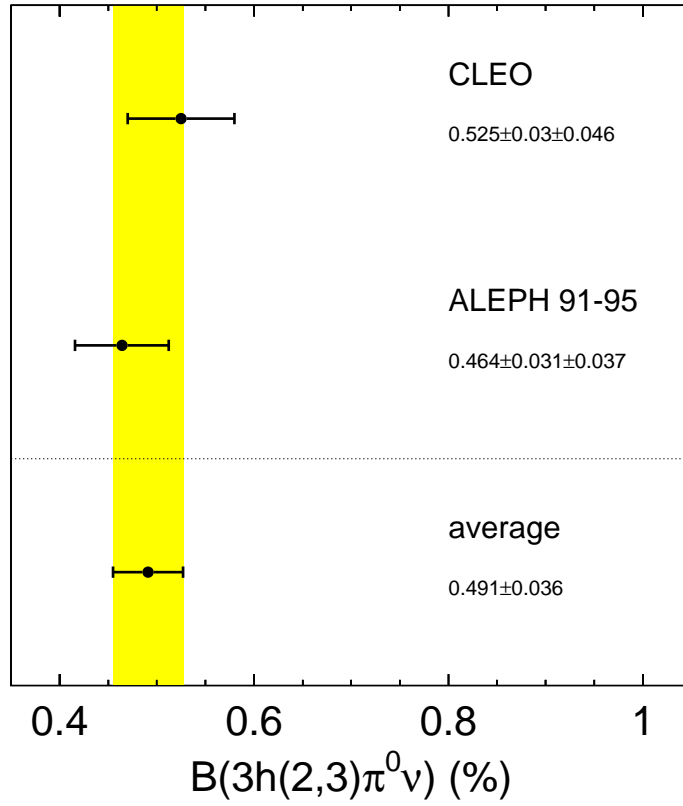
Figure 48: Comparison of ALEPH measurement with published precise results from other experiments for $\tau \to 3h(2,3)\pi^0\nu$ (sum of $3\pi(2,3)\pi^0\nu$, $K2\pi(2,3)\pi^0\nu$ and $2K\pi(2,3)\pi^0\nu$). References for other experiments are CLEO [41].
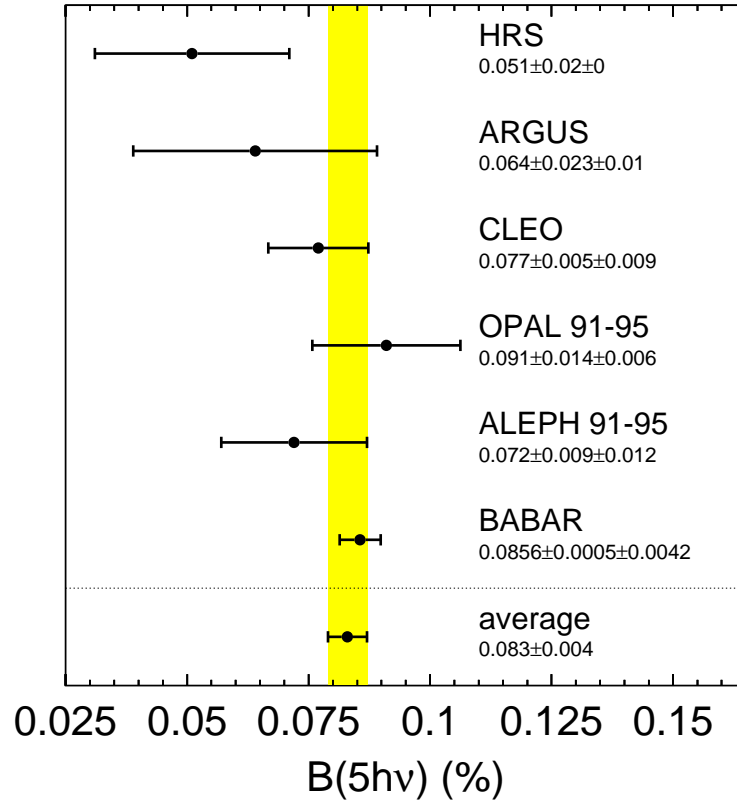
Figure 49: Comparison of ALEPH measurement with published precise results from other experiments for $\tau \to 5h\nu$. References for other experiments are HRS [42], ARGUS [43], CLEO [44], OPAL [45], BABAR [46].

CLEO

0.017±0.002±0.002

OPAL 91-95

0.027±0.018±0.009
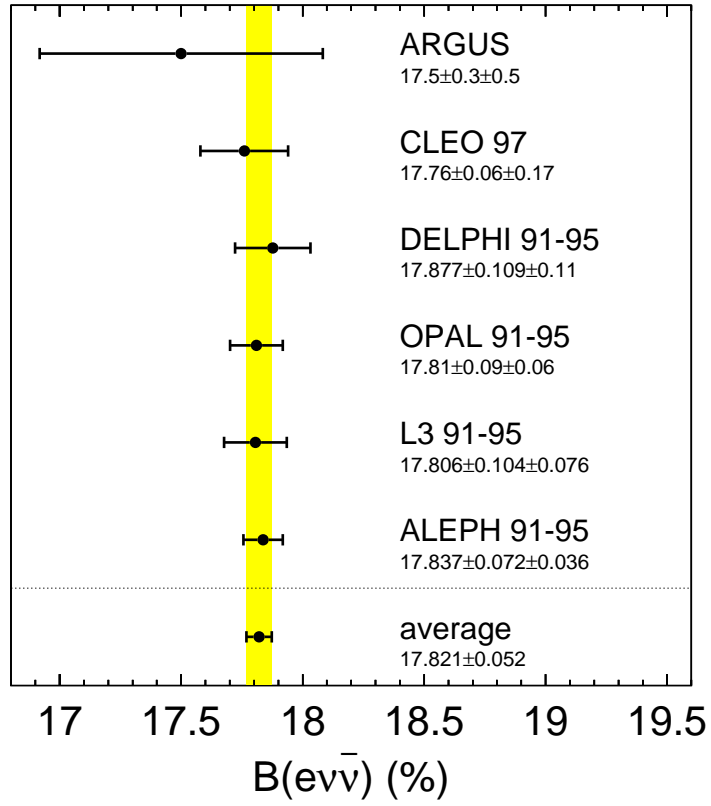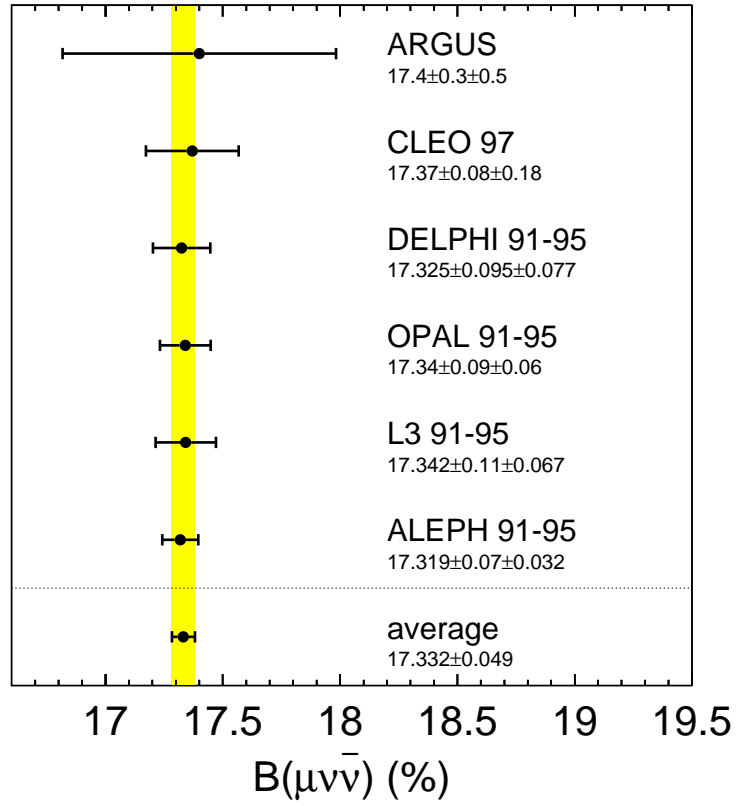
ALEPH 91-95

0.014±0.007±0.006

average

0.017±0.003

B(5hπ⁰ν) (%)
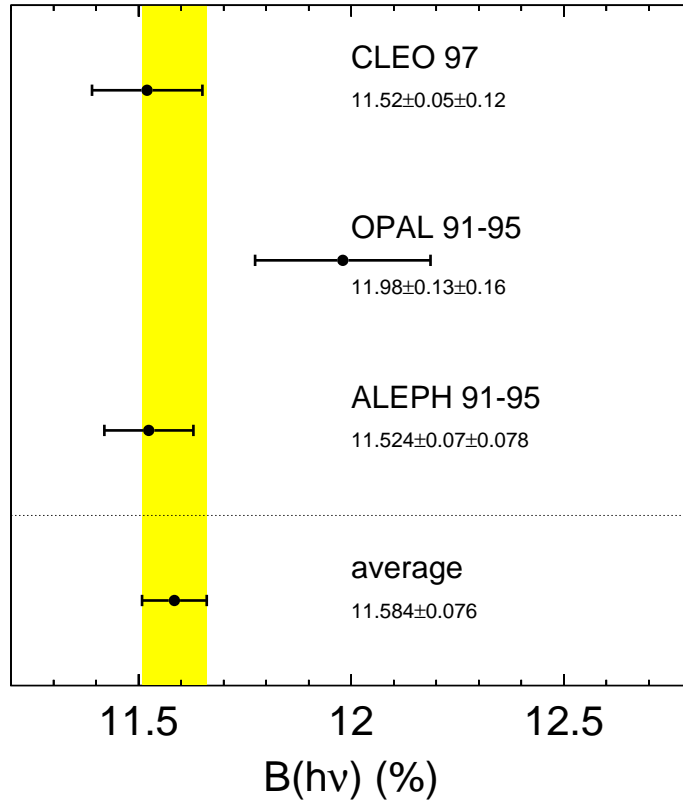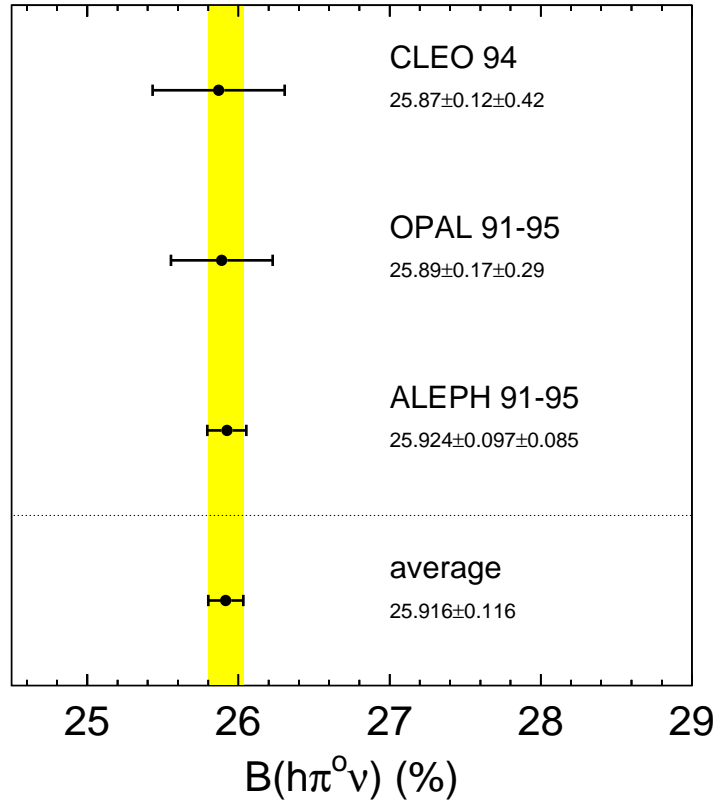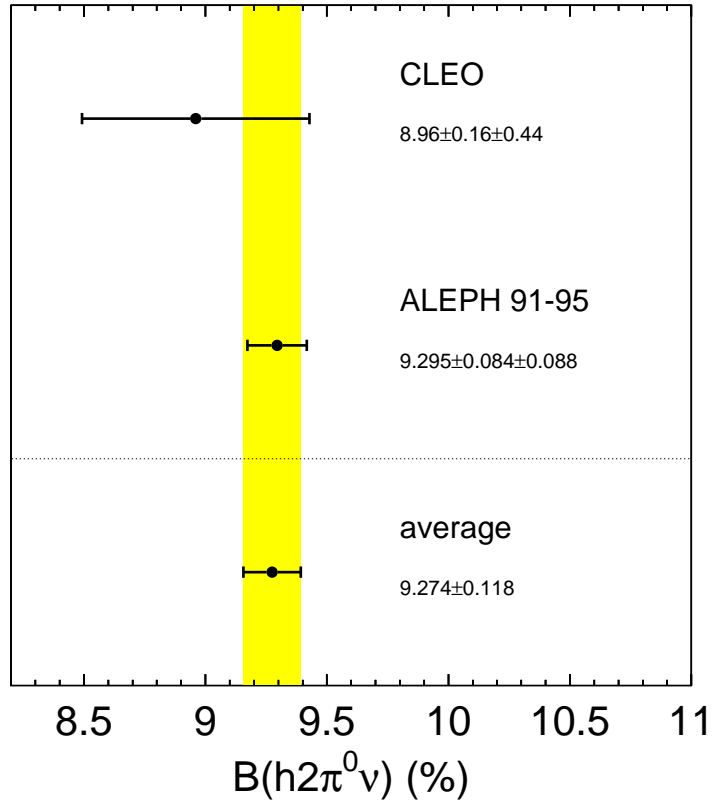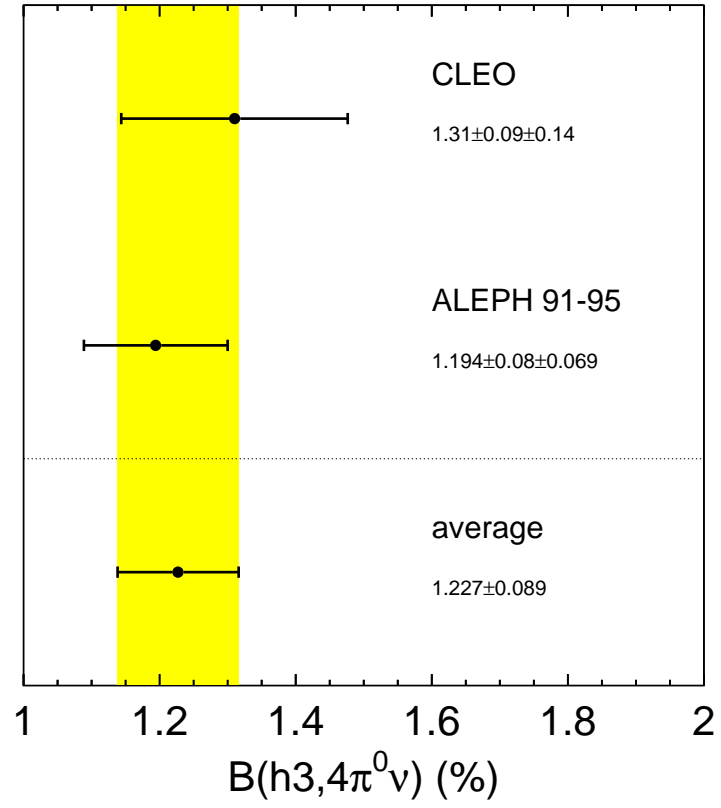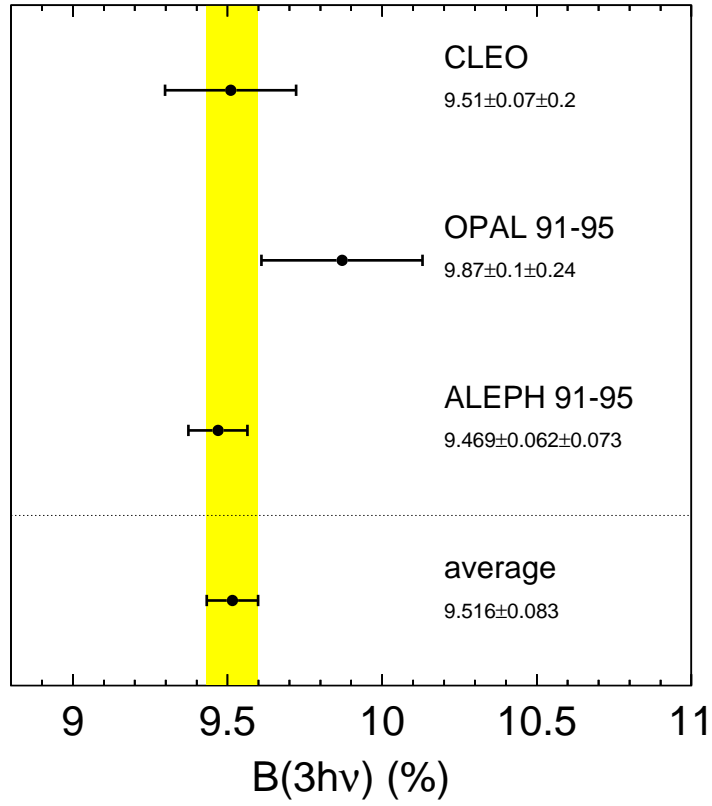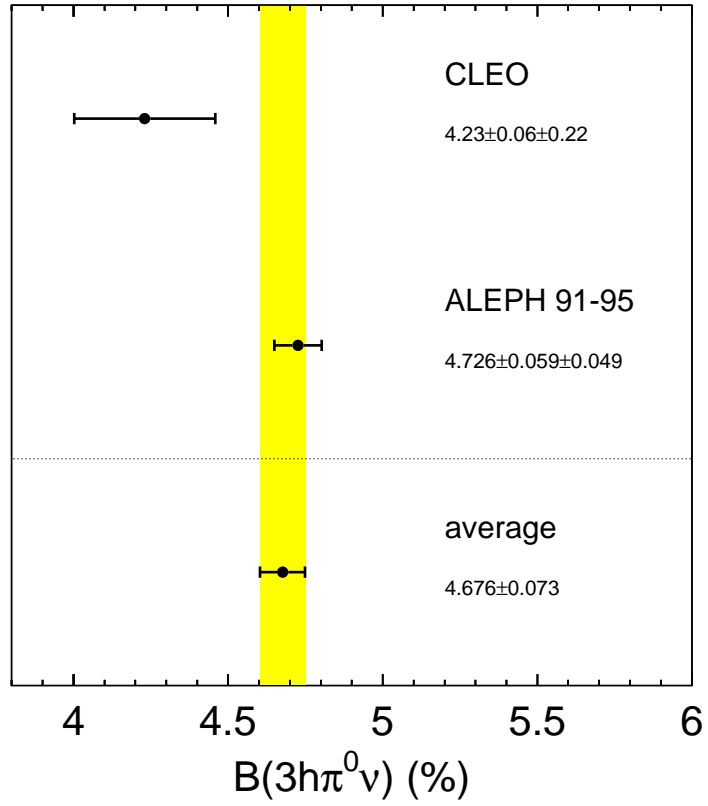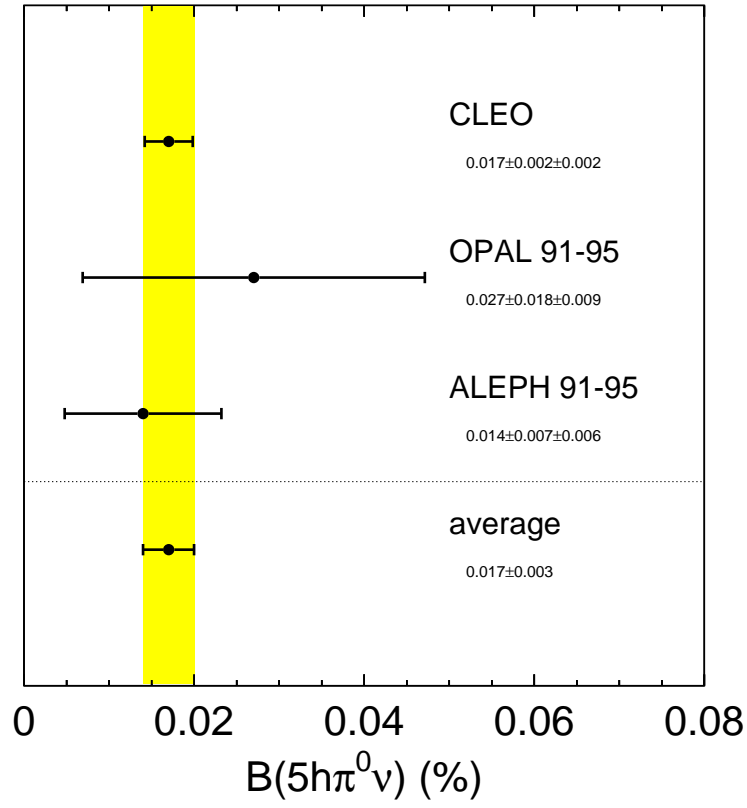
Figure 50: Comparison of ALEPH measurement with published precise results from other experiments for $\tau \to 5h\pi^0\nu$. References for other experiments are CLEO [47], OPAL [45].

14.2 Universality in the leptonic charged current

14.2.1 $\mu - e$ universality from the leptonic branching ratios

In the standard V-A theory with leptonic coupling g_l at the $Wl\overline{\nu}_l$ vertex, the τ leptonic partial width can be computed, including radiative corrections [50] and safely neglecting neutrino masses:

$$\Gamma(\tau \to \nu_\tau l \overline{\nu}_l(\gamma)) = \frac{G_\tau G_l m_\tau^5}{192\pi^3} f\left(\frac{m_l^2}{m_\tau^2}\right) \delta_W^\tau \delta_\gamma^\tau \ , \tag{20}$$

where

$$\begin{aligned}
G_l &= \frac{g_l^2}{4\sqrt{2}M_W^2} \ , \\
\delta_W^\tau &= 1 + \frac{3}{5}\frac{m_\tau^2}{M_W^2} \ , \\
\delta_\gamma^\tau &= 1 + \frac{\alpha(m_\tau)}{2\pi}\left(\frac{25}{4} - \pi^2\right) \ , \\
f(x) &= 1 - 8x + 8x^3 - x^4 - 12x^2 \ln x \ .
\end{aligned} \tag{21}$$

Numerically, the W propagator correction and the radiative corrections are small: $\delta_W^\tau = 1 + 2.9 \times 10^{-4}$ and $\delta_\gamma^\tau = 1 - 43.2 \times 10^{-4}$.

Taking the ratio of the two leptonic branching fractions, a direct test of $\mu - e$ universality is obtained. The measured ratio

$$\frac{B_\mu}{B_e} = 0.9709 \pm 0.0060 \pm 0.0029 \tag{22}$$

agrees with the expectation of 0.97257 when universality holds. Alternatively the measurements yield the ratio of couplings

$$\frac{g_\mu}{g_e} = 0.9991 \pm 0.0033 \tag{23}$$

which is consistent with unity.

This result is in agreement with the best test of $\mu - e$ universality of the W couplings obtained in the comparison of the rates for $\pi \to \mu\overline{\nu}_\mu$ and $\pi \to e\overline{\nu}_e$ decays, where the results of the two most accurate experiments [51, 52] can be averaged to yield $\frac{g_\mu}{g_e} = 1.0012 \pm 0.0016$. The results have comparable precision, but it should be pointed out that they are in fact complementary. The τ result given here probes the coupling to a transverse W (helicity ± 1) while the π decays measure the coupling to a longitudinal W (helicity 0). It is indeed conceivable that either approach could be sensitive to different nonstandard corrections to universality.

Since B_e and B_μ are consistent with $\mu - e$ universality their values can be combined, taking common errors into account, into a consistent leptonic branching ratio for a massless lepton (the electron, since $f(\frac{m_e^2}{m_\tau^2}) = 1$ within 10^{-6})

$$B_l^{(m_l=0)} = (17.822 \pm 0.044 \pm 0.022)\% \ , \tag{24}$$

where the first error is statistical and the second systematic.

14.2.2 Tests of $\tau - \mu$ and $\tau - e$ universality

Comparing the rates for $\Gamma(\tau \to \nu_\tau e \overline{\nu}_e(\gamma))$, $\Gamma(\tau \to \nu_\tau \mu \overline{\nu}_\mu(\gamma))$ and $\Gamma(\mu \to \nu_\mu e \overline{\nu}_e(\gamma))$ provides direct tests of the universality of $\tau - \mu - e$ couplings. Taking the relevant ratios with calculated radiative corrections, one obtains

$$\left(\frac{g_\tau}{g_\mu}\right)^2 = \frac{\tau_\mu}{\tau_\tau} \left(\frac{m_\mu}{m_\tau}\right)^5 B_e \frac{f(\frac{m_e^2}{m_\mu^2})}{f(\frac{m_e^2}{m_\tau^2})} \Delta_W \Delta_\gamma \ , \tag{25}$$

$$\left(\frac{g_\tau}{g_e}\right)^2 = \frac{\tau_\mu}{\tau_\tau} \left(\frac{m_\mu}{m_\tau}\right)^5 B_\mu \frac{f(\frac{m_e^2}{m_\mu^2})}{f(\frac{m_\mu^2}{m_\tau^2})} \Delta_W \Delta_\gamma \ , \tag{26}$$

where $f(\frac{m_e^2}{m_\mu^2}) = 0.9998$, $\Delta_W = \frac{\delta_W^\mu}{\delta_W^\tau} = 1 - 2.9 \times 10^{-4}$, $\Delta_\gamma = \frac{\delta_\gamma^\mu}{\delta_\gamma^\tau} = 1 + 8.5 \times 10^{-5}$, and τ_l is the lepton l lifetime.

From the present measurements of B_e, B_μ, the τ mass [25], $m_\tau = (1777.03^{+0.30}_{-0.26})$ MeV (dominated by the BES result [66]), the τ lifetime [25], $\tau_\tau = (290.6 \pm 1.1)$ fs and the other quantities from Ref. [25], universality can be tested:

$$\frac{g_\tau}{g_\mu} = 1.0009 \pm 0.0023(B_e) \pm 0.0019(\tau_\tau) \pm 0.0004(m_\tau) \ , \tag{27}$$

$$\frac{g_\tau}{g_e} = 1.0001 \pm 0.0022(B_\mu) \pm 0.0019(\tau_\tau) \pm 0.0004(m_\tau) \ . \tag{28}$$

14.2.3 $\tau - \mu$ universality from the pionic branching ratio

The measurement of B_π also permits an independent test of $\tau - \mu$ universality through the relation

$$\left(\frac{g_\tau}{g_\mu}\right)^2 = \frac{B_\pi}{B_{\pi \to \mu \overline{\nu}_\mu}} \frac{\tau_\pi}{\tau_\tau} \frac{2 m_\pi m_\mu^2}{m_\tau^3} \left(\frac{1 - \frac{m_\mu^2}{m_\pi^2}}{1 - \frac{m_\pi^2}{m_\tau^2}}\right)^2 \frac{1}{\delta_{\tau/\pi}} \ , \tag{29}$$

where the radiative correction [53] amounts to $\delta_{\tau/\pi} = 1.0016 \pm 0.0014$. Using the world-averaged values for the τ and π (τ_π) lifetimes, and the branching ratio for the decay $\pi \to \mu\nu$ [25], the present result for B_π, one obtains

$$\frac{g_\tau}{g_\mu} = 0.9962 \pm 0.0048(B_\pi) \pm 0.0019(\tau_\tau) \pm 0.0002(m_\tau) \pm 0.0007(rad) \ , \tag{30}$$

comparing the measured value, $B_\pi = (10.828 \pm 0.105)\%$, to the expected one assuming universality, $(10.910 \pm 0.042)\%$.

The two determinations of $\frac{g_\tau}{g_\mu}$ obtained from B_e and B_π are consistent with each other and can be combined to yield

$$\frac{g_\tau}{g_\mu} = 1.0000 \pm 0.0021(B_e, B_\pi) \pm 0.0019(\tau_\tau) \pm 0.0004(m_\tau) \ . \tag{31}$$
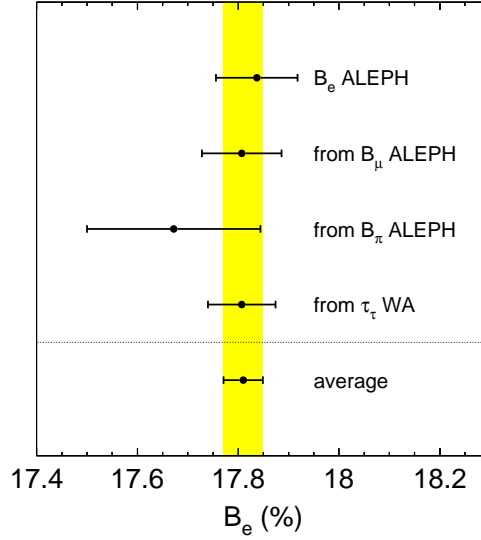
Figure 51: The measured value for B_e compared to predictions from other measurements assuming leptonic universality. The vertical band gives the average of all determinations.

Universality of the τ and μ charged-current couplings holds at the 0.29% level with about equal contributions from the present determination of B_e and B_π, and the world-averaged value for the τ lifetime.

The consistency of the present branching ratio measurements with leptonic universality is displayed in Fig. 51 where the result for B_e is compared to computed values of B_e using as input B_μ (assuming $e - \mu$ universality), τ_τ and τ_μ ($\mu - \tau$ universality), and B_π and τ_π ($\mu - \tau$ universality). All values are consistent and yield the average

$$B_e^{\text{universality}} = (17.810 \pm 0.039)\% . \tag{32}$$

14.3 The $\pi\pi^0$ branching ratio in the context of a_μ^{had}

The $\pi\pi^0$ final state is dominated by the ρ resonance as demonstrated in Fig. 39. Its mass distribution —or better, the corresponding spectral function, see Section 15— is a basic ingredient of vacuum polarization calculations, such as used for computing the hadronic contribution to the anomalous magnetic moment of the muon a_μ^{had}. In this case the ρ contribution is dominant (71%) and therefore controls the final precision of the result. It was proposed in Ref. [54] to use the spectral functions obtained from the measurement of hadronic τ decays in order to improve the precision of the prediction for a_μ^{had}. The calculation was later improved with the help of QCD constraints for energies above the τ mass [55] and even below [56].

The normalization of the spectral function is provided by the branching fraction $B_{\pi\pi^0}$. The present world average is completely dominated by the published ALEPH result [3].
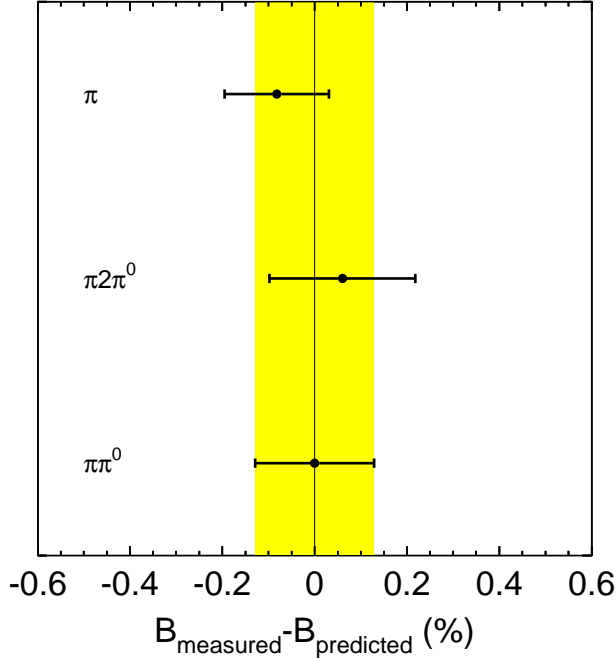
Figure 52: The differences between the measured values for B_π and $B_{\pi 2\pi^0}$ and their respective predictions from leptonic universality and isospin symmetry with π-mass breaking, compared to the precision on $B_{\pi\pi^0}$.

The new result given here is larger by 0.68%, thus one can expect a slightly larger contribution to a_μ^{had}.

A new evaluation [57] of a_μ^{had} was available, using the preliminary spectral functions from the present analysis, the published CLEO results [58] and new results from e^+e^- annihilation from CMD-2 [59]. Revision of the CMD-2 results [60] prompted a re-evaluation [61], which revealed a disagreement between the τ and e^+e^- spectral functions (see Section 15). Whereas the τ estimate leads to a prediction of the muon magnetic moment in agreement with the latest most precise measurement from the BNL experiment E-821 [62], the predicted value using only e^+e^- data lies 2.4 standard deviations below the measurement. In view of this situation, it is important to check all the ingredients, in particular the determination of the branching ratio $B_{\pi\pi^0}$. As most of the systematic uncertainty in $B_{\pi\pi^0}$ comes from γ/π^0 reconstruction, it is helpful to cross check the results in the "adjacent" hadronic modes, i.e. the π and $\pi 2\pi^0$ channels. This is possible if universality in the weak charged current is assumed, leading to an absolute prediction of B_π using as input the τ and π lifetimes (Section 14.2.3, Eq. (29)), and by computing $B_{\pi 2\pi^0}$ assuming isospin symmetry from the measurement of $B_{3\pi}$ which is essentially uncorrelated with $B_{\pi\pi^0}$ (Section 14.4). The comparison, shown in Fig. 52, does not point to a systematic bias in the determination of $B_{\pi\pi^0}$ within the quoted uncertainty.

14.4 a_1 decays to 3π and $\pi 2\pi^0$

With the level of precision reached it is interesting to compare the rates in the 3π and $\pi 2\pi^0$ channels which are dominated by the a_1 resonance. The dominant $\rho\pi$ intermediate state leads to equal rates, but a small isospin-breaking effect is expected from different charged and neutral π masses, slightly favouring the $\pi 2\pi^0$ channel, as discussed below.

A recent CLEO partial-wave analysis of the $\pi 2\pi^0$ final state [63] has shown that the situation is in fact much more complicated with many intermediate states, in particular involving isoscalars, amounting to about 20% of the total rate and producing strong interference effects. A good description of the a_1 decays was achieved in the CLEO study, which can be applied to the 3π final state, predicting [63] a ratio of the rates $3\pi/\pi 2\pi^0$ equal to 0.985. This value, which includes known isospin-breaking from the pion masses, turns out to be in good agreement with the measured value from this analysis which shows the expected trend

$$\frac{B_{3\pi}}{B_{\pi 2\pi^0}} = 0.979 \pm 0.018 . \tag{33}$$

14.5 Separation of vector and axial-vector contributions

14.5.1 Strange and nonstrange contributions

From the complete analysis of the τ branching ratios presented in this paper, it is possible to determine the nonstrange vector (V) and axial-vector (A) contributions to the total τ hadronic width, conveniently expressed in terms of their ratios to the leptonic width, called $R_{\tau,V}$ and $R_{\tau,A}$, respectively. The determination of the strange counterpart $R_{\tau,S}$ is already published [9].

The ratio R_τ for the total hadronic width is calculated from the leptonic branching ratios alone, and eventually from the electronic branching ratio alone,

$$\begin{aligned} R_\tau &= \frac{1 - B_e - B_\mu}{B_e} = \frac{1}{B_e} - 1.9726 \\ &= 3.642 \pm 0.012 . \end{aligned} \tag{34}$$

taking for $B(\tau^- \to e^- \bar\nu_e \nu_\tau)$ the value obtained in Section 14.2 assuming universality in the leptonic weak current. All R values given below are rescaled so that the sum of the hadronic and the leptonic branching ratios, the latter computed using the "universal" value given in Eq. 32), add up to unity. The deviations introduced in this way are extremely small, less than one tenth of the experimental error, but this procedure guarantees the consistency between all values. Using the ALEPH measurement of the strange branching ratios [9], supplemented by the small contribution from the $K^{*-}\eta$ channel measured by CLEO [64],

$$\begin{aligned} B_S &= (2.85 \pm 0.11) \% , \\ R_{\tau,S} &= 0.1603 \pm 0.0064 , \end{aligned} \tag{35}$$

the following result is obtained for the nonstrange component

$$B_{V+A} = (62.01 \pm 0.14) \% ,$$
$$R_{\tau,V+A} = 3.482 \pm 0.014 . \tag{36}$$

Separation of V and A components in hadronic final states with only pions is straightforward. Isospin invariance relates the spin-parity of such systems to their number of pions: G-parity $=1$ (even number) corresponds to vector states, while $G = -1$ (odd number) tags axial-vector states. This property places a strong requirement on the efficiency of π^0 reconstruction, a constraint that was emphasized in this analysis.

14.5.2   V and A separation in modes with a $K\overline{K}$ pair

Modes with a $K\overline{K}$ pair are not in general eigenstates of G-parity and contribute to both V and A channels. While the decay to K^-K^0 is pure vector, the situation is a priori not clear in the $K\overline{K}\pi$ channel, observed in three charged modes: $K^-K^+\pi^-$, $K^-K^0\pi^0$ and $K^0\overline{K}^0\pi^-$. Three sources of information exist on the possible V/A content in this decay mode:

(i) in the ALEPH analysis of τ decay modes with kaons [9], an estimate of the vector contribution was obtained using the available e^+e^- annihilation data in the $K\overline{K}\pi$ channel, extracted in the $I = 1$ state. In fact, this contribution was found to be very small, yielding a branching ratio consistent with zero, $B_{\mathrm{CVC}}(\tau \to \nu_\tau[K\overline{K}\pi]_V) = (0.26 \pm 0.39) \times 10^{-3}$, corresponding to an axial fraction, $f_A(\mathrm{CVC}) = 0.94^{+0.06}_{-0.08}$.

(ii) The CVC/ALEPH result is corroborated by a partial-wave and lineshape analysis of the a_1 resonance from τ decays in the $\nu_\tau\pi^-2\pi^0$ mode by CLEO [63]. The observation through unitarity of the opening of the K^*K decay mode of the a_1 is claimed and a branching ratio $B(a_1 \to K^*K) = (3.3 \pm 0.5)\%$ obtained. Knowing the decay rate of $\tau \to \nu_\tau a_1$, it is easy to see that such a result completely saturates, and even exceeds, the total rate for the $K\overline{K}\pi$ channel. The corresponding axial fraction turns out to be $f_A(\mathrm{CLEO}\ 3\pi) = 1.30 \pm 0.24$.

(iii) A new piece of information, also contributed by CLEO, but conflicting with the two previous results, was recently published [65]. It is based on a partial-wave analysis in the $K^-K^+\pi^-$ channel using two-body resonance production and including many possibly contributing channels. A much smaller axial contribution is obtained, $f_A(\mathrm{CLEO}\ KK\pi) = 0.56 \pm 0.10$.

The three determinations are displayed in Fig. 53. Since they are not consistent, a conservative value of $f_A = 0.75 \pm 0.25$ is assumed. It encompasses the range allowed by the previous results and still represents some progress over our former analyses [11, 12] where a value of 0.5 ± 0.5 was used. For the decays into $K\overline{K}\pi\pi$ no information is available in this respect and the same conservative fraction of 0.5 ± 0.5 is assumed.

All the present measurements and previous ones for modes with a $K\overline{K}$ pair are summarized in a complete list of determined branching ratios for nonstrange hadronic final states up to six hadrons, and four with kaons. The results are given in Table 17.
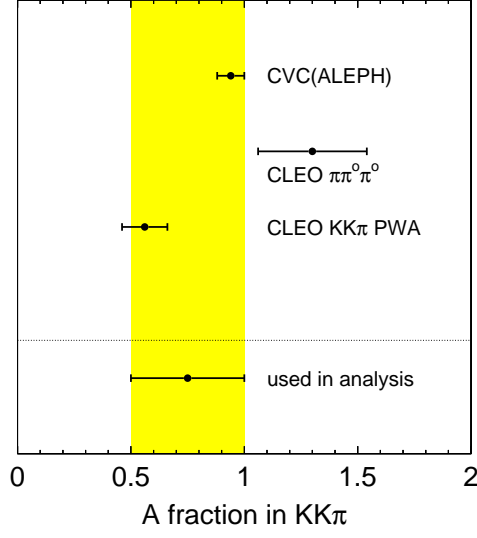
Figure 53: The axial-vector fraction f_A of the hadrons in the $\tau \to \nu_\tau K\overline{K}\pi$ decay mode from three independent determinations: ALEPH [9] using CVC and e^+e^- data, CLEO [63] with a partial-wave analysis of $a_1 \to \pi^- 2\pi^0$ decays, and CLEO [65] with a direct partial-wave analysis of the $\tau \to \nu_\tau K^+ K^- \pi^-$ decays. The shaded band corresponds to the conservative range used in this analysis.

14.5.3 Total V and A contributions in the non-strange sector

The total nonstrange vector and axial-vector contributions obtained in this analysis are:

$$
\begin{align}
B_V &= (31.82 \pm 0.18 \pm 0.12) \ \% \ , \tag{37} \\
R_{\tau,V} &= 1.787 \pm 0.011 \pm 0.007 \ , \tag{38} \\
B_A &= (30.19 \pm 0.18 \pm 0.12) \ \% \ , \tag{39} \\
R_{\tau,A} &= 1.695 \pm 0.011 \pm 0.007 \ , \tag{40}
\end{align}
$$

where the second errors reflect the uncertainties in the V/A separation in the channels with $K\overline{K}$ pairs. Accounting for the correlations between the respective uncertainties, one obtains the difference between the vector and axial-vector components, which is physically related to the amount of nonperturbative contributions in the nonstrange hadronic τ decay width (see Section 17):

$$
\begin{align}
B_{V-A} &= (1.63 \pm 0.34 \pm 0.24) \ \% \ , \tag{41} \\
R_{\tau,V-A} &= 0.092 \pm 0.018 \pm 0.014 \ , \tag{42}
\end{align}
$$

where again the second error has the same meaning as in Eqs. (37) and (39). The ratio

$$
\frac{R_{\tau,V-A}}{R_{\tau,V+A}} = 0.026 \pm 0.007 \tag{43}
$$

is a measure of the relative importance of nonperturbative contributions.

These values yield the normalization of the corresponding spectral functions, which will be determined later for the QCD analysis of hadronic τ decays and vacuum polarization calculations. Compared to the previous analysis, the vector/axial-vector separation is significantly improved and will result in better determined nonperturbative contributions.

14.6 Summary of all measured branching ratios

A summary list of all τ branching ratios measured by ALEPH using the full LEP-1 statistics is given in Table 17.

15 Determination of hadronic spectral functions

15.1 Spectral functions

The spectral function v_1 (a_1, a_0), where the subscript refers to the spin J of the hadronic system, is here defined for a nonstrange vector (axial-vector) hadronic τ decay channel $V^- \nu_\tau$ $(A^- \nu_\tau)$. The spectral function is obtained by dividing the normalized invariant mass-squared distribution $(1/N_{V/A})(dN_{V/A}/ds)$ for a given hadronic mass $\sqrt{s}$ by the appropriate kinematic factor

$$
v_1(s) \equiv \frac{m_\tau^2}{6\,|V_{ud}|^2\,S_{EW}} \frac{B(\tau^- \to V^- \nu_\tau)}{B(\tau^- \to e^- \bar{\nu}_e \nu_\tau)}
$$

$$
\times \frac{dN_V}{N_V\,ds} \left[\left(1 - \frac{s}{m_\tau^2}\right)^2 \left(1 + \frac{2s}{m_\tau^2}\right) \right]^{-1}, \tag{44}
$$

$$
a_1(s) \equiv \frac{m_\tau^2}{6\,|V_{ud}|^2\,S_{EW}} \frac{B(\tau^- \to A^- \nu_\tau)}{B(\tau^- \to e^- \bar{\nu}_e \nu_\tau)}
$$

$$
\times \frac{dN_A}{N_A\,ds} \left[\left(1 - \frac{s}{m_\tau^2}\right)^2 \left(1 + \frac{2s}{m_\tau^2}\right) \right]^{-1}, \tag{45}
$$

$$
a_0(s) \equiv \frac{m_\tau^2}{6\,|V_{ud}|^2\,S_{EW}} \frac{B(\tau^- \to \pi^- \nu_\tau)}{B(\tau^- \to e^- \bar{\nu}_e \nu_\tau)} \frac{dN_A}{N_A\,ds} \left(1 - \frac{s}{m_\tau^2}\right)^{-2}, \tag{46}
$$

where $|V_{ud}| = 0.9746 \pm 0.0006$ [61] denotes the CKM weak mixing matrix element and $S_{EW} = 1.0198 \pm 0.0006$ accounts for electroweak radiative corrections [50], as discussed in Section 16.1. Due to the conserved vector current, there is no $J = 0$ contribution to the vector spectral function, while the only contribution to a_0 is assumed to be from the pion pole. It is connected via PCAC to the pion decay constant, f_π through $a_{0,\pi}(s) = 4\pi^2 f_\pi^2 \delta(s - m_\pi^2)$. The spectral functions are normalized by the ratio of the vector/axial-vector branching fraction $B(\tau^- \to V^-/A^- \nu_\tau)$ to the branching fraction of the massless leptonic, i.e., electron, channel. For the latter, the value obtained in Section 14.2 using universality is used, i.e. $B(\tau^- \to e^- \bar{\nu}_e \nu_\tau) = (17.810 \pm 0.039)\%$.

Table 17: A summary list of ALEPH branching ratios (%). Statistical and systematical uncertainties have been combined in quadrature. The labels V, A and S refer to the nonstrange vector and axial-vector, and strange components, respectively. CLEO results on channels with small branching fractions have been used as indicated.

mode	B [%]		
e	17.837 ± 0.080		
μ	17.319 ± 0.077		
π^-	10.828 ± 0.105	A	
$\pi^-\pi^0$	25.471 ± 0.129	V	
$\pi^-2\pi^0$	9.239 ± 0.124	A	
$\pi^-3\pi^0$	0.977 ± 0.090	V	
$\pi^-4\pi^0$	0.112 ± 0.051	A	
$\pi^-\pi^-\pi^+$	9.041 ± 0.097	A	
$\pi^-\pi^-\pi^+\pi^0$	4.590 ± 0.086	V	
$\pi^-\pi^-\pi^+2\pi^0$	0.392 ± 0.046	A	
$\pi^-\pi^-\pi^+3\pi^0$	0.013 ± 0.010	V	estimate
$3\pi^-2\pi^+$	0.072 ± 0.015	A	
$3\pi^-2\pi^+\pi^0$	0.014 ± 0.009	V	
$\pi^-\pi^0\eta$	0.180 ± 0.045	V	
$(3\pi)^-\eta$	0.039 ± 0.007	A	CLEO [27]
$a_1^-(\to \pi^-\gamma)$	0.040 ± 0.020	A	estimate
$\pi^-\omega(\to \pi^0\gamma, \pi^+\pi^-)$	0.253 ± 0.018	V	
$\pi^-\pi^0\omega(\to \pi^0\gamma, \pi^+\pi^-)$	0.048 ± 0.009	A	+ CLEO [26]
$(3\pi)^-\omega(\to \pi^0\gamma, \pi^+\pi^-)$	0.003 ± 0.003	V	CLEO [27]
K^-K^0	0.163 ± 0.027	V	
$K^-\pi^0K^0$	0.145 ± 0.027	$(75 \pm 25)\%$ A	
$\pi^-K^0\overline{K^0}$	0.153 ± 0.035	$(75 \pm 25)\%$ A	
$K^-K^+\pi^-$	0.163 ± 0.027	$(75 \pm 25)\%$ A	
$(K\overline{K}\pi\pi)^-$	0.050 ± 0.020	$(50 \pm 50)\%$ A	
K^-	0.696 ± 0.029	S	
$K^-\pi^0$	0.444 ± 0.035	S	
$\overline{K^0}\pi^-$	0.917 ± 0.052	S	
$K^-2\pi^0$	0.056 ± 0.025	S	
$K^-\pi^+\pi^-$	0.214 ± 0.047	S	
$\overline{K^0}\pi^-\pi^0$	0.327 ± 0.051	S	
$(K3\pi)^-$	0.076 ± 0.044	S	
$K^-\eta$	0.029 ± 0.014	S	
$K^-\omega$	0.067 ± 0.021	S	
$K^{*-}\eta$	0.029 ± 0.009	S	CLEO [64]

Using unitarity and analyticity, the spectral functions are connected to the imaginary part of the two-point correlation (or hadronic vacuum polarization) functions [67, 68] $\Pi_{ij,U}^{\mu\nu}(q) \equiv i \int d^4x\, e^{iqx} \langle 0|T(U_{ij}^\mu(x)U_{ij}^\nu(0)^\dagger)|0\rangle = (-g^{\mu\nu}q^2 + q^\mu q^\nu)\,\Pi_{ij,U}^{(1)}(q^2) + q^\mu q^\nu\,\Pi_{ij,U}^{(0)}(q^2)$ of vector ($U_{ij}^\mu \equiv V_{ij}^\mu = \bar{q}_j\gamma^\mu q_i$) or axial-vector ($U_{ij}^\mu \equiv A_{ij}^\mu = \bar{q}_j\gamma^\mu\gamma_5 q_i$) colour-singlet quark currents in corresponding quantum states and for time-like momenta-squared $q^2 > 0$. Lorentz decomposition is used to separate the correlation function into its $J = 1$ and $J = 0$ parts. Thus, using the definition (44), one identifies for non-strange quark currents

$$
\begin{aligned}
\operatorname{Im}\Pi_{\bar{u}d,V}^{(1)}(s) &= \frac{1}{2\pi}v_1(s)\ , \\
\operatorname{Im}\Pi_{\bar{u}d,A}^{(1)}(s) &= \frac{1}{2\pi}a_1(s)\ , \\
\operatorname{Im}\Pi_{\bar{u}d,A}^{(0)}(s) &= \frac{1}{2\pi}a_0(s)\ ,
\end{aligned}
\tag{47}
$$

which provide the basis for comparing short-distance theory with data.

15.2   The unfolding procedure

The measurement of the τ spectral functions defined in Eq. (46) requires the determination of the invariant mass-squared distributions, obtained from the experimental distributions after unfolding from the effects of measurement distortion. The unfolding procedure used in this analysis follows a method published in Ref. [69], which has been extensively used in previous publications [11, 12]. It is based on the regularized inversion of the detector response matrix, obtained from the Monte Carlo simulation, using the Singular Value Decomposition (SVD) technique. The regularization function applied minimizes the average curvature of the distribution. The optimal choice of the regularization strength is found by means of the Monte Carlo simulation where the true distribution is known.

In order to measure exclusive spectral functions, individual unfolding procedures with specific detector response matrices and regularization parameters are applied for each τ decay channel X considered. An iterative procedure is applied to correct the Monte Carlo spectral functions used to subtract the feed across between the modes. Each spectral function is determined in 140 mass-squared bins of equal width ($0.025\ \mathrm{GeV}^2$).

15.3   Specific systematic studies

All systematic uncertainties concerning the decay classification are contained in the covariance matrix of the branching ratios obtained in Section 10. Therefore only the systematic effects affecting the shape of the mass-squared distributions, and not its normalization, need to be examined here.

The general procedure is the same as for the branching ratio analysis. All effects affecting the decay classification and the calculation of the hadronic invariant mass are considered in turn. Comparisons of data and Monte Carlo distributions are made and the corresponding biases are corrected for, as discussed in Section 10, while the uncertainty

in the correction is taken as input for the calculation of the systematic uncertainty. In the case of the spectral functions, the whole analysis including the unfolding procedure is repeated, for each systematic effect. This generates new mass distributions under the systematic change which are compared bin-by-bin to the nominal ones, hence providing the full 140×140 covariance matrix of the spectral function for the studied effect. In this process it was found necessary to smooth the mass distributions, before and after applying the systematic effect, in order to construct stable covariance matrices.

Following the systematic studies for the determination of the branching ratios, extensive studies are performed to determine the uncertainties at the level of the spectral functions. They include the effects from the photon and π^0 energy calibration and resolution, the photon detection efficiency (especially in the threshold region above 350 MeV), the shapes of the identification probability distribution, the estimate of the number of fake photons, the proximity in the calorimeter of other photon showers and of energy deposition by charged particles, and the separation between radiative and π^0 decay photons for residual single photons. The photon and π^0 reconstruction constitutes the main part of the uncertainty for the determination of spectral functions.

Similarly, the effects of momentum calibration and resolution uncertainties in the reconstruction of charged tracks are checked, accompanied by tests of the reconstruction efficiency of highly collimated multi-prong events, and the simulation of secondary nuclear interactions.

In addition, systematic errors introduced by the unfolding procedure are tested by comparing known, true distributions to their corresponding unfolded ones.

Finally, systematic errors due to the limited Monte Carlo statistics and to uncertainties in the branching ratios are added.

15.4   Spectral functions for nonstrange exclusive modes

15.4.1   The results

Before unfolding the mass distributions, the τ and non-τ backgrounds are subtracted. In the case of τ feedthrough the Monte Carlo distributions normalized to the measured branching fractions are used. Since the spectral functions are measured for nonstrange exclusive final states, the contributions from strange modes classified in the same topology are subtracted using their Monte Carlo spectral functions normalized by the measured branching fractions [9]. The measurement of the strange spectral functions has been published elsewhere [9].

The vector spectral functions of the dominant two- and four-pion modes are given in Figs. 54, 55 and 56. The error bars shown correspond to the diagonal elements of the covariance matrix. They include both statistical and systematic uncertainties. It should be pointed out that the unfolding generates strong correlations between neighbouring bins. This information is contained in the covariance matrix that is determined for each spectral function [8].

---

[8]The corrected invariant mass-squared distributions from this analysis and their covariance matrices
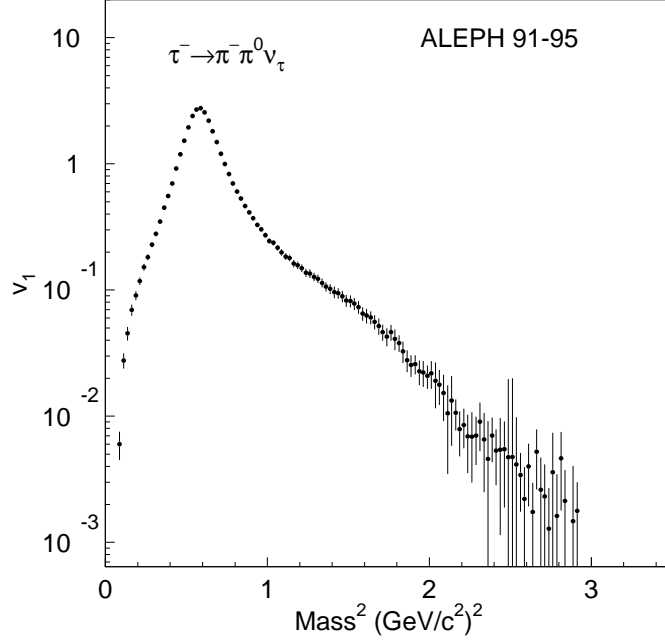
Figure 54: The spectral function for the $\pi\pi^0$ hadronic mode.

Figures 57 and 58 show the unfolded $2\pi^-\pi^+ \nu_\tau$ and $\pi^-2\pi^0 \nu_\tau$ spectral functions which are the dominant contributions to the axial-vector spectral function. Both spectra are dominated by the a_1 resonance and indeed the two distributions have consistent shape, while their normalization was already observed to agree, as expected from isospin invariance with a small correction from the slightly different charged and neutral pion masses. The comparison is seen in Fig. 59.

The 5-pion channels, $\pi^-4\pi^0\nu_\tau$, $2\pi^-\pi^+2\pi^0\nu_\tau$ and $3\pi^-2\pi^+\nu_\tau$, have small branching ratios and relatively large feedthrough background (except for the 5-charged-pion mode). Their combined mass-squared distribution, shown in Fig. 60, does not agree with the TAUOLA decay simulation in the KORALZ07 generator [18]. The experimental spectrum is harder than the phase-space model used in TAUOLA, in the absence of prior experimental information on the dynamics in these decay modes.

15.4.2 Comparison with other experiments

Spectral functions for some specific final states have been determined by CLEO and OPAL. Since the data are not presented with the same binning and furthermore plotted sometimes against the mass rather than the mass-squared, the comparison must involve some treatment of the original data.

are publicly accessible at the website http://aleph.web.lal.in2p3.fr/tau/specfun for the inclusive as well as the main exclusive channels.
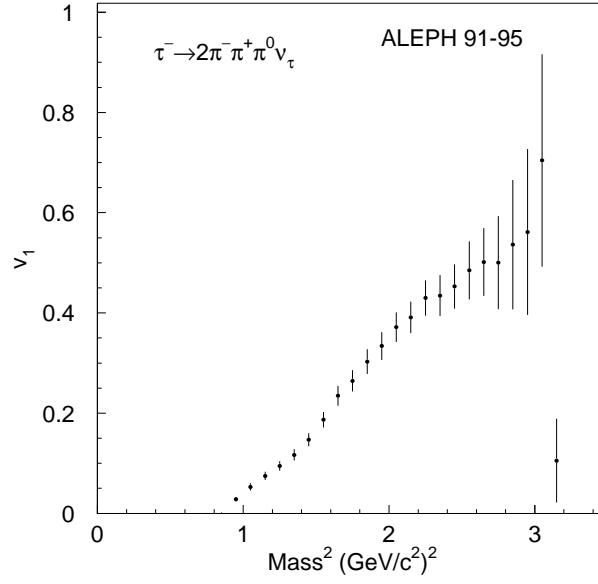
Figure 55: The spectral function for the $3\pi\pi^0$ hadronic mode. While the original spectral function is determined in 0.025 GeV^2 bins, it is rebinned here to 0.1 GeV^2 for easier reading.
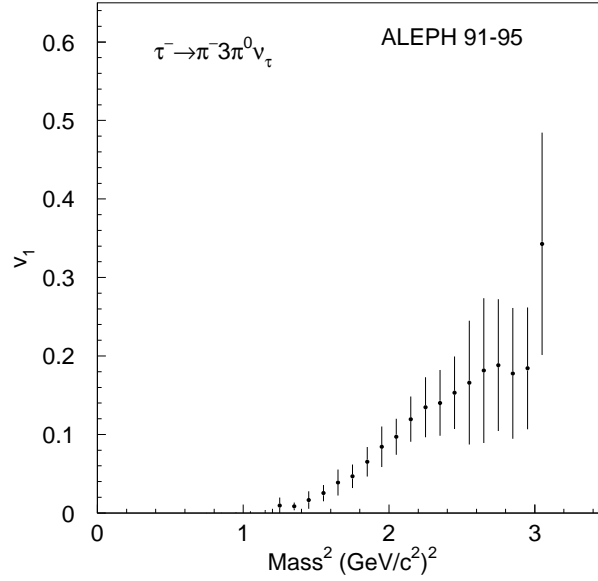
Figure 56: The spectral function for the $\pi3\pi^0$ hadronic mode. While the original spectral function is determined in 0.025 GeV^2 bins, it is rebinned here to 0.1 GeV^2 for easier reading.
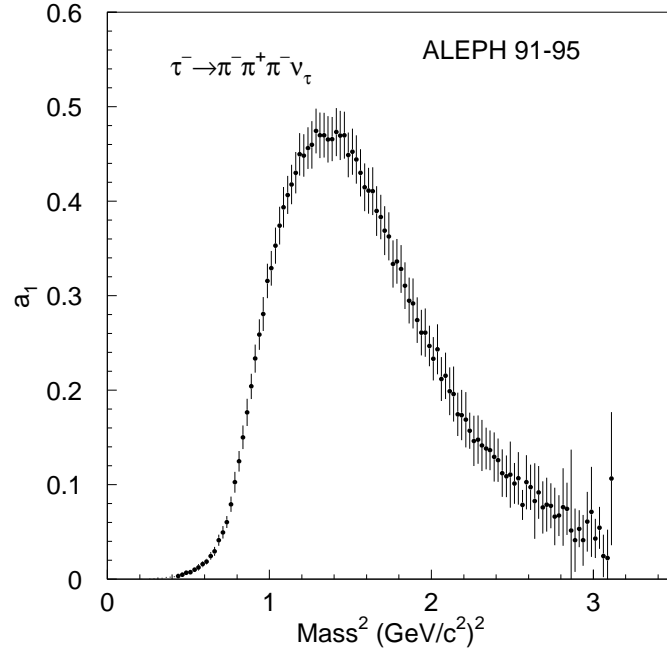
Figure 57: The spectral function for the 3π hadronic mode.
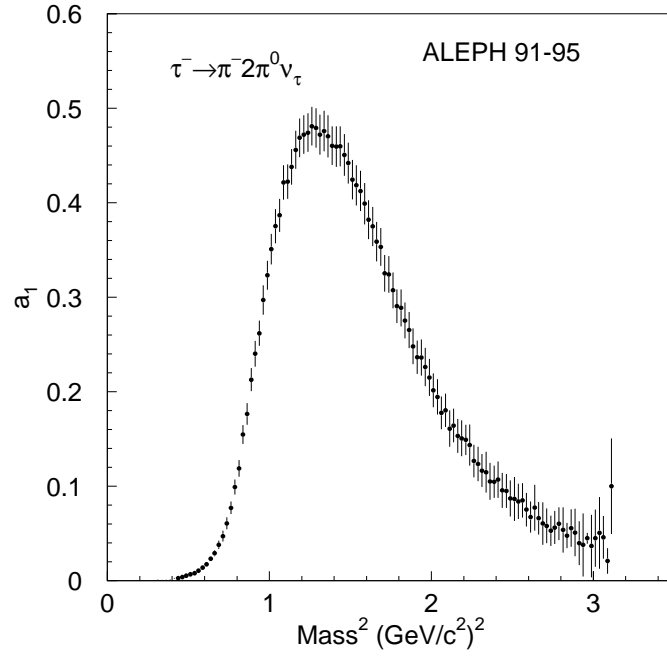
Figure 58: The spectral function for the $\pi 2\pi^0$ hadronic mode.
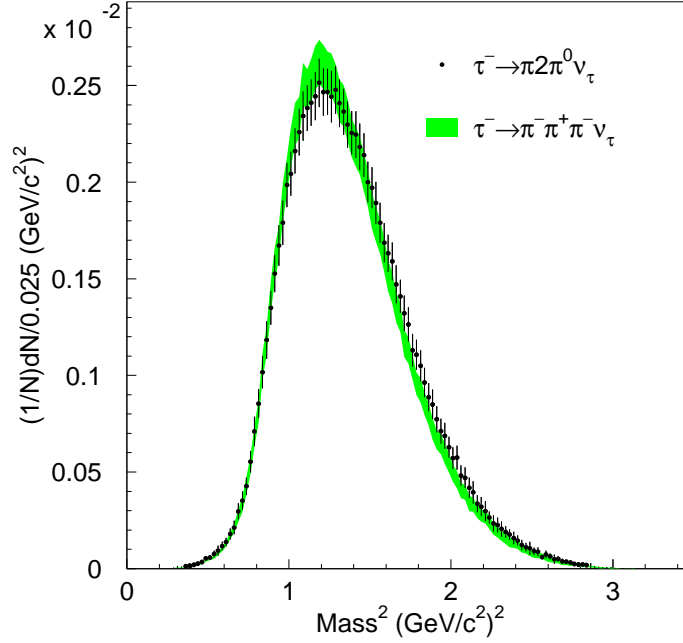
Figure 59: Comparison of the corrected mass spectra for the 3π and $\pi 2\pi^0$ hadronic modes.

The results for the $\pi\pi^0$ spectral function from ALEPH, CLEO [58], and OPAL [70] are compared in Fig. 61 in the ρ resonance region. For this comparison, each data set is normalized to the weighted mean of the three measurements. The different data are in agreement within their quoted uncertainties, when taking into account the correlation between different mass bins, particularly the strong statistical correlation between neighbouring points due to the unfolding procedure. It should be pointed out that each spectral function is normalized to the world-average branching ratio for $\tau \to \nu_\tau \pi\pi^0$ that is dominated by the ALEPH result. Hence the present exercise should be understood as a test of the shape of the spectral function. However, if the branching ratio determined by each experiment (see Section 16.2.3) is used instead, the spectral functions are still in agreement, albeit with larger uncertainties in the case of CLEO and OPAL. The two most precise results from ALEPH and CLEO do agree well. The statistics is comparable in the two cases, however due to a flat acceptance in ALEPH and a strongly increasing one in CLEO, ALEPH data are more precise below the ρ peak, while CLEO is more precise above.

15.5 Results on inclusive V, A and $V \pm A$ spectral functions

15.5.1 The vector spectral function

The inclusive τ vector spectral function with its most important contributions is shown in Fig. 62. The dashed line depicts the naive parton model prediction while the massless
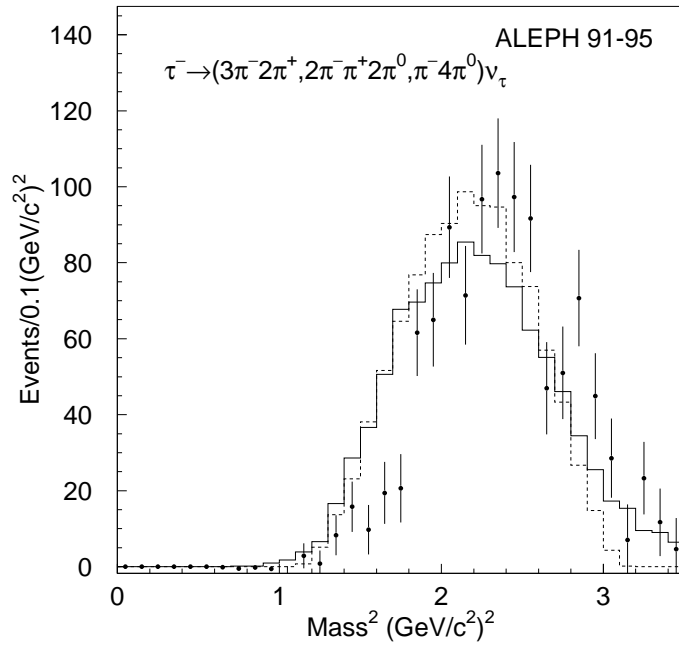
Figure 60: Comparison of the background-subtracted mass-squared spectrum in the 5-pion modes ($\pi^-4\pi^0\nu_\tau$, $2\pi^-\pi^+2\pi^0\nu_\tau$ and $3\pi^-2\pi^+\nu_\tau$) with the phase-space model used in the TAUOLA decay generator [18]. The dashed histogram is the generated distribution, while the solid histogram is the reconstructed spectrum with the detector response which can be directly compared to the data (points). A clear disagreement is observed.
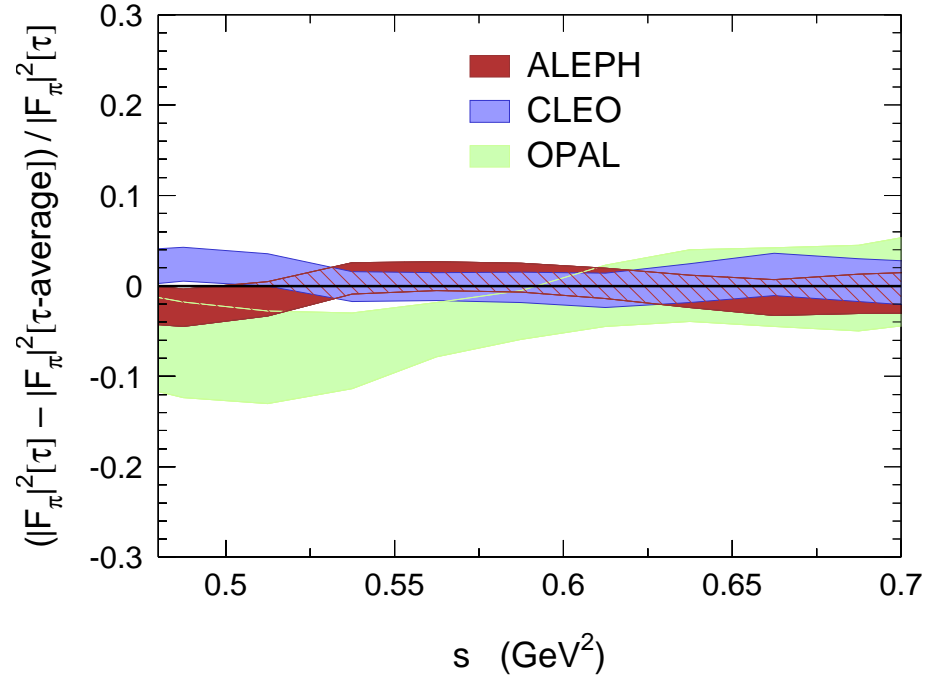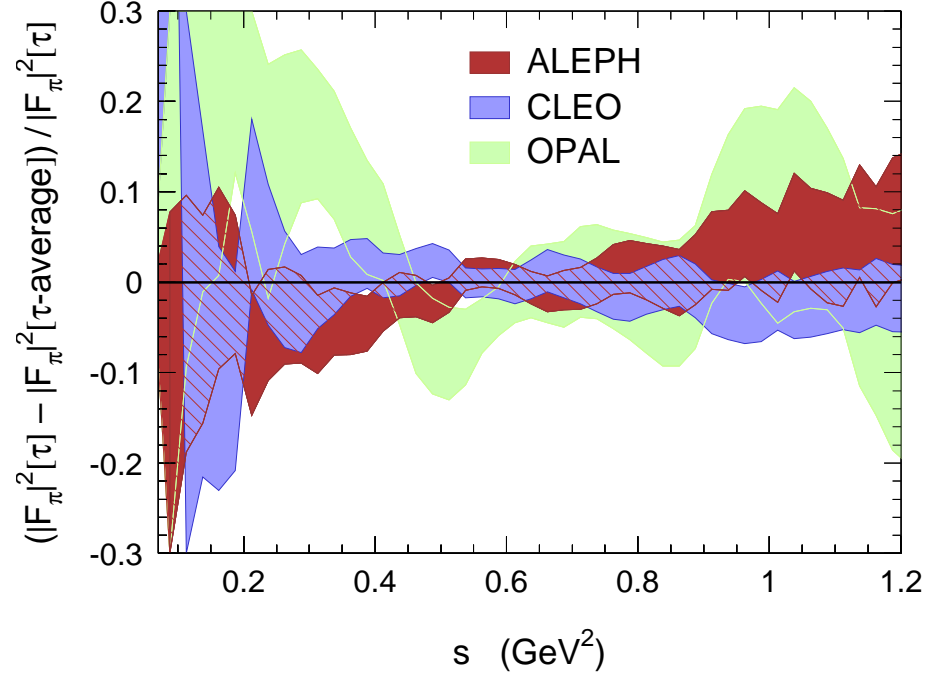
Figure 61: Relative comparison of the $\pi^+\pi^-$ spectral functions extracted from τ data from different experiments, expressed as a ratio to the average τ spectral function. The lower figure emphasizes the ρ region. For CLEO only statistical errors are shown.
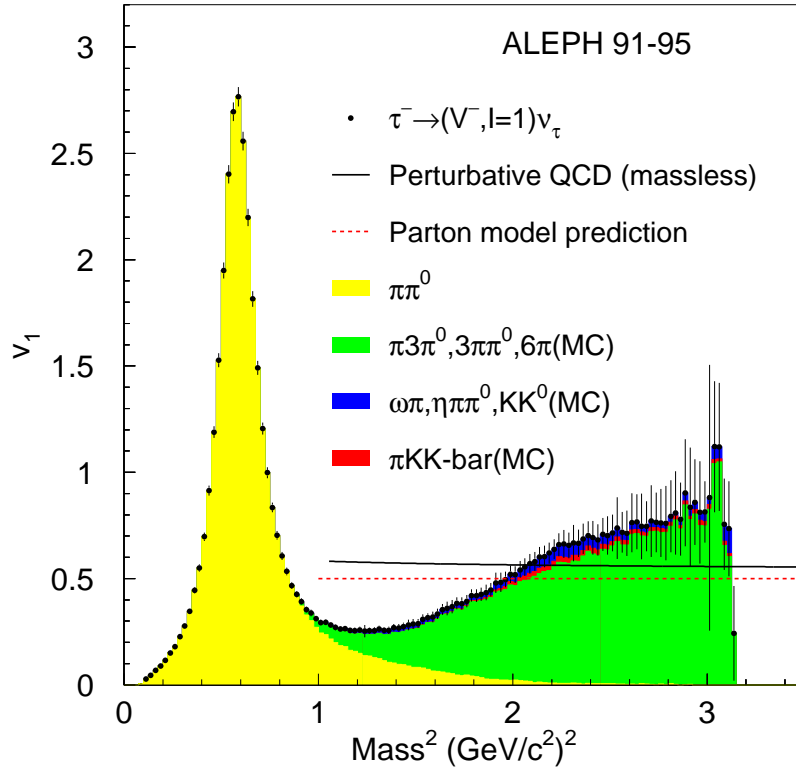
Figure 62: The total vector spectral function. The shaded areas indicate the contributions from the exclusive τ vector channels, where the shapes of the contributions labelled 'MC' are taken from the Monte Carlo simulation. The lines show the predictions from the naive parton model and from massless perturbative QCD using $\alpha_s(M_Z^2) = 0.120$.

perturbative QCD prediction [71] using $\alpha_s(M_Z^2) = 0.120$ (solid line) lies roughly 25% lower than the data at m_τ^2. Although the statistical power of the data is weak near the kinematic limit, the trend of the spectral function clearly indicates that the asymptotic region is not reached.

The two- and four-pion final states are measured exclusively, while the six-pion state is only partly measured. The total six-pion branching ratio has been determined in [11] using isospin symmetry. However, one has to account for the fact that the six-pion channel is contaminated by isospin-violating $\tau^- \to \eta\, 2\pi^-\pi^+\, \nu_\tau$, $\eta\, \pi^- 2\pi^0\, \nu_\tau$ decays, as reported by the CLEO Collaboration [27].

The small fraction of the $\omega\, \pi^-\, \nu_\tau$ decay channel that is not reconstructed in the four-pion final state is added using the simulation. Similarly, one corrects for $\eta\pi^-\pi^0\, \nu_\tau$ decay modes where η decays into pions. For the $\eta \to 2\gamma$ mode, the τ decay is classified in the $h3\pi^0\nu_\tau$ final state, since the two-photon mass is inconsistent with the π^0 mass and consequently each photon is reconstructed as a π^0.

The $K^- K^0 \nu_\tau$ mass distribution is taken entirely from the simulation. The vector contributions in the $K\overline{K}\pi$ and $K\overline{K}\pi\pi$ modes are taken from Section 14.5. The corresponding spectral functions are obtained from the Monte Carlo simulation.

The invariant mass spectra of the small contributions labelled 'MC' in Figs. 62 and 63 are taken from the Monte Carlo simulation accompanied by a channel-dependent systematic error of up to 50% of the bin entry.

15.5.2   The axial-vector spectral function

In complete analogy to the vector spectral function, the inclusive axial-vector spectral function is obtained by summing up the exclusive axial-vector spectral functions with the addition of small unmeasured modes taken from the Monte Carlo simulation.

The small fraction of the $\omega\pi^-\pi^0\, \nu_\tau$ decay channel that is not accounted for in the $2\pi^-\pi^+2\pi^0\, \nu_\tau$ final state is added from the simulation. Also considered are the axial-vector $\eta\, (3\pi)^-\, \nu_\tau$ final states [27]. CLEO observed that the dominant part of this mode issues from the $\tau^- \to f_1(1285)\pi^-$ intermediate state, with $B(\tau^- \to f_1\pi^- \nu_\tau) = (0.068 \pm 0.030)\%$, measured in the $f_1 \to \eta\, \pi^+\pi^-$ and $f_1 \to \eta\, \pi^0\pi^0$ decay modes [27]. Since the f_1 meson is isoscalar, the branching ratios relate as $B(\tau^- \to \eta\, 2\pi^-\pi^+ \nu_\tau) = 2 \times B(\tau^- \to \eta\, \pi^- 2\pi^0\, \nu_\tau)$. The distributions are taken from the ordinary six-pion phase space simulation accompanied by large systematic errors. As discussed for the vector spectral function, the $K\overline{K}\pi$ final states contribute dominantly to the inclusive axial-vector spectral function, with full anticorrelation to the inclusive vector spectral function. Invariant mass distributions for these channels are taken from the simulation.

The total inclusive axial-vector spectral function is plotted in Fig. 63 together with the naive parton model and the massless, perturbative QCD prediction. One observes that the asymptotic region is apparently not reached at the τ mass scale.
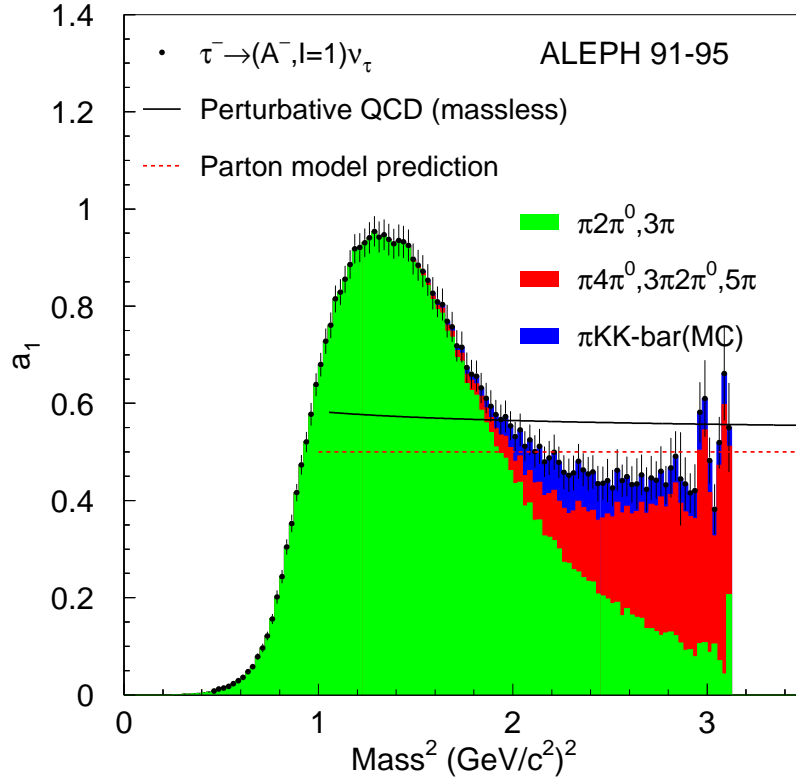
Figure 63: The total axial-vector spectral function. The shaded areas indicate the contributions from the exclusive τ vector channels, where the shapes of the contributions labelled 'MC' are taken from the Monte Carlo simulation. The lines show the predictions from the naive parton model and from massless perturbative QCD using $\alpha_s(M_Z^2) = 0.120$.
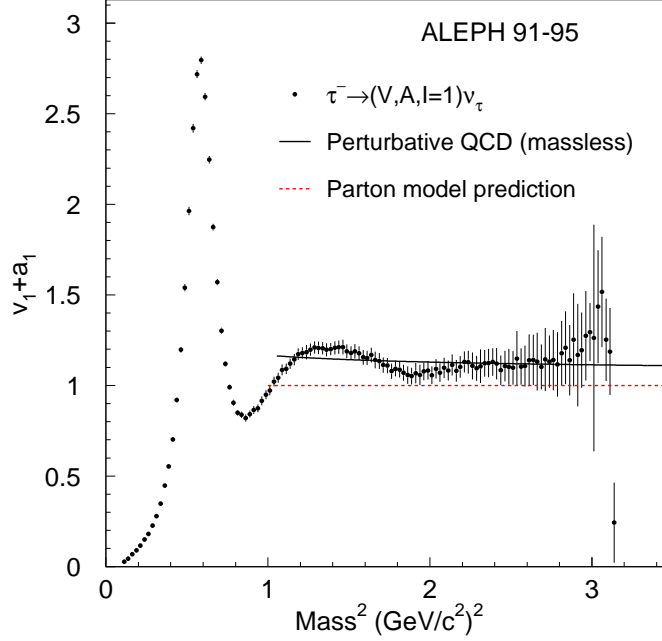
Figure 64: The inclusive vector plus axial-vector (v_1+a_1) spectral function and predictions from the parton model and from massless perturbative QCD using $\alpha_s(M_Z^2) = 0.120$.

15.5.3 The $V \pm A$ spectral functions

For the total $(v_1 + a_1)$ hadronic spectral function one does not have to distinguish the current properties of the non-strange hadronic τ decay channels. Hence the mixture of all contributing non-strange final states is measured inclusively using the following procedure.

The two- and three-pion final states dominate and their exclusive measurements are added with proper accounting for the correlations. The remaining contributing topologies are treated inclusively, *i.e.*, without separation of the vector and axial-vector decay modes. This reduces the statistical uncertainty. The effect of the feedthrough between τ final states on the invariant mass spectrum is described by the Monte Carlo simulation and thus corrected in the data unfolding. In this procedure the simulated mass distributions are iteratively corrected using the exclusive vector/axial-vector unfolded mass spectra. Another advantage of the inclusive $(v_1 + a_1)$ measurement is that one does not have to separate the vector/axial-vector currents of the $K\overline{K}\pi$ and $K\overline{K}\pi\pi$ modes. The $(v_1 + a_1)$ spectral function is depicted in Fig. 64. The improvement in precision when comparing to a sum of the two parts (Fig. 62 and Fig. 63) is obvious at higher mass-squared.

One clearly sees the oscillating behaviour of the spectral function but, unlike the vector/axial-vector spectral functions, it does approximately reach the asymptotic limit predicted by perturbative QCD at $s \rightarrow m_\tau^2$. Also, the $V + A$ spectral function, including the δ-function π contribution, exhibits the features expected from global quark-hadron duality: despite the huge oscillatory effects from π, and ρ, a_1 and ρ' hadron
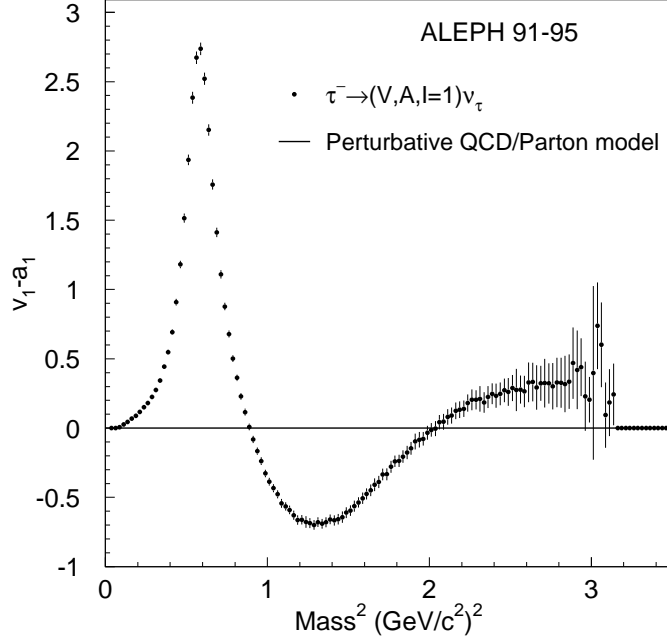
Figure 65: The vector minus axial-vector $(v_1 - a_1)$ spectral function. In the parton model as well as in perturbative QCD vector and axial-vector contributions are degenerate.

resonances, the spectral function qualitatively averages out to the quark contribution from perturbative [72]. This observation is the physical basis for the quantitative QCD analysis performed in Section 17.

In the case of the $(v_1 - a_1)$ spectral function, uncertainties on the V/A separation are reinforced due to their anticorrelation. In addition, anticorrelations in the branching ratios between τ final states with adjacent numbers of pions increase the errors. The $(v_1 - a_1)$ spectral function is shown in Fig. 65. The oscillating behaviour of the respective v_1 and a_1 spectral functions is emphasized and the asymptotic behaviour is clearly not reached at m_τ^2. However again here, the oscillation generated by the hadron resonances qualitatively averages out to zero, as predicted by perturbative QCD.

16 The vector spectral functions and tests of CVC

16.1 General remarks on spectral functions in τ decays and e^+e^- annihilation

Using the optical theorem and in the limit of isospin invariance (implicit in the hypothesis of CVC—Conserved Vector Current) the spectral function of a τ decay mode $X^-\nu_\tau$, where the hadronic system X is in a vector state, is related to the e^+e^- annihilation cross section

of the corresponding isovector final state X^0:

$$\sigma_{e^+e^- \to X^0}^{I=1} = \frac{4\pi\alpha^2}{s} v_{1,X^-} , \tag{48}$$

with the electromagnetic fine structure constant α.

Since the breaking of isospin symmetry is expected at some level, in particular from electromagnetic effects, it is useful to carefully write down all the factors involved in the comparison of e^+e^- and τ spectral functions in order to make explicit the possible sources of CVC breakdown. For the dominant $\pi\pi$ spectral functions, one has on the e^+e^- side

$$\sigma(e^+e^- \longrightarrow \pi^+\pi^-) = \frac{4\pi\alpha^2}{s} v_0(s) , \tag{49}$$

$$v_0(s) = \frac{\beta_0^3(s)}{12\pi} |F_\pi^0(s)|^2,$$

where $\beta_0^3(s)$ is the threshold kinematic factor and $F_\pi^0(s)$ the pion form factor. On the τ side, the physics is contained in the hadronic mass distribution through

$$\frac{1}{\Gamma}\frac{d\Gamma}{ds}(\tau \longrightarrow \pi^-\pi^0\nu_\tau) =$$
$$\frac{6\pi|V_{ud}|^2 S_{EW}}{m_\tau^2} \frac{B_e}{B_{\pi\pi^0}} C(s)v_-(s) , \tag{50}$$

$$v_-(s) = \frac{\beta_-^3(s)}{12\pi} |F_\pi^-(s)|^2 ,$$

$$C(s) = \left(1 - \frac{s}{m_\tau^2}\right)^2 \left(1 + \frac{2s}{m_\tau^2}\right) .$$

SU(2) symmetry implies $v_-(s) = v_0(s)$. The threshold functions $\beta_{0,-}$ are defined by

$$\beta_{0,-} = \beta(s, m_{\pi^-}, m_{\pi^0,-}) , \tag{51}$$

where

$$\beta(s, m_1, m_2) = \left[\left(1 - \frac{(m_1 + m_2)^2}{s}\right)\left(1 - \frac{(m_1 - m_2)^2}{s}\right)\right]^{1/2} . \tag{52}$$

In this analysis of τ decays the rate is measured inclusively with respect to radiative photons, i.e., for $\tau \to \nu_\tau \pi\pi^0(\gamma)$. The measured spectral function is thus $v_-^*(s) = v_-(s) G(s)$, where $G(s)$ is a radiative correction.

Several levels of SU(2) breaking can be identified.

- *Electroweak radiative corrections to τ decays* are contained in the S_{EW} factor [50, 73] which is dominated by short-distance effects. As such it is expected to be weakly dependent on the specific hadronic final state, as verified in the $\tau \to (\pi, K)\nu_\tau$ channels [53]. Recently, detailed calculations have been performed for

the $\pi\pi^0$ channel [24], which also confirm the relative smallness of the long-distance contributions. The total correction is

$$S_{EW} = \frac{S_{EW}^{\text{had}} S_{EM}^{\text{had}}}{S_{EM}^{\text{lep}}} \tag{53}$$

where S_{EW}^{had} is the leading-log short-distance electroweak factor (which vanishes for leptons) and $S_{EM}^{\text{had,lep}}$ are the nonleading electromagnetic corrections. The latter corrections are calculated in Ref. [73] at the quark level and in Ref. [24] at the hadron level for the $\pi\pi^0$ decay mode, and in Refs. [50, 73] for leptons. The total correction amounts [57] to $S_{EW}^{\text{inclu}} = 1.0198 \pm 0.0006$ for the inclusive hadron decay rate and $S_{EW}^{\pi\pi^0} = (1.0232 \pm 0.0006) \, G_{EM}^{\pi\pi^0}(s)$ for the $\pi\pi^0$ decay mode, where $G_{EM}^{\pi\pi^0}(s)$ is an s-dependent radiative correction [24].

- *The pion mass splitting* breaks isospin symmetry in the spectral functions [54, 74] since $\beta_-(s) \neq \beta_0(s)$.

- Isospin symmetry is also broken in *the pion form factor* [54, 24] from the π mass splitting.

- A similar effect is expected from *the ρ mass splitting*. The theoretical expectation [75] gives a limit (< 0.7 MeV), but this is only a rough estimate. Hence the question must be investigated experimentally, the best approach being the explicit comparison of τ and e^+e^- 2π spectral functions, after correction for the other isospin-breaking effects. No correction for ρ mass splitting is applied initially.

- Explicit *electromagnetic decays* such as $\pi\gamma$, $\eta\gamma$, l^+l^- and $\pi\pi\gamma$ introduce small differences between the widths of the charged and neutral ρ's.

- Isospin violation in the strong amplitude through the *mass difference between u and d quarks* is expected to be negligible.

- An obvious, but large correction must be applied to the τ spectral function to introduce the effect of $\rho - \omega$ mixing, only present in the neutral channel. This correction is computed using the parameters determined in the e^+e^- experiments in their fits of the $\pi^+\pi^-$ lineshape taking into account the $\rho - \omega$ interference [60].

16.2 Comparison with e^+e^- results

16.2.1 The 2π spectral function

Figure 66 shows the comparison for the 2π spectral functions obtained by averaging the results of the present analysis and the published data from CLEO [58] and OPAL [70]. The e^+e^- data are taken from TOF [76], OLYA [77], CMD [78], CMD-2 [60], DM1 [79], DM2 [80], and NA7 [81]. The most precise results come from CMD-2 and have undergone recently a major revision due to previously incorrect radiative corrections [59]. Visually, the agreement seems satisfactory, however the large dynamical range involved does not

permit an accurate test. To do so, the e^+e^- data are plotted as a point-by-point ratio to the τ spectral function in Fig. 67, also showing the recent accurate data from KLOE [82] using the radiative return technique. The data are found to be consistent below and around the ρ peak, while a discrepancy is observed for masses larger than 0.85 GeV.

16.2.2 The 4π spectral functions

The spectral function measurements of the τ vector current final states $\pi^-3\pi^0$ and $2\pi^-\pi^+\pi^0$ are compared to the cross sections of the corresponding e^+e^- annihilation into the isovector states $2\pi^-2\pi^+$ and $\pi^-\pi^+2\pi^0$. Using Eq. (46) and isospin invariance the following relations hold:

$$\sigma^{I=1}_{e^+e^-\to\pi^+\pi^-\pi^+\pi^-} = 2\cdot\frac{4\pi\alpha^2}{s}\,v_{1,\,\pi^-\,3\pi^0\,\nu_\tau}\;, \tag{54}$$

$$\sigma^{I=1}_{e^+e^-\to\pi^+\pi^-\pi^0\pi^0} = \frac{4\pi\alpha^2}{s}\left[v_{1,\,2\pi^-\pi^+\pi^0\,\nu_\tau} - v_{1,\,\pi^-\,3\pi^0\,\nu_\tau}\right]\;. \tag{55}$$

The comparison of the 4π cross sections is given in Fig. 68 for the $2\pi^+2\pi^-$ channel and in Fig. 69 for $\pi^+\pi^-2\pi^0$, where the latter suffers from large differences between the results from the various e^+e^- experiments. The τ data, combining two measured spectral functions according to Eq. (55) and corrected for isospin breaking originating from the charged-vs-neutral pion mass difference[74], lie somewhat in between with large uncertainties above 2 GeV^2 because of the lack of statistics and a large feedthrough background in the $\tau\to\nu_\tau\,\pi^-3\pi^0$ mode. In spite of these difficulties the $\pi^-3\pi^0$ spectral function is in agreement with e^+e^- data as can be seen in Fig. 68. It is clear that intrinsic discrepancies exist among the e^+e^- experiments and that a quantitative test of CVC in the $\pi^+\pi^-2\pi^0$ channel is premature.

16.2.3 Branching Ratios in τ Decays and CVC

It is possible to compare the e^+e^- and τ spectral functions in a more quantitative way by calculating weighted integrals over the mass range of interest up to the τ mass. One convenient choice is provided by the τ branching fractions which involve as a weight the kinematic factor $(1-\frac{s}{m_\tau^2})^2(1+\frac{2s}{m_\tau^2})$ coming from the $V-A$ charged current in τ decay. It is then possible to directly compare the measured τ branching ratios to their prediction through isospin invariance (CVC) using as input the e^+e^- isovector spectral functions.

Using the "universality-improved" branching fraction given in Eq. (32), the results for the main channels are given in Table 18. The errors quoted for the CVC values are split into uncertainties from (*i*) the experimental input (the e^+e^- annihilation cross sections) and the numerical integration procedure, (*ii*) additional radiative corrections applied to some of the e^+e^- data (see Ref. [57] for details), and (*iii*) the isospin-breaking corrections when relating τ and e^+e^- spectral functions.

As expected from the preceding discussion, a large discrepancy is observed for the $\tau\to$

Figure 66: Comparison of the $\pi^+\pi^-$ spectral functions from e^+e^- and isospin-breaking corrected τ data from ALEPH, CLEO, and OPAL expressed as e^+e^- cross sections. The band indicates the combined e^+e^- and τ result within 1σ errors. It is given for illustration purpose only. The complete references for the e^+e^- data are given in Refs. [57, 61] and [81].

Figure 67: Relative comparison of the $\pi^+\pi^-$ spectral functions from e^+e^- and isospin-breaking corrected τ data from ALEPH, CLEO, and OPAL expressed as a ratio to the τ spectral function. The band shows the uncertainty on the latter function. The complete references for the e^+e^- data are given in Refs. [57, 61] and [82].

Figure 68: Comparison of the $2\pi^+2\pi^-$ spectral functions from e^+e^- and isospin-breaking corrected τ data, expressed as e^+e^- cross sections. The complete references for the e^+e^- data are given in Refs. [57, 61].
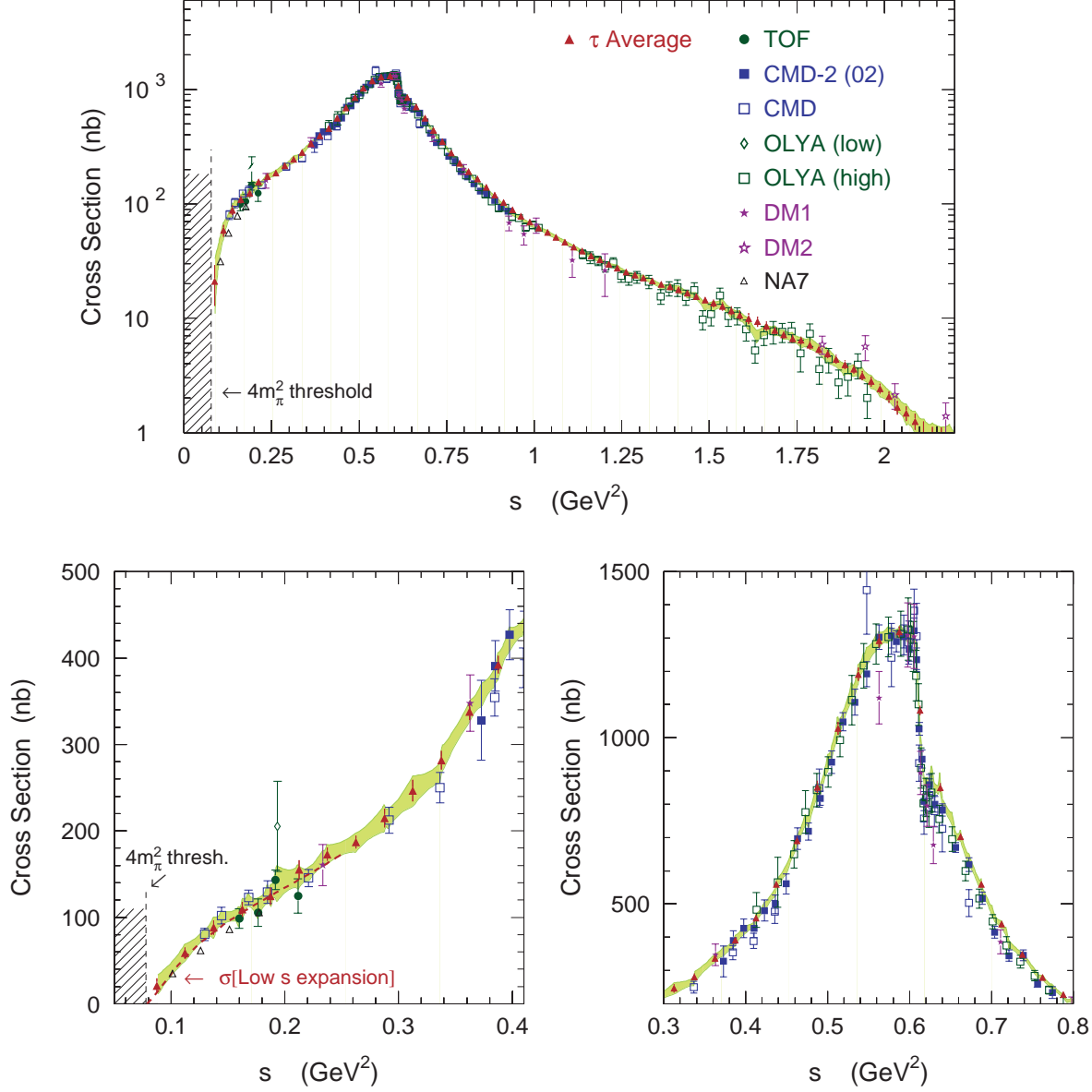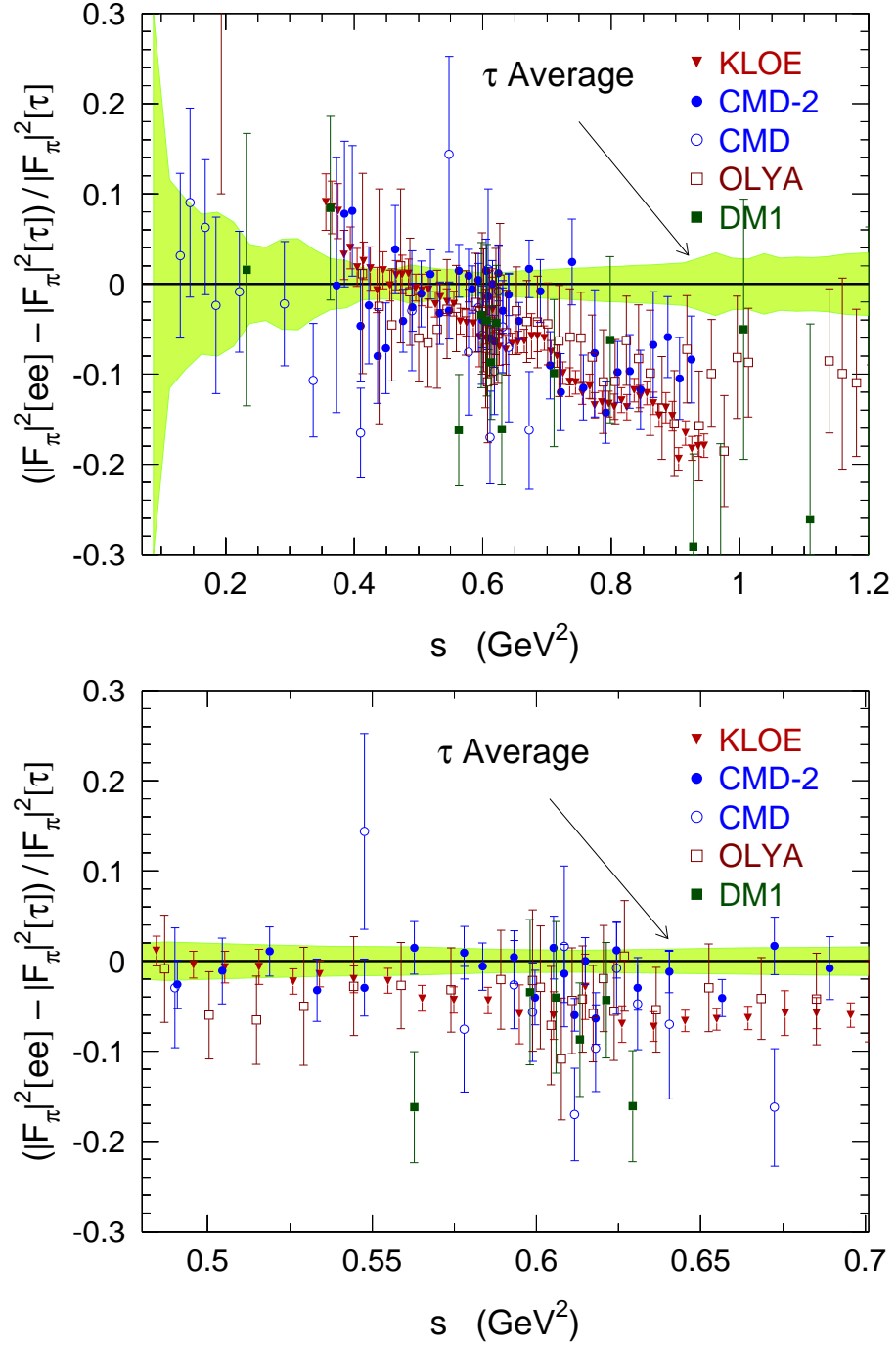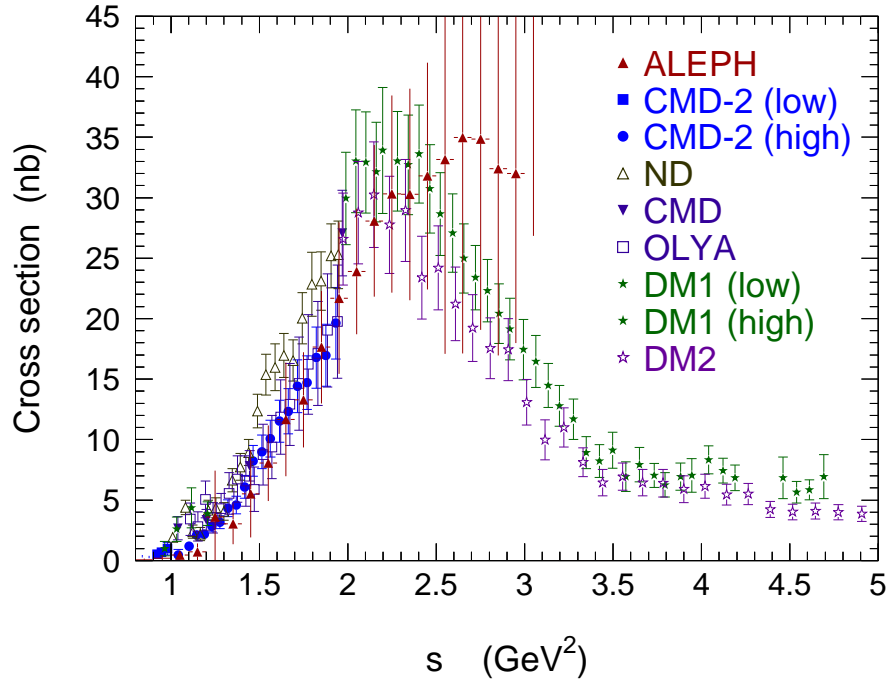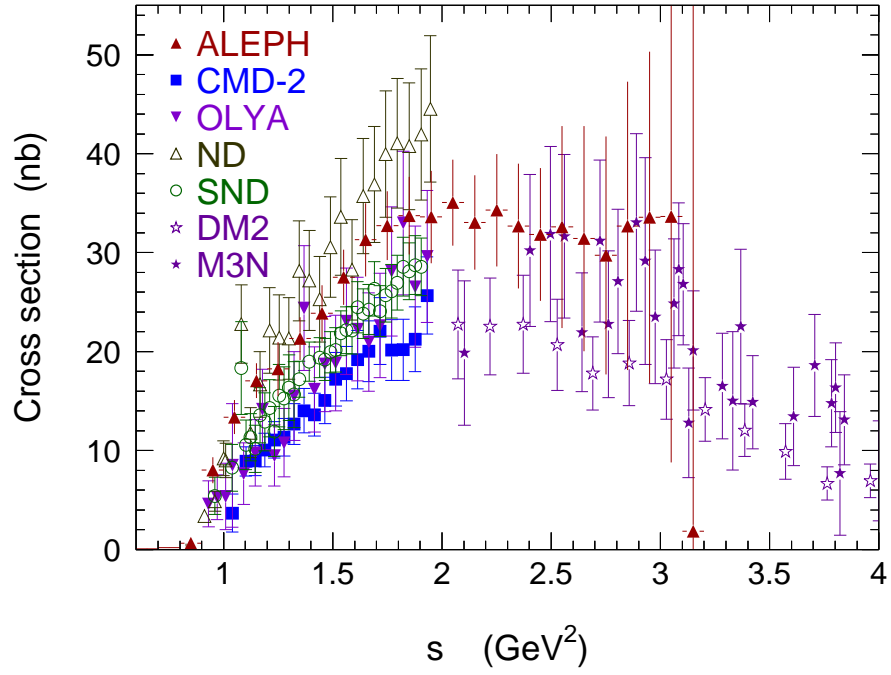
Figure 69: Comparison of the $\pi^+\pi^-2\pi^0$ spectral functions from e^+e^- and isospin-breaking corrected τ data, expressed as e^+e^- cross sections. The complete references for the e^+e^- data are given in Refs. [57, 61].

Table 18: Branching fractions of τ vector decays into 2 and 4 pions in the final state. Second column: present ALEPH results. Third column: inferred from e^+e^- spectral functions using the isospin relations (48,50,51,54, 55) and correcting for isospin breaking following Refs. [57, 61]. Experimental errors, including uncertainties on the integration procedure, and theoretical (missing radiative corrections for e^+e^-, and isospin-breaking corrections and V_{ud} for τ) are shown separately. Right column: differences between the direct measurements in τ decays and the CVC evaluations, where the separate errors have been added in quadrature.

| Mode | Branching fractions (in %) | | |
	τ ALEPH	e^+e^- via CVC	$\Delta(\tau - e^+e^-)$
$\tau^- \to \nu_\tau \pi^- \pi^0$	25.47 ± 0.13	$24.52 \pm \underbrace{0.26_{\mathrm{exp}} \pm 0.11_{\mathrm{rad}} \pm 0.12_{\mathrm{SU(2)}}}_{0.31}$	$+0.95 \pm 0.33$
$\tau^- \to \nu_\tau \pi^- 3\pi^0$	0.98 ± 0.09	$1.09 \pm \underbrace{0.06_{\mathrm{exp}} \pm 0.02_{\mathrm{rad}} \pm 0.05_{\mathrm{SU(2)}}}_{0.08}$	-0.11 ± 0.12
$\tau^- \to \nu_\tau 2\pi^- \pi^+ \pi^0$	4.59 ± 0.09	$3.63 \pm \underbrace{0.19_{\mathrm{exp}} \pm 0.04_{\mathrm{rad}} \pm 0.09_{\mathrm{SU(2)}}}_{0.21}$	$+0.96 \pm 0.23$

$\nu_\tau \pi^- \pi^0$ branching ratio, with a difference of $(0.95 \pm 0.13_\tau \pm 0.26_{ee} \pm 0.11_{\mathrm{rad}} \pm 0.12_{\mathrm{SU(2)}})\%$, where the uncertainties are from the τ branching ratio, e^+e^- cross sections, e^+e^- missing radiative corrections and isospin-breaking corrections (including the uncertainty on V_{ud}), respectively. Adding all errors in quadrature, the effect represents a 2.9 σ discrepancy. Since the disagreement between e^+e^- and τ spectral functions is more pronounced at energies above 0.85 GeV, a smaller discrepancy is expected in the calculation of the hadronic contribution to the muon anomalous magnetic moment because, in this case, the spectral function is weighted by a steeply falling kernel $K(s)$.

Besides the result from the present analysis, a similar comparison can be performed using results from other experiments. The values for the τ branching ratios involve measurements [37, 36] given without charged hadron identification, *i.e.* for the $h\pi^0\nu_\tau$, $h3\pi^0\nu_\tau$ and $3h\pi^0\nu_\tau$ final states. The corresponding channels with charged kaons have been measured [9, 83] and their contributions are subtracted out in order to obtain the pure pionic modes. The comparison is displayed in Fig. 70 where it is clear that ALEPH, CLEO, and OPAL all separately disagree with the e^+e^--based CVC result.

The situation in the 4π channels is different. Agreement is observed for the $\pi^-3\pi^0$ mode within a relative accuracy of 12%, however the comparison is not satisfactory for the $2\pi^-\pi^+\pi^0$ mode. In the latter case, the relative difference is very large, $(23 \pm 6)\%$, compared to a reasonable level of isospin symmetry breaking. As such, it rather points to experimental problems that have to be investigated, which are emphasized by the scatter observed among the different e^+e^- results. In this respect, it is to be noted that new preliminary results from the SND and CMD-2 experiments have been recently
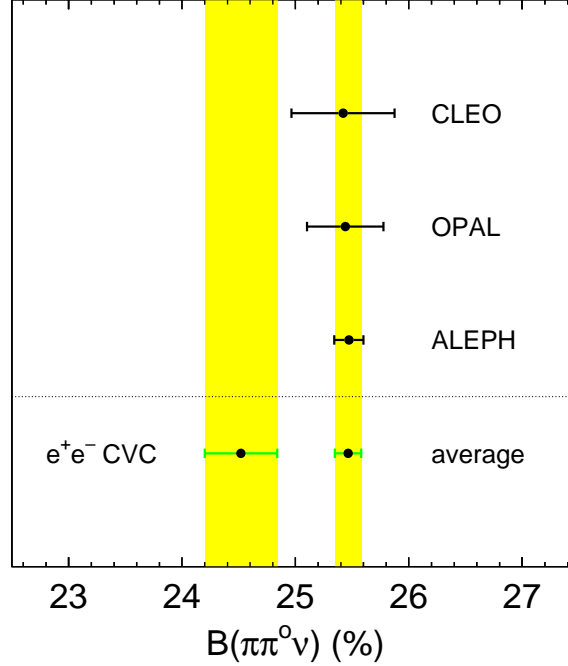
Figure 70: The measured branching ratios for $\tau \to \nu_\tau \pi^- \pi^0$ compared to the prediction from the $e^+e^- \to \pi^+\pi^-$ spectral function applying the isospin-breaking correction factors discussed in Section 16.1. The measured branching ratios are from ALEPH, CLEO [37] and OPAL [36]. The OPAL result was obtained from their $h\pi^0$ branching ratio, reduced by the small $K\pi^0$ contribution measured by ALEPH [9] and CLEO [83].

presented [84]; while the new data contradict earlier results from the same experiments, they are in good agreement with the ALEPH spectral functions.

16.3   Fits to the $\pi\pi^0$ spectral function

16.3.1   Procedure

The $\pi\pi^0$ spectral function is dominated by the wide ρ resonance, parametrized in the forthcoming fits following Gounaris-Sakurai [85] (GS). The GS parametrization takes into accounts analyticity and unitarity properties. The fits make use of the covariance matrix taking into account the correlations between different mass bins.

If one assumes vector dominance, the pion form factor is given by interfering amplitudes from the known isovector meson resonances $\rho(770)$, $\rho(1450)$ and $\rho(1700)$ with relative strengths 1, β, and γ. Although one could expect from the quark model that β and γ are real and respectively negative and positive, the phase of β, ϕ_β is left free in the fits, while the much smaller γ is assumed to be real for lack of precise experimental

information at large masses. Taking into account $\rho - \omega$ interference, one writes

$$F_\pi^{I=1,0}(s) = \frac{\mathrm{BW}_{\rho(770)}(s)\,\frac{1+\delta\,\mathrm{BW}_{\omega(783)}(s)}{1+\delta} \;+\; \beta\,\mathrm{BW}_{\rho(1450)}(s) \;+\; \gamma\,\mathrm{BW}_{\rho(1700)}(s)}{1 \,+\, \beta \,+\, \gamma} \;, \qquad (56)$$

with the Breit-Wigner propagators

$$\mathrm{BW}^{\mathrm{GS}}_{\rho(m_\rho)}(s) \;=\; \frac{m_\rho^2(\,1 + d\cdot\Gamma_\rho/m_\rho)}{m_\rho^2 \,-\, s \,+\, f(s) \,-\, i\sqrt{s}\,\Gamma_\rho(s)} \;, \qquad (57)$$

where

$$f(s) \;=\; \Gamma_\rho \frac{m_\rho^2}{k^3(m_\rho^2)} \left[k^2(s)\left(h(s) - h(m_\rho^2)\right) \;+\; (m_\rho^2 - s)\,k^2(m_\rho^2)\,\frac{dh}{ds}\bigg|_{s=m_\rho^2} \right]. \qquad (58)$$

The P-wave energy-dependent width is given by

$$\Gamma_\rho(s) \;=\; \Gamma_\rho(m_\rho^2)\,\frac{m_\rho}{\sqrt{s}}\left(\frac{k(s)}{k(m_\rho^2)}\right)^3 \;, \qquad (59)$$

where $k(s) = \frac{1}{2}\sqrt{s}\,\beta^-(s)$ and $k(m_\rho^2)$ are pion momenta in the ρ rest frame. The function $h(s)$ is defined as

$$h(s) \;=\; \frac{2}{\pi}\,\frac{k(s)}{\sqrt{s}}\,\ln\frac{\sqrt{s}+2k(s)}{2m_\pi} \;, \qquad (60)$$

with $dh/ds|_{m_\rho^2} = h(m_\rho^2)\left[(8k^2(m_\rho^2))^{-1} - (2m_\rho^2)^{-1}\right] + (2\pi m_\rho^2)^{-1}$. Interference with the isospin-violating electromagnetic $\omega \to \pi^+\pi^-$ decay occurs only in e^+e^- annihilation. Consequently, δ is fixed to zero when fitting τ data. The normalization $\mathrm{BW}^{\mathrm{GS}}_{\rho(m_\rho)}(0) = 1$ fixes the parameter $d = f(0)/(\Gamma_\rho m_\rho)$, which is found to be [85]

$$d \;=\; \frac{3}{\pi}\,\frac{m_\pi^2}{k^2(m_\rho^2)}\,\ln\frac{m_\rho + 2k(m_\rho^2)}{2m_\pi} \;+\; \frac{m_\rho}{2\pi\,k(m_\rho^2)} \;-\; \frac{m_\pi^2 m_\rho}{\pi\,k^3(m_\rho^2)} \;. \qquad (61)$$

16.3.2 Fit to the ALEPH data

The result of the fit to the ALEPH data using the GS parametrization is given in Table 19 and illustrated in Fig 71. The ρ mass uncertainty is dominated by systematic effects, the largest being the knowledge of the π^0 energy scale (calibration).

Concluding from Table 19, the fit establishes a need for the $\rho(1450)$ contribution to the weak pion form factor. Weak evidence is found for a $\rho(1700)$ contribution which is expected since the resonance lies close to the spectrum end-point. Most of the fitted parameters exhibit large correlations as seen in Table 20.

Table 19: Fit results of the ALEPH pion form factor in $\tau^- \to \pi^- \pi^0 \nu_\tau$ decays using the Gounaris-Sakurai (GS) parametrization. The parameters $m_{\rho^\pm(1700)}$ and $\Gamma_{\rho(1700)}$ are kept fixed to values obtained from fits of e^+e^- data extending in mass-squared up to 3.6 GeV^2.

Parameter	ALEPH GS
$m_{\rho^\pm(770)}$ (MeV)	775.5 ± 0.7
$\Gamma_{\rho^\pm(770)}$ (MeV)	149.0 ± 1.2
β	0.120 ± 0.008
ϕ_β (degrees)	153 ± 7
$m_{\rho^\pm(1450)}$ (MeV)	1328 ± 15
$\Gamma_{\rho(1450)}$(MeV)	468 ± 41
γ	0.023 ± 0.008
$m_{\rho^\pm(1700)}$ (MeV)	[1713]
$\Gamma_{\rho(1700)}$ (MeV)	[235]
χ^2/DF	119/110

Table 20: The correlation coefficients between the fitted parameters in the fit of the ALEPH $\pi\pi^0$ spectral function.

ALEPH	$m_{\rho(770)}$	$\Gamma_{\rho(770)}$	β	ϕ_β	$m_{\rho(1450)}$	$\Gamma_{\rho(1450)}$	γ
$m_{\rho(770)}$	1	0.38	0.29	-0.28	0.42	0.46	-0.36
$\Gamma_{\rho(770)}$	–	1	0.52	-0.02	0.16	0.71	-0.38
β	–	–	1	0.31	-0.08	0.63	0.03
ϕ_β	–	–	–	1	-0.87	-0.40	0.77
$m_{\rho(1450)}$	–	–	–	–	1	0.58	-0.94
$\Gamma_{\rho(1450)}$	–	–	–	–	–	1	-0.66
γ	–	–	–	–	–	–	1

16.4 Combined fit to τ and e^+e^- data

It is interesting to perform a combined fit using τ (ALEPH and CLEO) and e^+e^- data in order to better constrain the lesser known parameters in the phenomenological form factor. For this study, the τ spectral function is duly corrected for the isospin-breaking effects identified in Section 16.1. Also photon vacuum polarization contributions are removed in the e^+e^- spectral function since they are absent in the τ data. In this way, the mass and width of the dominant $\rho(770)$ resonance in the two isospin states can be determined. For the sub-leading amplitudes from the higher vector mesons, isospin symmetry is assumed and therefore common masses and widths are used in the fit.

The result of the combined fit is given in Table 21. The differences between the masses and widths of the charged and neutral $\rho(770)$'s can be extracted to yield

$$m_{\rho^-} - m_{\rho^0} \quad = \quad (2.4 \pm 0.8) \text{ MeV} \tag{62}$$
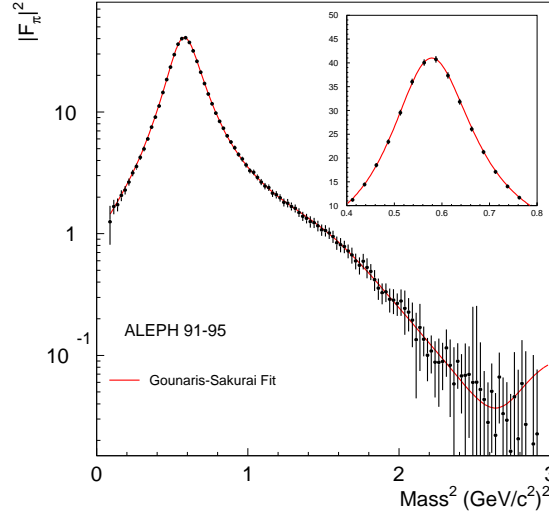
Figure 71: Fit of the ALEPH $\pi^- \pi^0$ form factor squared using the Gounaris-Sakurai parametrization.

$$\Gamma_{\rho^-} - \Gamma_{\rho^0} \quad = \quad (0.2 \pm 1.0) \text{ MeV} \tag{63}$$

The mass splitting is somewhat larger than the theoretical prediction (< 0.7 MeV) [75], but only at the 2σ level. The expected width splitting, from known isospin breaking, but not taking into account any ρ mass splitting, is (0.7 ± 0.3) MeV [24, 57]. However, if the mass difference is taken as an experimental fact, then a larger width difference would be expected. From the chiral model of the ρ resonance [86, 24], one expects

$$\Gamma_{\rho^0} \quad = \quad \Gamma_{\rho^-} \left(\frac{m_{\rho^0}}{m_{\rho^-}} \right)^3 \left(\frac{\beta_0}{\beta_-} \right)^3 \quad + \quad \Delta\Gamma_{EM} \tag{64}$$

where $\Delta\Gamma_{EM}$ is the width difference from electromagnetic decays (as discussed above), leading to a total width difference of (2.1 ± 0.5) MeV, marginally consistent with the observed value.

Mass splitting for the ρ was in fact considered in our previous analysis [3]. Using pre-CMD-2 e^+e^- data, a combined fit was attempted which produced a mass splitting consitent with 0 within an uncertainty of 1.1 MeV. However, the form factor from e^+e^- data still contained the vacuum polarization contribution (producing a 1.1 MeV shift) and a normalization problem was discovered in the treatment of the τ data in the combined fit. With the advent of precise CMD-2 data [59], it became apparent that differences were showing up between τ and e^+e^- form factors. A large part of the discrepancy was removed when CMD-2 re-analysed their data [60]. Since the τ results from ALEPH, CLEO and OPAL have been shown to be consistent, and since the recent results from the radiative return analysis of KLOE [82] are in fair agreement with the corrected CMD-2 results, the question of the ρ mass splitting is now more relevant. However a combined fit as shown in Table 22 using the τ data on one side and the e^+e^- data on

Table 21: Combined fit to the pion form factor-squared to ALEPH, CLEO τ and all e^+e^- data, where vacuum polarization has been excluded in the latter data. The parametrization of the $\rho(770)$, $\rho(1450)$, $\rho(1700)$ line shapes follows the Gounaris-Sakurai formula. Separate masses and widths are fitted for the $\rho(770)$, while common values are kept for the higher vector mesons. All mass and width values are in units of MeV and the phases are in degrees.

	τ and e^+e^-
$m_{\rho^-(770)}$	775.5 ± 0.6
$m_{\rho^0(770)}$	773.1 ± 0.5
$\Gamma_{\rho^-(770)}$	148.2 ± 0.8
$\Gamma_{\rho^0(770)}$	148.0 ± 0.9
$\alpha_{\rho\omega}$	$(2.03 \pm 0.10)\ 10^{-3}$
ϕ_α	(13.0 ± 2.3)
β	0.166 ± 0.005
ϕ_β	177.8 ± 5.2
$m_{\rho(1450)}$	1409 ± 12
$\Gamma_{\rho(1450)}$	501 ± 37
γ	0.071 ± 0.006
ϕ_γ	$[0]$
$m_{\rho(1700)}$	1740 ± 20
$\Gamma_{\rho(1700)}$	$[235]$
χ^2/DF	$383/326$

the other, and requiring for consistency the constraint from Eq. (64) has a χ^2 probability of only 0.6%. In fact, correcting for different masses extracted from the fit and using the corresponding constrained widths, improves the agreement between the τ and e^+e^- line shapes, but at the expense of a significant discrepancy in normalization. It should be noted that an additional correction for this apparent ρ mass splitting increases the present discrepancy for the muon anomalous magnetic moment between the estimates based on τ and e^+e^- spectral functions [87]. Looking back at the detailed comparison between spectral functions in Fig. 67, it is seen that the new KLOE data shows a trend below and above the ρ resonance which is not in good agreement with CMD-2 (and even worse with τ data). This behaviour prevents one at the moment from attributing the e^+e^--τ difference to a simple isospin-breaking correction resulting from different ρ masses and widths. The origin of the discrepancy thus remains ununderstood.

17 QCD analysis of τ spectral functions

The measurement of $\alpha_s(m_\tau^2)$ presented in this section is an update with the full τ sample of the analysis published in Ref. [12]. The method is based on a simultaneous fit of QCD parametrizations including perturbative and nonperturbative components to the

Table 22: Combined fit to the pion form factor squared to ALEPH, CLEO τ and e^+e^- data, where vacuum polarization has been excluded for the latter data. The parametrization of the $\rho(770)$, $\rho(1450)$, $\rho(1700)$ line shapes follows the Gounaris-Sakurai formula. For the $\rho(770)$, only m_{ρ^-}, m_{ρ^0}, and Γ_{ρ^-} are fitted, while Γ_{ρ^0} is computed from Eq. (64). All mass and width values are in units of MeV and the phases are in degrees. The parameters related to $\rho(1450)$ and $\rho(1700)$ amplitudes are fitted, assuming they are identical in both data sets.

	τ and e^+e^-
$m_{\rho^-(770)}$	775.4 ± 0.6
$m_{\rho^0(770)}$	773.1 ± 0.5
$\Gamma_{\rho^-(770)}$	148.8 ± 0.8
$\Gamma_{\rho^0(770)}$	(146.7)
$\alpha_{\rho\omega}$	$(2.02 \pm 0.10)\ 10^{-3}$
ϕ_α	(15.3 ± 2.0)
β	0.167 ± 0.006
ϕ_β	177.5 ± 6.0
$m_{\rho(1450)}$	1410 ± 16
$\Gamma_{\rho(1450)}$	505 ± 53
γ	0.071 ± 0.007
ϕ_γ	$[0]$
$m_{\rho(1700)}$	1748 ± 21
$\Gamma_{\rho(1700)}$	$[235]$
χ^2/DF	$390/327$

measured ratio R_τ

$$R_\tau = \frac{\Gamma(\tau^- \to \text{hadrons}^- \nu_\tau)}{\Gamma(\tau^- \to e^- \bar{\nu}_e \nu_\tau)} \ , \tag{65}$$

and to the spectral moments defined below (Section 17.2). It was proposed by Le Diberder and Pich [88] and has been employed in previous analyses by the ALEPH [10, 12], CLEO [89] and OPAL [70] Collaborations.

17.1 Theoretical prediction

According to Eq. (47) the absorptive parts of the vector and axial-vector two-point correlation functions $\Pi_{\bar{u}d,V/A}^{(J)}(s)$, with the spin J of the hadronic system, are proportional to the τ hadronic spectral functions with corresponding quantum numbers. The non-strange ratio R_τ can be written as an integral of these spectral functions over the invariant mass-squared s of the final state hadrons [67]:

$$R_\tau = 12\pi S_{\text{EW}} \int\limits_0^{m_\tau^2} \frac{ds}{m_\tau^2} \left(1 - \frac{s}{m_\tau^2}\right)^2 \left[\left(1 + 2\frac{s}{m_\tau^2}\right) \text{Im}\Pi^{(1)}(s + i\epsilon) + \text{Im}\Pi^{(0)}(s + i\epsilon)\right] \ , \tag{66}$$

where $\Pi^{(J)}$ can be decomposed as $\Pi^{(J)} = |V_{ud}|^2 \left(\Pi_{ud,V}^{(J)} + \Pi_{ud,A}^{(J)}\right)$. The correlation function $\Pi^{(J)}$ is analytic in the complex s plane everywhere except on the positive real axis where singularities exist. Hence by Cauchy's theorem, the imaginary part of $\Pi^{(J)}$ is proportional to the discontinuity across the positive real axis.

The energy scale $s_0 = m_\tau^2$ is large enough that contributions from nonperturbative effects are small. It is therefore assumed that one can use the Operator Product Expansion (OPE) to organize perturbative and nonperturbative contributions to $R_\tau(s_0)$. The factor $(1 - s/m_\tau^2)^2$ suppresses the contribution from the region near the positive real axis where $\Pi^{(J)}(s)$ has a branch cut and the OPE validity is restricted [90].

The theoretical prediction of the vector and axial-vector ratio $R_{\tau,V/A}$ can thus be written as:

$$R_{\tau,V/A} = \frac{3}{2}|V_{ud}|^2 S_{\text{EW}} \left(1 + \delta^{(0)} + \delta_{\text{EW}}' + \delta_{ud,V/A}^{(2-\text{mass})} + \sum_{D=4,6,\ldots} \delta_{ud,V/A}^{(D)}\right) \ , \tag{67}$$

with the residual non-logarithmic electroweak correction $\delta_{\text{EW}}' = 0.0010$ [73], neglected in the following, and the dimension $D = 2$ contribution $\delta_{ud,V/A}^{(2-\text{mass})}$ from quark masses which is lower than 0.1% for u, d quarks. The term $\delta^{(0)}$ is the massless perturbative contribution, while the $\delta^{(D)}$ are the OPE terms in powers of m_τ^{-D}:

$$\delta_{ud,V/A}^{(D)} = \sum_{\dim\mathcal{O}=D} C_{ud,V/A}(s,\mu) \frac{\langle\mathcal{O}_{ud}(\mu)\rangle_{V/A}}{(-m_\tau)^D} \ , \tag{68}$$

where the parameter μ separates the long-distance nonperturbative effects, absorbed into the vacuum expectation elements $\langle\mathcal{O}_{ud}(\mu)\rangle$, from the short-distance effects which are included in the Wilson coefficients $C_{ud,V/A}(s,\mu)$ [91].

The perturbative prediction adopted in this analysis follows in detail Ref. [92]. The perturbative contribution is given in the chiral limit. Effects from quark masses have been calculated in Ref. [93] and are found to be well below 1% for the light quarks. Thus the contributions from vector and axial-vector currents coincide to any given order of perturbation theory and the results are flavour independent.

The perturbative contribution in Eq. (67) is then given by [92]

$$1 + \delta^{(0)} = \sum_{n=0}^{3} K_n A^{(n)}(\alpha_s) , \tag{69}$$

with $K_0 = K_1 = 1$, $K_2 = 1.63982$ and $K_3 = 6.37101$ for three active flavours in the $\overline{\text{MS}}$ scheme [71]. The coefficients K_n are known up to three-loop order α_s^3 and for $n \geq 2$ they depend on the renormalization scheme employed. Although progress was recently made in the evaluation of some contributions at the four-loop order [94], the full calculation of K_4 is not yet available. The functions $A^{(n)}(\alpha_s)$ in Eq. (69) are the contour integrals

$$A^{(n)}(\alpha_s) = \frac{1}{2\pi i} \oint_{|s|=m_\tau^2} \frac{ds}{s} \left[1 - 2\frac{s}{m_\tau^2} + 2\left(\frac{s}{m_\tau^2}\right)^3 - \left(\frac{s}{m_\tau^2}\right)^4 \right] \left(\frac{\alpha_s(-s)}{\pi}\right)^n , \tag{70}$$

where the contour runs counter clockwise around the circle from $m_\tau^2 + i\epsilon$ to $m_\tau^2 - i\epsilon$. The strong coupling constant in the vicinity of m_τ^2 can be expanded in powers of $\alpha_s(s_0)$, with coefficients that are polynomials in $\ln(s/m_\tau^2)$ [67]. The perturbative prediction becomes then a function of the K_n coefficients and elementary integrals. Up to fourth order the fixed-order perturbation theory (FOPT) expansion reads

$$
\begin{aligned}
1 + \delta^{(0)} = {} & 1 + \frac{\alpha_s(m_\tau^2)}{\pi} + 5.2023 \left(\frac{\alpha_s(m_\tau^2)}{\pi}\right)^2 + 26.366 \left(\frac{\alpha_s(m_\tau^2)}{\pi}\right)^3 \\
& + (K_4 + 78.00) \left(\frac{\alpha_s(m_\tau^2)}{\pi}\right)^4 ,
\end{aligned} \tag{71}
$$

with the unknown K_4 coefficient.

Another approach to the solution of the contour integral (70) is to perform a direct numerical evaluation using the solution of the renormalization group equation (RGE) to four loops [98] as input for the running $\alpha_s(-s)$ [99, 92]. It implicitly provides a resummation of all known higher order logarithmic integrals and improves the convergence of the perturbative series. While, for instance, the third order term in the expansion (71) contributes with 17% to the total (truncated) perturbative prediction, the corresponding term of the numerical solution amounts only to 6.6% (assuming $\alpha_s(m_\tau^2) = 0.35$). This numerical solution of Eq. (69) will be referred as *contour-improved* fixed-order perturbation theory (FOPT$_{\text{CI}}$) in the following.

Despite a number of arguments expressed in Ref. [92], the intrinsic ambiguity between FOPT and FOPT$_{\text{CI}}$ is unresolvable at present. This is due to the truncation of the perturbative approximation of $\delta^{(0)}$ at finite order in α_s. A conservative measure of this

ambiguity is obtained from the deviation in R_τ found when cutting all additional orders in α_s (which is FOPT) and keeping them (FOPT$_{\mathrm{CI}}$), respectively. Both methods are likewise considered in this analysis.

The leading $D = 2$ corrections induced by the light-quark masses are computed using the running quark masses evaluated at the two-loop level. The following values are used for the renormalization-invariant quark mass parameters $\hat{m}_i$ defined in Ref. [67]:

$$\hat{m}_u = (8.7 \pm 1.5)\ \mathrm{MeV}\ , \quad \hat{m}_d = (15.4 \pm 1.5)\ \mathrm{MeV}\ , \quad \hat{m}_s = (270 \pm 30)\ \mathrm{MeV}\ . \tag{72}$$

The dimension $D = 4$ operators have dynamical contributions from the gluon condensate $\langle (\alpha_s/\pi) GG \rangle$ and quark condensates $m_u \langle 0|\bar{u}u|0 \rangle$, $m_d \langle 0|\bar{d}d|0 \rangle$ of the light u, d quarks. The contribution of the gluon condensate to $R_{\tau, V/A}$ vanishes in first order in $\alpha_s(m_\tau^2)$. However, there appear second order terms in the Wilson coefficients due to the logarithmic s dependence of $\alpha_s(s)$ which after performing the integral (66) becomes $\alpha_s^2(m_\tau^2)$. The quark condensates are parametrized [67] by $\langle m_j \bar{\psi}_i \psi_i \rangle = -\hat{m}_j \hat{\mu}_i^3$ with

$$\hat{\mu}_u = \hat{\mu}_d = (189 \pm 7)\ \mathrm{MeV}\ , \quad \hat{\mu}_s = (160 \pm 10)\ \mathrm{MeV}\ . \tag{73}$$

The contributions from dimension $D = 6$ and 8 operators are rather complex. They are treated phenomenologically in this analysis. Higher order contributions from $D \geq 10$ operators are expected to be small as, equivalent to the gluon condensate, constant terms and terms in leading order α_s vanish in Eq. (66) after integration.

The formulae are taken entirely from Ref. [67], in which Eq. (66) is evaluated after the power terms (68) are inserted into the integral.

17.2 Spectral moments

It was shown in Ref. [88] that it is possible to benefit from the information provided by the explicit shape of the spectral functions in order to obtain additional constraints on $\alpha_s(s_0)$ and — more importantly — on the nonperturbative condensates. The spectral moments at m_τ^2 are defined as:

$$R_{\tau, V/A}^{kl} \equiv \int_0^{m_\tau^2} ds \left(1 - \frac{s}{m_\tau^2} \right)^k \left(\frac{s}{m_\tau^2} \right)^l \frac{dR_{\tau, V/A}}{ds}\ , \tag{74}$$

with $R_{\tau, V/A}^{00} = R_{\tau, V/A}$. The factor $(1 - s/m_\tau^2)^k$ suppresses the integrand at the crossing of the positive real axis where the validity of the OPE is less certain and the experimental accuracy is statistically limited. Its counterpart $(s/m_\tau^2)^l$ projects out higher energies. The spectral information is used to fit simultaneously $\alpha_s(m_\tau^2)$ and the phenomenological effective operators $\langle (\alpha_s/\pi) GG_{D=4} \rangle$, $\langle \mathcal{O}_{D=6} \rangle$ and $\langle \mathcal{O}_{D=8} \rangle$. Due to the intrinsic strong correlations only five moments are used as input to the fit.

In analogy to R_τ, the contributions to the moments originating from perturbative

and nonperturbative QCD are separated via the OPE. The prediction of the perturbative contribution takes the form

$$\delta^{(0,kl)} = \sum_{n=1}^{3} K_n A^{(n,kl)}(\alpha_s) \, , \tag{75}$$

with contour integrals $A^{(n,kl)}(\alpha_s)$ [88] that are expanded up to $\alpha_s^3(s)$ (FOPT) or numerically resolved for the running $\alpha_s(-s)$ obtained from the RGE (FOPT$_{\mathrm{CI}}$).

For practical purpose it is more convenient to define moments that are normalized to the corresponding $R_{\tau,V/A}$ in order to decouple the normalization from the shape of the τ spectral functions:

$$D_{\tau,V/A}^{kl} \equiv \frac{R_{\tau,V/A}^{kl}}{R_{\tau,V/A}} = \int_0^{m_\tau^2} ds \left(1 - \frac{s}{m_\tau^2}\right)^k \left(\frac{s}{m_\tau^2}\right)^l \frac{1}{N_{V/A}} \frac{dN_{V/A}}{ds} \, . \tag{76}$$

The two sets of experimentally almost uncorrelated observables — $R_{\tau,V/A}$ on one hand and the spectral moments on the other hand— yield independent constraints on $\alpha_s(m_\tau^2)$ and thus provide an important test of consistency.

The results given in Section 14.5 are recalled:

$$R_{\tau,V} = 1.787 \pm 0.013 \, , \tag{77}$$
$$R_{\tau,A} = 1.695 \pm 0.013 \, , \tag{78}$$
$$R_{\tau,V+A} = 3.482 \pm 0.014 \, . \tag{79}$$

The normalization according to Eq. (76) reduces considerably the correlations between R_τ and the moments. It is completely negligible in the $(V + A)$ case where $R_{\tau,V+A}$ is calculated from the difference $R_\tau - R_{\tau,S}$, which has no correlation with the hadronic invariant mass spectrum.

The measured values of the moments for the V, A and $(V + A)$ spectral functions are given in Table 23, and their correlation matrices in Table 24. The correlations between the moments are computed analytically from the contraction of the derivatives of two involved moments with the covariance matrices of the respective normalized invariant mass-squared spectra. In all cases, the negative sign for the correlations between the $k = 1, l = 0$ and the $k = 1, l \geq 1$ moments is understood to be due to the ρ and the π, a_1 peaks which determine the major part of the $k = 1, l = 0$ moments. They are much less important for higher moments and consequently the amount of negative correlation increases with $l = 1, 2, 3$. This also explains the large and increasing positive correlations between the $k = 1, l \geq 1$ moments, in which, with growing l, the high energy tail becomes more important than the low energy peaks. The total errors for the $(V + A)$ case are dominated by the uncertainties on the hadronic fractions.

17.3   Results of the fits: $\alpha_s(m_\tau^2)$

The combined fits to the measured V, A and $(V + A)$ ratios R_τ and moments adjust the parameters $\alpha_s(m_\tau^2)$, $\langle (\alpha_s/\pi)GG \rangle$, $\langle \mathcal{O}_6 \rangle_{V/A}$ and $\langle \mathcal{O}_8 \rangle_{V/A}$ of the OPE in the theoretical

Table 23: Spectral Moments of vector (V), axial-vector (A) and vector plus axial-vector $(V+A)$ inclusive τ decays. The errors give the total experimental uncertainties including statistical and systematic effects.

ALEPH	$l=0$	$l=1$	$l=2$	$l=3$
D_V^{1l}	0.7160	0.1694	0.0533	0.0227
$\Delta^{\exp} D_V^{1l}$	0.0025	0.0004	0.0006	0.0004
D_A^{1l}	0.7107	0.1489	0.0657	0.0317
$\Delta^{\exp} D_A^{1l}$	0.0018	0.0006	0.0004	0.0003
D_{V+A}^{1l}	0.7134	0.1595	0.0594	0.0271
$\Delta^{\exp} D_{V+A}^{1l}$	0.0016	0.0004	0.0003	0.0003

Table 24: Experimental correlations between the moments $D_{\tau,V/A/V+A}^{kl}$. There are no correlations between $R_{\tau,V+A}$ and the corresponding moments.

ALEPH	$D_{\tau,V}^{10}$	$D_{\tau,V}^{11}$	$D_{\tau,V}^{12}$	$D_{\tau,V}^{13}$	ALEPH	$D_{\tau,A}^{10}$	$D_{\tau,A}^{11}$	$D_{\tau,A}^{12}$	$D_{\tau,A}^{13}$
$R_{\tau,V}$	-0.34	0.20	0.33	0.35	$R_{\tau,A}$	-0.23	0.02	0.16	0.25
$D_{\tau,V}^{10}$	1	-0.82	-0.98	-0.99	$D_{\tau,A}^{10}$	1	-0.78	-0.97	-0.98
$D_{\tau,V}^{11}$	$-$	1	0.90	0.82	$D_{\tau,A}^{11}$	$-$	1	0.87	0.66
$D_{\tau,V}^{12}$	$-$	$-$	1	0.99	$D_{\tau,A}^{12}$	$-$	$-$	1	0.94
$D_{\tau,V}^{13}$	$-$	$-$	$-$	1	$D_{\tau,A}^{13}$	$-$	$-$	$-$	1

ALEPH	$D_{\tau,V+A}^{10}$	$D_{\tau,V+A}^{11}$	$D_{\tau,V+A}^{12}$	$D_{\tau,V+A}^{13}$
$D_{\tau,V+A}^{10}$	1	-0.73	-0.98	-0.99
$D_{\tau,V+A}^{11}$	$-$	1	0.80	0.67
$D_{\tau,V+A}^{12}$	$-$	$-$	1	0.98
$D_{\tau,V+A}^{13}$	$-$	$-$	$-$	1

predictions (67) and (74) of the above quantities.

The uncertainties entering the theoretical predictions have been estimated in great detail in the previous analysis [12]. Minor contributions originate from the CKM matrix element $|V_{ud}|$, the electroweak radiative correction factor S_{EW}, the light quark masses $m_{u,d}$, and the quark condensates. The largest contributions have their origin in the truncation of the perturbative expansion. Although it might introduce double-counting, the procedure used considers separate variations of the unknown higher order coefficient K_4 and the choice of the renormalization scale. Thus the estimate is expected to be conservative. The renormalization scale is varied around m_τ from 1.1 to 2.3 GeV with the variation over half of the range taken as systematic uncertainty. Concerning the coefficient K_4, some theoretical progress has been achieved for its direct calculation. Part of the contributions have been recently calculated [94], lending support to the estimate

$(K_4 \sim 27.5)$ using the principle of minimal sensitivity [95], which allows the computation of a renormalization scheme with optimal convergence [96]. Another estimate of K_4 was obtained [97] using the a priori freedom of the choice of the renormalization scale μ to increase the sensitivity of the perturbative series on K_4, yielding $K_4 = 27 \pm 5$. Taking advantage of the new theoretical developments, the value $K_4 = 25 \pm 25$ is assumed in this analysis, instead of 50 ± 50 used in the previous analysis [12].

The fit minimizes the χ^2 of the differences between measured and fitted quantities contracted with the inverse of the sum of the experimental and theoretical covariance matrices.

The results are listed in Table 25, separately for the FOPT and FOPT$_{\mathrm{CI}}$ approaches. It is to be noted that even if the fits are better with the FOPT expansion, the two sets of results are considered on the same footing and averaged later on. Table 26 gives the corresponding correlation matrices between the fitted parameters. The limited number of observables and the strong correlations between the spectral moments explain the large correlations observed, especially between the fitted nonperturbative operators. The precision of $\alpha_s(m_\tau^2)$ obtained with the two perturbative methods employed is comparable, however their central values differ by 0.01-0.02. The $\delta^{(2)}$ term is the pure theoretical contribution from the known masses (within errors) of the light u, d quarks. In the $\delta^{(4)}$ term the quark condensates and the quark masses are rather well known and are fixed theoretically within their errors, while the gluon condensate is adjusted in the fit.

As mentioned before, there exists no constraining prescription which allows a resolution of the ambiguity between FOPT$_{\mathrm{CI}}$ and FOPT. The final result on $\alpha_s(m_\tau^2)$ is thus taken as the arithmetic average of the two values given in Table 25, with half of their difference added as additional theoretical error:

$$\alpha_s(m_\tau^2) = 0.340 \pm 0.005_{\mathrm{exp}} \pm 0.014_{\mathrm{th}} . \tag{80}$$

The first error accounts for the experimental uncertainty, the second number gives the uncertainty of the theoretical prediction of R_τ and the spectral moments as well as the ambiguity of the theoretical approaches employed.

In Table 25, a remarkable agreement within statistical errors is found between the $\alpha_s(m_\tau^2)$ values using vector and axial-vector data, providing a first important consistency check of the analysis, since the two corresponding spectral functions are independently measured and manifest a quite different resonant behaviour. The main results are displayed in Fig. 72.

17.4   Results of the fits: nonperturbative contributions

The advantage of separating the vector and axial-vector channels and comparing to the inclusive $(V + A)$ fit becomes obvious in the adjustment of the leading nonperturbative contributions of dimension $D = 6$ and $D = 8$, which approximately cancel in the inclusive sum. This cancellation of the nonperturbative terms increases the confidence in the $\alpha_s(m_\tau^2)$ determination from the inclusive $(V + A)$ observables. The gluon condensate is

Table 25: Fit results of $\alpha_s(m_\tau^2)$ and the OPE nonperturbative contributions from vector, axial-vector and $(V+A)$ combined fits using the corresponding ratios R_τ and the spectral moments as input parameters. Where two errors are given they denote experimental (first number) and theoretical uncertainties (second number). The $\delta^{(2)}$ term is the pure theoretical prediction with quark masses varying within their prescribed range (see text). The quark condensates in the $\delta^{(4)}$ term are fixed to their theoretical values [12] within errors and only the gluon condensate is varied as a free parameter. The total nonperturbative contribution is the sum $\delta_{\mathrm{NP}} = \delta^{(4)} + \delta^{(6)} + \delta^{(8)}$. Results are given separately for the FOPT$_{\mathrm{CI}}$ and the FOPT perturbative expansion (see text).

fitted variable	Vector (V)	Axial-Vector (A)	$V + A$
$\alpha_s(m_\tau^2)$ (FOPT$_{\mathrm{CI}}$)	$0.355 \pm 0.008 \pm 0.009$	$0.333 \pm 0.009 \pm 0.009$	$0.350 \pm 0.005 \pm 0.009$
$\alpha_s(m_\tau^2)$ (FOPT)	$0.331 \pm 0.006 \pm 0.012$	$0.327 \pm 0.007 \pm 0.012$	$0.331 \pm 0.004 \pm 0.012$
$\langle \frac{\alpha_s}{\pi} GG \rangle$ (GeV^4) (FOPT$_{\mathrm{CI}}$)	$(0.4 \pm 0.3) \times 10^{-2}$	$(-1.3 \pm 0.4) \times 10^{-2}$	$(-0.5 \pm 0.3) \times 10^{-2}$
$\langle \frac{\alpha_s}{\pi} GG \rangle$ (GeV^4) (FOPT)	$(1.5 \pm 0.3) \times 10^{-2}$	$(-0.2 \pm 0.4) \times 10^{-2}$	$(0.6 \pm 0.2) \times 10^{-2}$
$\delta^{(6)}$ (FOPT$_{\mathrm{CI}}$)	$(2.85 \pm 0.22) \times 10^{-2}$	$(-3.23 \pm 0.26) \times 10^{-2}$	$(-2.1 \pm 2.2) \times 10^{-3}$
$\delta^{(6)}$ (FOPT)	$(2.70 \pm 0.25) \times 10^{-2}$	$(-2.96 \pm 0.31) \times 10^{-2}$	$(-1.6 \pm 2.5) \times 10^{-3}$
$\delta^{(8)}$ (FOPT$_{\mathrm{CI}}$)	$(-9.0 \pm 0.5) \times 10^{-3}$	$(8.9 \pm 0.6) \times 10^{-3}$	$(-0.3 \pm 4.8) \times 10^{-4}$
$\delta^{(8)}$ (FOPT)	$(-8.6 \pm 0.6) \times 10^{-3}$	$(8.6 \pm 0.6) \times 10^{-3}$	$(1.2 \pm 5.2) \times 10^{-4}$
$\chi^2/1$ DF (FOPT$_{\mathrm{CI}}$)	0.52	5.71	3.84
$\chi^2/1$ DF (FOPT)	0.01	0.63	0.11
$\delta^{(2)}$ (FOPT$_{\mathrm{CI}}$)	$(-3.3 \pm 3.0) \times 10^{-4}$	$(-5.1 \pm 3.0) \times 10^{-4}$	$(-4.4 \pm 2.0) \times 10^{-4}$
$\delta^{(2)}$ (FOPT)	$(-3.0 \pm 3.0) \times 10^{-4}$	$(-5.0 \pm 3.0) \times 10^{-4}$	$(-4.0 \pm 2.0) \times 10^{-4}$
$\delta^{(4)}$ (FOPT$_{\mathrm{CI}}$)	$(4.1 \pm 1.2) \times 10^{-4}$	$(-5.7 \pm 0.1) \times 10^{-3}$	$(-2.7 \pm 0.1) \times 10^{-3}$
$\delta^{(4)}$ (FOPT)	$(6.8 \pm 1.0) \times 10^{-4}$	$(-5.3 \pm 0.1) \times 10^{-3}$	$(-2.4 \pm 0.1) \times 10^{-3}$
Total δ_{NP} (FOPT$_{\mathrm{CI}}$)	$(1.99 \pm 0.27) \times 10^{-2}$	$(-2.91 \pm 0.20) \times 10^{-2}$	$(-4.8 \pm 1.7) \times 10^{-3}$
Total δ_{NP} (FOPT)	$(1.91 \pm 0.31) \times 10^{-2}$	$(-2.63 \pm 0.25) \times 10^{-2}$	$(-3.9 \pm 2.0) \times 10^{-3}$

Table 26: Correlation matrices according to the fits presented in Table 25 for vector (left table), axial-vector (middle) and $(V + A)$ (right table) using FOPT$_{\mathrm{CI}}$. As the gluon condensate contributes only insignificantly to $\delta^{(4)}$, the correlations to the total $\delta^{(4)}$ term are small.

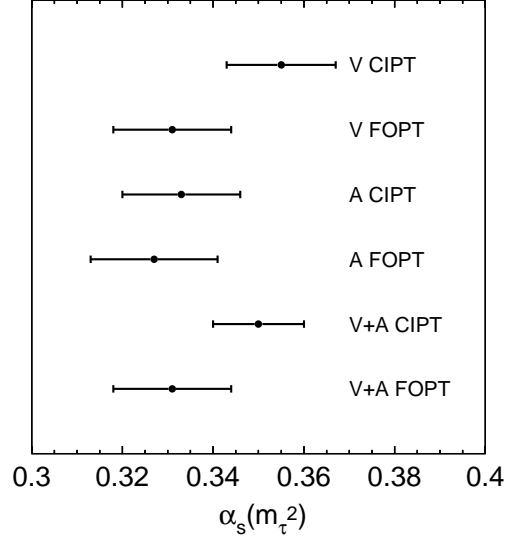| ALEPH	$\langle GG \rangle_V$	$\delta_V^{(6)}$	$\delta_V^{(8)}$	$\langle GG \rangle_A$	$\delta_A^{(6)}$	$\delta_A^{(8)}$	$\langle GG \rangle_{V+A}$	$\delta_{V+A}^{(6)}$	$\delta_{V+A}^{(8)}$
$\alpha_s(m_\tau^2)$	-0.39	-0.28	-0.34	-0.57	0.52	-0.55	-0.37	0.38	-0.45
$\langle GG \rangle_{V/A/V+A}$	1	0.44	0.46	1	-0.81	0.80	1	-0.65	0.65
$\delta_{V/A/V+A}^{(6)}$	–	1	-0.98	–	1	-0.99	–	1	-0.98
$\delta_{V/A/V+A}^{(8)}$	–	–	1	–	–	1	–	–	1

Figure 72: Results for $\alpha_s(m_\tau^2)$ from the fits of $R_{\tau,V,A,V+A}$ and the moments $D_{V,A,V+A}^{kl}$ using the $\mathrm{FOPT_{CI}}$ and FOPT perturbative expansions. The measurements are correlated due to the theoretical errors (see Table 25).

determined by the first $l = 0, 1$ moments, which receive lowest order contributions. It is observed that the values obtained in the V and A fits are not very consistent, which could indicate some problem in the validity of the OPE approach, since nonperturbative contributions are significant in these cases. Taking the value obtained in the $(V + A)$ inclusive fit, where nonperturbative effects are negligible, and adding as systematic uncertainties half of the difference between the vector and axial-vector fits as well as between the $\mathrm{FOPT_{CI}}$ and FOPT results, the gluon condensate is found to be

$$\langle(\alpha_s/\pi)GG\rangle = (0.001 \pm 0.012) \text{ GeV}^4. \tag{81}$$

This result does not provide evidence for a nonzero gluon condensate, but it is consistent with and has comparable accuracy to the independent value obtained using charmonium sum rules and e^+e^- data in the charm region, (0.011 ± 0.009) GeV^4 in a combined determination with the c quark mass [102].

The $D = 6, 8$ nonperturbative contributions are obtained after averaging the FOPT and $\mathrm{FOPT_{CI}}$ values:

$$\begin{aligned}
\delta_V^{(6)} &= (2.8 \pm 0.3) \times 10^{-2} , & \delta_V^{(8)} &= (-8.8 \pm 0.6) \times 10^{-3} , \\
\delta_A^{(6)} &= (-3.1 \pm 0.3) \times 10^{-2} , & \delta_A^{(8)} &= (8.7 \pm 0.6) \times 10^{-3} , \\
\delta_{V+A}^{(6)} &= (-1.8 \pm 2.4) \times 10^{-3} , & \delta_{V+A}^{(8)} &= (0.5 \pm 5.1) \times 10^{-4} .
\end{aligned} \tag{82}$$

The remarkable feature is the approximate cancellation of these contributions in the $V+A$ case, both for $D = 6$ and $D = 8$. This property was predicted [67] for $D = 6$ using the simplifying assumption of vacuum saturation for the matrix elements of four-quark
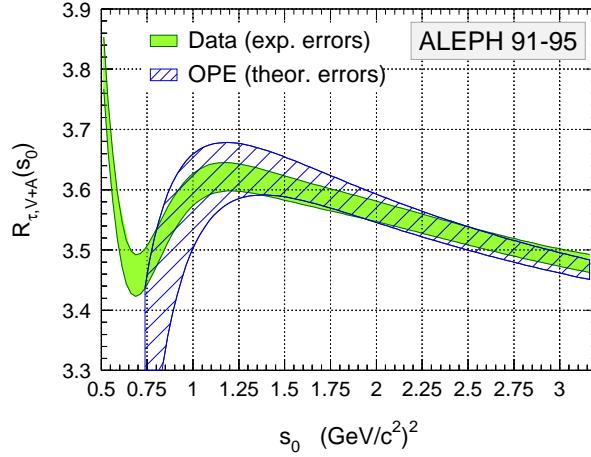
Figure 73: The ratio $R_{\tau,V+A}$ versus the square "τ mass" s_0. The curves are plotted as error bands to emphasize their strong point-to-point correlations in s_0. Also shown is the theoretical prediction using FOPT_{CI} and the results for $R_{\tau,V+A}$ and the nonperturbative terms from Table 25.

operators, yieding $\delta_V^{(6)} = -(7/11)\,\delta_A^{(6)}$ and $\delta_V^{(6)} = (2.5 \pm 1.3) \times 10^{-2}$, in fair agreement with our results. There is no reliable prediction for the $D = 8$ contributions.

The total nonperturbative $V + A$ correction is $\delta_{\text{NP},V+A} = (-4.3 \pm 1.9) \times 10^{-3}$, much smaller than the corresponding values in the V and A components, $\delta_{\text{NP},V} = (2.0 \pm 0.3) \times 10^{-2}$ and $\delta_{\text{NP},V} = (-2.8 \pm 0.3) \times 10^{-2}$. After removing the theoretically well-known contribution from the quark condensates ($D = 4$), the remaining non perturbative component in $V + A$ is $-(1.7 \pm 1.9) \times 10^{-3}$, one order of magnitude smaller compared to V and A, and even consistent with zero.

17.5 Evolution of α_s with the mass scale

17.5.1 Test of the running of $\alpha_s(s)$ at low energies

Using the spectral functions, one can simulate the physics of a hypothetical τ lepton with a mass $\sqrt{s_0}$ smaller than m_τ through Eq. (66). Assuming quark-hadron duality, the evolution of $R_\tau(s_0)$ provides a direct test of the running of $\alpha_s(s_0)$, governed by the RGE β-function. On the other hand, it is a test of the validity of the OPE approach in τ decays. The studies performed in this section employ only FOPT_{CI}. Results obtained with FOPT are similar and differ only in the central $\alpha_s(m_\tau^2)$ value.

The functional dependence of $R_{\tau,V+A}(s_0)$ is plotted in Fig. 73 together with the theoretical prediction using the results of Table 25. The slight mismatch appearing at $s_0 = m_\tau^2$ between the experimental and theoretical values of $R_{\tau,V+A}$ is due to the fact that the global fits presented in Table 25 involve not only the measured $R_{\tau,V+A}$, but also the spectral moments. The spread due to uncertainties are shown as bands. The correlations between two adjacent bins $s_1 < s_2$ are large as the only new information is provided
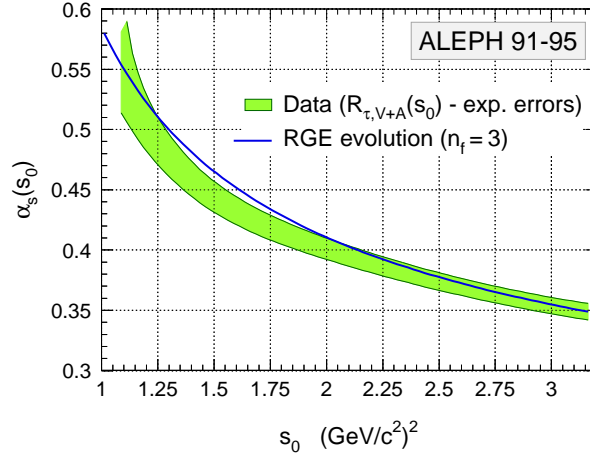
Figure 74: The running of $\alpha_s(s_0)$ obtained from the fit of the theoretical prediction to $R_{\tau,V+A}(s_0)$. The shaded band shows the data including experimental errors. The curve gives the four-loop RGE evolution for three flavours.

by the small mass difference between the two bins and the slightly different weight function. They are reinforced by the original experimental and theoretical correlations. Below 1 GeV^2 the error of the theoretical prediction of $R_{\tau,V+A}(s_0)$ starts to blow up due to the increasing uncertainty from the unknown K_4 perturbative term; errors of the nonperturbative contributions are *not* contained in the theoretical error band. Figure 74 shows the plot corresponding to Fig. 73, translated into the running of $\alpha_s(s_0)$, *i.e.*, the experimental value for $\alpha_s(s_0)$ has been individually determined at every s_0 from the comparison of data and theory. Also plotted is the four-loop RGE evolution using three quark flavours.

It is remarkable that the theoretical prediction using the parameters determined at the τ mass and $R_{\tau,V+A}(s_0)$ extracted from the measured $V+A$ spectral function agree down to $s_0 \sim 0.8$ GeV^2. The agreement is good to about 2% at 1 GeV^2. This result, even more directly illustrated by Fig. 74, demonstrates the validity of the perturbative approach down to masses around 1 GeV, well below the τ mass scale. The agreement with the expected scale evolution between 1 and 1.8 GeV is an interesting result, considering the relatively low mass range, where α_s is seen to decrease by a factor of 1.6 and reaches rather large values ~ 0.55 at the lowest masses. This behaviour provides confidence that the $\alpha_s(m_\tau^2)$ measurement is on solid phenomenological ground.

17.5.2   Evolution to M_Z

The evolution of the $\alpha_s(m_\tau^2)$ measurement from the inclusive $(V+A)$ observables to the Z mass scale can be performed, based on the Runge-Kutta integration of the differential equation to four loops and matching conditions at heavy quark (c, b) thresholds to three loops [98, 100, 101, 103, 104]. There is some ambiguity in the procedure followed to satisfy the matching conditions, in particular whether the matching should be performed

at a scale given by the quark mass or twice the quark mass, and also on the choice of quark mass, *i.e.* the running mass or the pole mass. Different procedures have been tried with the relevant parameters varied within their uncertainties. The results are consistent within the quoted systematic uncertainty and for definiteness the final value is obtained with the matching realized at the quark-pair thresholds:

$$\begin{aligned} \alpha_s(M_Z^2) &= 0.1209 \pm 0.0006_{\text{exp}} \pm 0.0016_{\text{th}} \pm 0.0005_{\text{evol}} \\ &= 0.1209 \pm 0.0018 \ . \end{aligned} \tag{83}$$

The first two errors originate from the $\alpha_s(m_\tau^2)$ determination given in Eq. (80), while the last error stands for possible ambiguities in the evolution due to uncertainties in the matching scales of the quark thresholds. The uncertainty on the evolution has main components from the c-quark mass (0.00020), the b-quark mass (0.00005), the renormalization scale (taken from 0.7 m_q to 3.0 m_q, 0.00023), the 3-loop truncation in the matching expansion (0.00026) and the four-loop truncation in the RGE equation (0.00031).

The result (83) is a 1.5% determination of the strong coupling constant at the M_Z scale, limited in accuracy by theoretical uncertainties in the perturbative expansion. The significant improvement in precision compared to our previous determination [12], $0.1202 \pm 0.008_{\text{exp}} \pm 0.0024_{\text{th}} \pm 0.0010_{\text{evol}}$, results from the higher statistics and the more detailed experimental analysis, but mostly from the increased knowledge from theory, essentially at the level of the perturbative expansion [94], and also for the scale evolution procedure.

The $\alpha_s(M_Z^2)$ result from the present analysis of τ decays is in agreement with the determination from the Z width as obtained by the global fit to all electroweak data [105]:

$$\alpha_s(M_Z^2)_{\text{Z width}} = 0.1186 \pm 0.0027 \ , \tag{84}$$

as demonstrated in Fig. 75. Both determinations have somewhat comparable accuracies, which are however very different in nature. On one hand, the τ value is dominated by theoretical uncertainties. On the other hand, the determination at the Z resonance, benefiting from the much larger energy scale and the correspondingly small uncertainties from the truncated perturbative expansion, is limited by the experimental precision on the electroweak observables, essentially the ratio of leptonic to hadronic peak cross sections. The consistency between the two results, Eqs. (83) and (84), provides a powerful test, over a range of s spanning more than three orders of magnitude, of the evolution of the strong interaction coupling as predicted by the nonabelian nature of the QCD gauge theory. It is therefore a precise test of asymptotic freedom at the 2.7% level.

18   Conclusions

A final analysis of τ decay branching fractions has been presented using all LEP 1 data collected with the ALEPH detector. As in the publication based on the 1991-1993 data set,
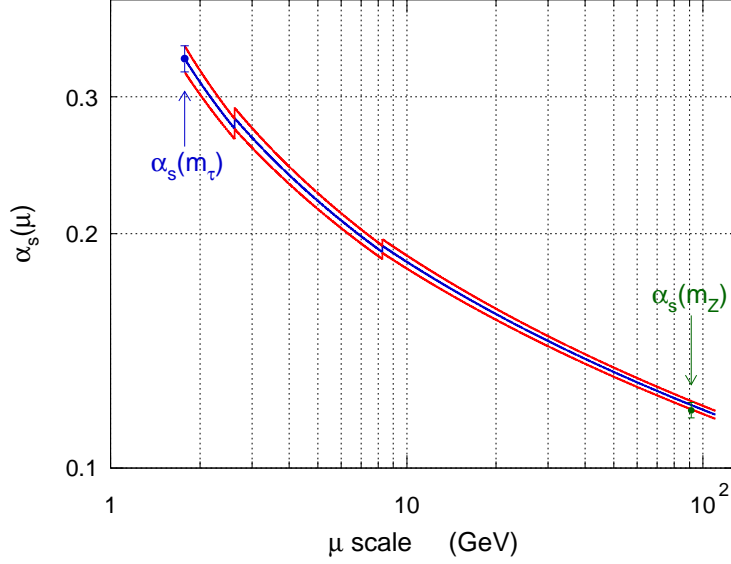
Figure 75: The evolution of the measured $\alpha_s(m_\tau^2)$ to higher scales μ using the 4-loop RGE and the 3-loop matching conditions applied at the heavy quark-pair thresholds (hence the discontinuities at $2\,m_c$ and $2\,m_b$). The evolution of the ALEPH $\alpha_s(m_\tau^2)$ determination is in agreement with the direct value obtained from the Z width through the global electroweak fit [105].

it uses a global analysis of all modes, classified according to charged particle identification, and charged particle and π^0 multiplicity up to $4\,\pi^0$s in the final state. Major improvements are introduced with respect to the published analysis and a better understanding is achieved, in particular in the separation between genuine and fake photons. In this process shortcomings and small biases of the previous method were discovered and corrected, leading to more robust results. As modes with kaons ($K^\pm$, K_S^0, and K_L^0) have already been studied and published with the full statistics, the non-strange modes without kaons are emphasized in this paper. Taken together these results provide a complete description of τ decays up to 6 hadrons in the final state. All decay channels with branching fractions larger than 0.1% are considered in this analysis.

The measured branching fractions are internally consistent and agree with known constraints from other measurements in the framework of the Standard Model. More specifically, the results on the leptonic and pionic fractions lead to powerful tests of universality in the charged leptonic weak current, showing that the $e - \mu - \tau$ couplings are equal within 0.3%. The branching ratio of $\tau \to \nu_\tau \pi \pi^0$, which is of particular interest to the accurate determination of vacuum polarization effects, is determined with a precision of 0.5% to be (25.47 ± 0.13) %. Also the ratio of a_1 branching fractions into $\pi 2\pi^0$ and 3π final states is measured to be 0.979 ± 0.018, in agreement with expectation from partial wave analyses of these decays. Separating nonstrange hadronic channels into vector (V) and axial-vector (A) components and normalizing to the electronic width yields the ratios $R_{\tau,V} = 1.787 \pm 0.013$, $R_{\tau,A} = 1.695 \pm 0.013$, $R_{\tau,V+A} = 3.482 \pm 0.014$ and

$R_{\tau,V-A} = 0.092 \pm 0.023$.

Spectral functions for the hadronic modes are determined through the unfolding of the measured invariant mass distributions, taking into account detector effects. As for the branching fractions, the spectral functions are separated into vector and axial-vector contributions. The vector spectral functions are compared to the corresponding ones obtained through e^+e^- annihilation, providing accurate tests of isospin invariance of the electroweak current. Both spectral functions are fitted within QCD to perturbative and nonperturbative components. The latter are determined to be very small, while the dominant perturbative part yields a precise value for the strong coupling at the τ mass scale, $\alpha_s(m_\tau^2) = 0.340 \pm (0.005)_{exp} \pm (0.014)_{th}$. The evolution to the Z mass scale yields $\alpha_s(M_Z^2) = 0.1209 \pm 0.0018$. It agrees well with the direct determination from the Z width and provides the most accurate test to date of asymptotic freedom in the QCD gauge theory.

Acknowledgements

We wish to thank our colleagues from the accelerator divisions for the successful operation of LEP. We are indebted to the engineers and technicians in all our institutions for their contribution to the excellent performance of ALEPH. Those of us from non-member countries thank CERN for its hospitality. It is a pleasure to thank W. Marciano and A. Pich for clarifying many theoretical aspects.

References

[1] ALEPH Coll., *Z. Phys.* **C54** (1992) 211.

[2] ALEPH Coll., *Z. Phys.* **C70** (1996) 561.

[3] ALEPH Coll., *Z. Phys.* **C70** (1996) 579.

[4] ALEPH Coll., *Phys. Lett.* **B332** (1994) 209.

[5] ALEPH Coll., *Phys. Lett.* **B332** (1994) 219.

[6] ALEPH Coll., *Eur. Phys. J.* **C1** (1998) 65.

[7] ALEPH Coll., *Eur. Phys. J.* **C4** (1998) 29.

[8] ALEPH Coll., *Eur. Phys. J.* **C10** (1999) 1.

[9] ALEPH Coll., *Eur. Phys. J.* **C11** (1999) 599.

[10] ALEPH Coll., *Phys. Lett.* **B307** (1993) 209.

[11] ALEPH Coll., *Z. Phys.* **C76** (1997) 15.

[12] ALEPH Coll., *Eur. Phys. J.* **C4** (1998) 409.

[13] ALEPH Coll., *Z. Phys.* **C74** (1997) 263.

[14] ALEPH Coll., *Nucl. Inst. Meth.* **A294** (1990) 127.

[15] ALEPH Coll., *Nucl. Inst. Meth.* **A360** (1995) 481.

[16] ALEPH Coll., *Eur. Phys. J.* **C20** (2001) 401.

[17] S. Jadach, B.F.L. Ward, and Z. Was, *Comp. Phys. Comm.* **79** (1994) 503.

[18] S. Jadach *et al.*, *Comp. Phys. Comm.* **76** (1993) 361.

[19] ALEPH Coll., *Z. Phys.* **C62** (1994) 539.

[20] H. Anlauf *et al.*, *Comp. Phys. Comm.* **79** (1994) 466.

[21] T. Sjöstrand, *Comp. Phys. Comm.* **39** (1986) 347.

[22] E. Barberio, B. van Eijk and Z. Was, *Comp. Phys. Comm.* **66** (1991) 115;
E. Barberio and Z. Was, *Comp. Phys. Comm.* **79** (1994) 291.

[23] S. Snow, Proceedings of the 2nd International Workshop on τ Lepton Physics,
Columbus 1992, K. K. Gan ed., World Scientific (1993).

[24] V. Cirigliano, G. Ecker and H. Neufeld, *Phys. Lett.* **B513** (2001) 361; *JHEP* **0208**
(2002) 002.

[25] Review of Particle Physics, S. Eidelman *et al.*, *Phys. Lett.* **B592** (2004) 1.

[26] D. Bortoletto *et al.*, CLEO Coll., *Phys. Rev. Lett.* **71** (1993) 1791.

[27] T. Bergfeld *et al.*, CLEO Coll., *Phys. Rev. Lett.* **79** (1997) 2406; A. Weinstein,
Proceedings of the 6th International Workshop on τ Lepton Physics, Victoria 2000,
R. J. Sobie and J. M. Roney eds., North Holland (2001).

[28] M. Zielinski *et al.*, *Phys. Rev. Lett.* **52** (1984) 1195.

[29] A. Anastassov *et al.*, CLEO Coll., *Phys. Rev. Lett.* **86** (2001) 4467.

[30] H. Albrecht *et al.*, ARGUS Coll., *Phys. Lett.* **B316** (1993) 608.

[31] A. Anastassov *et al.*, CLEO Coll., *Phys. Rev.* **D55** (1997) 2559.

[32] P. Abreu *et al.*, DELPHI Coll., *Eur. Phys. J.* **C10** (1999) 201.

[33] G. Abbiendi *et al.*, OPAL Coll., *Phys. Lett.* **B447** (1999) 134.

[34] M. Acciarri *et al.*, L3 Coll., *Phys. Lett.* **B507** (2001) 47.

[35] G. Abbiendi *et al.*, OPAL Coll., *Phys. Lett.* **B551** (2003) 35.

[36] K. Ackerstaff *et al.*, OPAL Coll., *Eur. Phys. J.* **C4** (1998) 193.

[37] M. Artuso *et al.*, CLEO Coll., *Phys. Rev. Lett.* **72** (1994) 3762.

[38] M. Procario *et al.*, CLEO Coll., *Phys. Rev. Lett.* **70** (1993) 1207.

[39] R. Balest *et al.*, CLEO Coll., *Phys. Rev. Lett.* **75** (1995) 3809.

[40] R. Akers *et al.*, OPAL Coll., *Z. Phys.* **C68** (1995) 555.

[41] D. Bortoletto *et al.*, CLEO Coll., *Phys. Rev. Lett.* **71** (1993) 3762; A. Anastassov *et al.*, CLEO Coll., *Phys. Rev. Lett.* **86** (2001) 4467.

[42] B. Bylsma *et al.*, HRS Coll., *Phys. Rev.* **D35** (1987) 2269.

[43] H. Albrecht *et al.*, ARGUS Coll., *Phys. Lett.* **B202** (1988) 149.

[44] O. Gibaut *et al.*, CLEO Coll., *Phys. Rev. Lett.* **73** (1984) 934.

[45] K. Ackerstaff *et al.*, OPAL Coll., *Eur. Phys. J.* **C8** (1999) 183.

[46] B. Aubert *et al.*, BaBar Coll., hep-ex/0505004

[47] A. Anastassov *et al.*, CLEO Coll., *Phys. Rev. Lett.* **86** (2001) 4467.

[48] P. Abreu *et al.*, DELPHI Coll., *Eur. Phys. J.* **C20** (2001) 617.

[49] K. Edwards *et al.*, CLEO Coll., *Phys. Rev.* **D56** (1997) 5297.

[50] W. Marciano and A. Sirlin, *Phys. Rev. Lett.* **61** (1988) 1815.

[51] D.I. Britton *et al.*, *Phys. Rev. Lett.* **68** (1992) 3000.

[52] C. Czapek *et al.*, *Phys. Rev. Lett.* **70** (1993) 17.

[53] R. Decker and M. Finkemeier, *Phys. Rev.* **D48** (1993) 4203.

[54] R. Alemany, M. Davier and A. Höcker, *Eur. Phys. J.* **C2** (1998) 123.

[55] M. Davier and A. Höcker, *Phys. Lett.* **B419** (1998) 419.

[56] M. Davier and A. Höcker, *Phys. Lett.* **B435** (1998) 427.

[57] M. Davier, S. Eidelman, A. Höcker and Z. Zhang, *Eur. Phys. J.* **C27** (2003) 497.

[58] S. Anderson *et al.*, CLEO Coll., *Phys. Rev.* **D61** (2000) 112002.

[59] R.R. Akhmetshin *et al.*, CMD-2 Coll., *Phys. Lett.* **B527** (2002) 161.

[60] R.R. Akhmetshin *et al.*, CMD-2 Coll., *Phys. Lett.* **B578** (2004) 285.

[61] M. Davier, S. Eidelman, A. Höcker and Z. Zhang, *Eur. Phys. J.* **C31** (2003) 503.

[62] G. W. Bennett, *et al.*, Muon $(g-2)$ Coll., *Phys. Rev. Lett.* **92** (2004) 161802.

[63] D. Asner *et al.*, CLEO Coll., *Phys. Rev.* **D61** (2000) 012002.

[64] M. Bishai *et al.*, CLEO Coll., *Phys. Rev. Lett.* **82** (1999) 281.

[65] T. E. Coan *et al.*, CLEO Coll., *Phys. Rev. Lett.* **92** (2004) 232001.

[66] J. Z. Bai *et al.*, *Phys. Rev. Lett.* **88** (2002) 101802.

[67] E. Braaten, S. Narison and A. Pich, *Nucl. Phys.* **B373** (1992) 581.

[68] A. Pich, *Nucl. Phys.* **B39** (Proc. Suppl.) (1995) 326.

[69] A. Höcker and V. Kartvelishvili, *Nucl. Inst. Meth.* **A372** (1996) 469.

[70] K. Ackerstaff *et al.*, OPAL Coll., *Eur. Phys. J.* **C7** (1999) 571.

[71] L.R. Surguladze and M.A. Samuel, *Phys. Rev. Lett.* **66** (1991) 560;
S.G. Gorishny, A.L. Kataev and S.A. Larin, *Phys. Lett.* **B259** (1991) 144.

[72] M.A. Shifman, A.L. Vainshtein and V.I. Zakharov, *Nucl. Phys.* **B147** (1979) 385;
ibid **B147** (1979) 448; *ibid* **B147** (1979) 519.

[73] E. Braaten and C.S. Li, *Phys. Rev.* **D42** (1990) 3888.

[74] H. Czyż and J. H. Kühn, *Eur. Phys. J.* **C18** (2001) 497.

[75] J. Bijnens and P. Gosdzinsky, *Phys. Lett.* **B388** (1996) 203.

[76] I.B. Vasserman *et al.*, TOF Coll., *Sov. J. Nucl. Phys.* **33** (1981) 709.

[77] I.B. Vasserman *et al.*, OLYA Coll., *Sov. J. Nucl. Phys.* **30** (1979) 519.

[78] L.M. Barkov *et al.*, OLYA and CMD Coll., *Nucl. Phys.* **B256** (1985) 365.

[79] A. Quenzer *et al.*, DM1 Coll., *Phys. Lett.* **B76** (1987) 512.

[80] D. Bisello *et al.*, DM2 Coll., *Phys. Lett.* **B220** (1989) 321.

[81] S. R. Amendolia *et al.*, NA7 Coll., *Phys. Lett.* **B138** (1984) 454.

[82] A. Aloisio *et al.*, KLOE Coll., *Phys. Lett.* **B606** (2005) 12.

[83] M. Battle *et al.*, CLEO Coll., *Phys. Rev. Lett.* **73** (1994) 1079.

[84] S. Eidelman, *Recent results from Novosibirsk*, International Workshop on τ Lepton Physics, Nara (Sept. 2004).

[85] G.J. Gounaris and J.J. Sakurai, *Phys. Rev. Lett.* **21** (1968) 244.

[86] F. Guerrero and A. Pich, *Phys. Lett.* **B412** (1997) 382; D. Gómez Gumm, A. Pich and J. Portolés, *Phys. Rev.* **62** (2000) 054014.

[87] M. Davier, *Nucl. Phys.* (Proc. Suppl.) **B 131** (2004) 192.

[88] F. Le Diberder and A. Pich, *Phys. Lett.* **B289** (1992) 165.

[89] T. Coan *et al.*, CLEO Coll., *Phys. Lett.* **B356** (1995) 580.

[90] E. Braaten, *Phys. Rev. Lett.* **60** (1988) 1606.

[91] K.G. Wilson, *Phys. Rev.* **179** (1969) 1499.

[92] F. Le Diberder and A. Pich, *Phys. Lett.* **B286** (1992) 147.

[93] K.G. Chetyrkin and A. Kwiatkowski, *Z. Phys.* **C59** (1993) 525.

[94] P.A. Baikov, K.G. Chetyrkin and J.H. Kühn, *Phys. Rev.* **D67** (2003) 074026.

[95] P. M. Stevenson, *Phys. Rev.* **D23** (1981) 2916.

[96] A. L. Kataev and V. V. Starshenko, *Mod. Phys. Lett.* **A10** (1995) 235.

[97] F. Le Diberder, *Nucl. Phys.* **B39** (Proc. Suppl.) (1995) 318.

[98] S.A. Larin, T. van Ritbergen and J.A.M. Vermaseren, *Phys. Lett.* **B400** (1997) 379.

[99] A.A. Pivovarov, *Sov. J. Nucl. Phys.* **54** (1991) 676, *Z. Phys.* **C53** (1992) 461.

[100] K.G. Chetyrkin, B.A. Kniehl and M. Steinhauser, *Phys. Rev. Lett.* **79** (1997) 2184.

[101] K.G. Chetyrkin, B.A. Kniehl and M. Steinhauser, *Nucl. Phys.* **B510** (1998) 61.

[102] B. L. Ioffe and K. N. Zyablyuk, *Eur. Phys. J.* **C27** (2003) 229.

[103] W. Bernreuther, W. Wetzel, *Nucl. Phys.* **B197** (1982) 228;
W. Wetzel, *Nucl. Phys.* **B196** (1982) 259;
W. Bernreuther, *Ann. Phys.* **151** (1983) 127.

[104] G. Rodrigo, A. Pich, A. Santamaria, *Phys. Lett.* **B424** (1998) 367.

[105] LEPEWWG/2004-01, hep-ex/0412015.